© Copyright 2024

Yinong Zhang

Emergent Phenomena and Applications in Artificially Stacked 2D Materials

Yinong Zhang

A dissertation
submitted in partial fulfillment of the
requirements for the degree of

Doctor of Philosophy

University of Washington
2024

Reading Committee:
Xiaodong Xu, Chair
David Cobden
Ting Cao

Program Authorized to Offer Degree:
Physics

University of Washington

Abstract

Emergent Phenomena and Applications in Artificially Stacked 2D Materials

Yinong Zhang

Chair of the Supervisory Committee:

Professor Xiaodong Xu

Physics

Two-dimensional (2D) semiconducting transition metal dichalcogenides (TMDs) possess broken inversion symmetry and strong spin-orbit coupling, leading to unique spin-valley locking effect. In TMD multilayers, rich excitonic responses are identified from the direct-to-indirect bandgap transition, where the coupling among spin, valley and layer pseudospin plays a crucial role in forming bright and dark exciton species and their complex hybridizations. Furthermore, structural engineering can be leveraged in building Rhombohedral (R) and Hexagonal (H) stacking orders and forming moiré superlattice that further modulate the band structure and give rise to exotic physics. In this thesis, we first demonstrate the photoluminescence and reflectance spectra under varying doping densities and electric fields while increasing TMD layer thickness, to explain the bandgap transition. We further show that the spin-valley locking in H-stacked multilayer TMD yields an electronic superlattice structure, where alternating layers correspond to barriers and quantum wells, respectively, depending on the spin-valley indices and that the spin-valley locked superlattice hosts a kind of dipolar excitons with the electron and hole constituents separated in an

every-other-layer configuration. Such excitons become optically bright via hybridization with intralayer excitons. This effect is also manifested by the presence of multiple anti-crossing patterns in the reflectance spectra, as the dipolar exciton is tuned through the intralayer resonance by an electric field. As layer thickness keeps increasing, the dipolar exciton can form one-dimensional Bose-Hubbard chain displaying a layer number dependent fine spectroscopy structures. In the next chapter, we identify the interfacial ferroelectricity in R-stacked twisted TMD. We perform scanning probe imaging to directly visualize the alternating domain polarizations. Optical spectroscopy of ABBA-twisted double bilayer TMD under varying out-of-plane electric fields reveals rich excitonic responses, among which the inter-bilayer excitons are coupled with local domain polarizations and result in built-in electric fields. Weak hysteresis loop of the inter-bilayer excitons' emissions is observed while sweeping the external electric field at opposite directions, and confirms the domain wall dynamics dictated by the interfacial ferroelectricity. Finally, in the last chapter, we report the observation of exciton hybridizations coupled with interfacial ferroelectricity in R-stacked twisted bilayer WSe_2 systems, where dipolar excitons are allowed due to the matched spin-valley index and can hybridize with certain intralayer A exciton branches through an electron hopping process, which also makes them optically bright. Combining the built-in electric fields, we reconstruct the hybridization behaviors that are coupled with the interfacial ferroelectricity from the R-stacked moiré interface. Furthermore, ferromagnetism and correlated states are identified in the same system through magneto-optic effect. Our results demonstrate the delicate coupling between the excitonic responses and the artificially stacked 2D materials and reveal exciting and exotic physical phenomena.

TABLE OF CONTENTS

List of Figures ..... **iii**

List of Tables ..... **vi**

Chapter 1. Introduction **1**

1.1 Two-dimensional materials and heterostructures 1

1.2 Dissertation outline 5

1.3 Methods for fabricating two-dimensional heterostructures 8

1.3.1 PC-based dry transfer technique 13

1.3.2 Alignment of 2D crystals 16

1.3.3 AFM-based metallic contact improvement technique 17

1.3.4 Cryogenic optical measurements 19

Chapter 2. Excitonic responses in transition metal dichalcogenides **21**

2.1 Formation of excitons 21

2.2 Doping and field dependent spectroscopy from monolayer TMD 25

2.3 Direct-to-indirect bandgap transition in bilayer TMD 29

Chapter 3. Every-other-layer dipolar excitons in a spin-valley locked superlattice 33

3.1 Spin-valley locked superlattice in TMD 33

3.2 Spectroscopy signatures of every-other-layer dipolar excitons 35

3.3 Exciton hybridizations 37

3.4 Stacking dependence 43

3.5 Layer number dependence 45

3.6 Summary and applications 49

Chapter 4. Engineering ferroelectricity in Rhombohedral-stacked transition metal dichalcogenides.....50

4.1 Ferroelectricity in a dielectric 50

4.2 Device fabrications.....56

4.3 Visualization of interfacial ferroelectricity 59

4.4 Dipolar excitons coupled with interfacial ferroelectricity.....62

4.5 Summary and applications 71

Chapter 5. Multiferroics and exciton hybridizations in twisted bilayer transition metal dichalcogenides.....73

5.1 Physics in twisted bilayer TMD 73

5.2 Excitonic responses in twisted bilayer TMD 76

5.3 Exciton hybridizations coupled with interfacial ferroelectricity.....86

5.4 Magnetism and correlated physics in twisted bilayer TMD.....97

5.5 Summary and applications 101

Bibliography 103

Appendix A: Power dependence of monolayer WSe_2 excitons in device M2 119

Appendix B: Lattice Reconstructions in Rhombohedral-stacked twisted TMD 120

Appendix C: Reconstructing every-other-layer DX 122

Appendix D: Supplementary data.....124

LIST OF FIGURES

1.1 Tunable magnetism in twisted $MoTe_2$ devices 3

1.2 Capacitor model in 2D heterojunctions and its applications 4

1.3 Real-space lattice structure and reciprocal-space band dispersion of TMD monolayers .6

1.4 Semiconductor manufacturing process 9

1.5 Fabrications of 2D heterostructures 11

1.6 Mutations of PC dry transfer techniques 15

1.7 AFM-based metal contact cleaning techniques 18

1.8 Experimental setups for dR/R and PL measurements 20

2.1 Recombination of excitons 22

2.2 Mechanisms of PL and dR/R 23

2.3 Power dependence of monolayer WSe_2 excitons and defect-bound PL emissions 25

2.4 Tunability of monolayer WSe_2's optical spectra 26

2.5 Tunable optical spectroscopy of bilayer WSe_2 30

3.1 Spin-valley locked superlattice 34

3.2 Spectroscopy signatures of every-other-layer DXs in trilayer WSe_2 36

3.3 Electric field dependence of PL spectra in trilayer WSe_2 37

3.4 Electric field tuning of exciton hybridization 38

3.5 Modeling and reconstructing the every-other-layer DXs in trilayer WSe_2 41

3.6 Second order carrier hopping 42

3.7 Reflectance spectrum differentiated with respective to photon energy 43

3.8 Stacking-dependent every-other-layer DX 44

3.9 Layer number dependence and multiple anti-crossings 46

3.10 Modeling and reconstructing the every-other-layer DXs in five-layer WSe_2.....48

4.1 Hysteresis loop in P-E curves 51

4.2 MX and XM stackings in R-stacked TMD 52

4.3 Lattice reconstruction in twisted TMD.....53

4.4 Domain wall dynamics under external electric field 54

4.5 Mechanisms of the hysteresis loop in twisted TMD.....55

4.6 Tear-and-stack techniques for fabricating twisted TMD.....57

4.7 Visualization of interfacial ferroelectricity.....59

4.8 PL spectra in ABBA twisted double bilayer WSe_2 63

4.9 Electric field dependent PL emissions in ABBA twisted double bilayer WSe_2.....64

4.10 Dipolar excitons coupled with interfacial ferroelectricity 66

4.11 Optical signatures of hysteresis loop.....70

5.1 Adjacent layer hopping in R-stacked twisted bilayer TMD 74

5.2 Intravalley and intervalley PL spectra of R-stacked twisted bilayer WSe_2 device W1...77

5.3 dR/R spectra of R-stacked twisted bilayer WSe_2 device W1 78

5.4 dR/R spectra of R-stacked twisted bilayer WSe_2 device W2 80

5.5 Asymmetric carrier hopping in R-stacked twisted bilayer WSe_2.....82

5.6 Layer polarization analysis 83

5.7 Asymmetric carrier hopping in R-stacked twisted bilayer $MoTe_2$ 84

5.8 Schematic of energy bands and exciton structures in device W2.....86

5.9 Modeling the exciton hybridizations coupled with one domain in device W1 88

5.10 Modeling the exciton hybridizations coupled with one domain in device W2 88

5.11 Modeling the exciton hybridizations averaged over both domains in W1 and W2.....92

5.12 Modeling the exciton hybridizations coupled with both domains in W1 and W2 94

5.13 Modeling and reconstructing the background in W1 and W2 96

5.14 Experimental setups for RMCD measurement 97

5.15 Filling factor assignments for device W1.....98

5.16 Doping density dependent RMCD in W1 99

5.17 Temperature dependent RMCD at ν = -0.63 100

A.1 Power dependence of monolayer WSe_2 excitons in M2.....119

B.1 Visualization of interfacial ferroelectricity in P2 before being strained.....120

B.2 Visualization of interfacial ferroelectricity in P2 after being strained.....121

C.1 Every-other-layer DX versus hopping amplitude.....122

C.2 Every-other-layer DX versus asymmetric hopping amplitude.....123

D.1 Electric field dependences of the intravalley and intervalley PL in device W1 124

D.2 Hysteresis loop missing from twisted bilayer WSe_2.....125

D.3 Layer polarization analysis.....126

LIST OF TABLES

4.1 Fitting parameters for DXs coupled with ferroelectricity.....69

5.1 Fitting parameters for exciton hybridizations coupled with MX domain.....89

5.2 Fitting parameters for exciton hybridizations coupled with XM domain.....90

5.3 Fitting parameters for exciton hybridizations averaged over both domains.....93

5.4 Fitting parameters for exciton hybridizations coupled with both domains.....95

5.5 Fitting parameters for exciton hybridizations in twisted $MoTe_2$.....96

ACKNOWLEDGEMENTS

First, I would like to express my gigantic gratitude to my advisor Xiaodong, not only for the well-organized lab environment and the professional teamwork he's leading, but also for his constant inspirations and dedication in condensed matter physics during the past five years. I still remember the Monday meetings during the spring of 2022, during which we were drafting my first manuscript and I was greatly encouraged. He told me the story of how he, as an experimentalist, had been performing theoretical calculations in his early career stage with the company of his theoretical physicist friend Prof. Wang Yao. Following his path, I began to steer myself to a rigorous and versatile researcher with full of passions ever since. Moreover, Xiaodong provided me with countless resources and opportunities, including scientific collaborations, conferences and career opportunities. It was a really unforgettable experience working in such environment.

I would also like to thank my reading committee: Profs. David Cobden and Ting Cao. We had multiple pleasant but insightful discussions over research, career and life (and Chinese language learning with Dave). Nevertheless, I want to express my thankfulness to my supervisory committee, Profs. Alejandro Garcia, Jun Liu, Xiaosong Li and Alexandra Velian, for taking their time to attend my General and Final exams and provide comments from a surprisingly different perspective outside the field of condensed matter physics.

The past five years would not be unforgettable without the colleagueship, the teammate-ship, the friendship with everyone who's once been in the Xu lab before. First to my same-year cohorts Eric Anderson, Jiaqi Cai, Jiayi Zhu and Jordan Fonseca, we share the five-year incredible journey from struggling for the first-year courses to surviving the pandemic, to finally graduating together. To Dmitry Ovchinnikov, Xi Wang and Yingqi Wang, thank you for being my mentors during my first-year confusion period. I also had fun and knowledgeable moments with my previous roommates Minhao He, Qianni Jiang, Jiaqi Cai and Chong Wang, when we shared rents,

kitten, drones, scientific discussions and scientific gossips every night after work. Nevertheless, I cannot ever stop learning from the huge $MoTe_2$ team including Eric Anderson, Chaowei Hu, Courtney Baier, Dhan Bautista, Jack Barlow, Jiang Yao, Jiaqi Cai, Jiayi Zhu, Joon Park, Julian Stewart, Weijie Li, Will Holtzmann, Yuzhou Zhao. I'm amazed by the teamwork we have been carrying out. Plus, I want to express my gratefulness to Jordan Fonseca, Kyle Hwangbo, Yue Shi, for sharing the struggle of job searching under such a depressed macro-economy and job market. I've also enjoyed working (and every group dinner, hiking, bike riding, snowboarding, gym hitting) with everyone around: Bevin Huang, Nathan Wilson, Qi Zhang, Zaiyao Fei, Tiancheng Song, Yang Liu, Yuhao Li, John Cenker, Geoffrey Diederich, Zhaoyu Liu, Chun-Chih Tseng, Xuetao Ma, Mai Nguyen, Ren, Essance Ray.

All the accomplishments in our lab would not have been done without our collaborators. I therefore would like to thank all our collaborators who have contributed to our research work. Within UW, the network among different research groups is more than common. We have received huge theoretical support from Profs. Di Xiao and Ting Cao's group, and high-quality crystals from Prof. Jiun-Haw Chu's lab. For me personally, I have also received assistance on cleanroom facilities from students in Profs. Mo Li and Arka Majumdar's group, and instructions from Prof. Arthur Barnard on nanoelectromechanical systems. There are too many more research groups I want to name in one paragraph: Profs. David Cobden, Matthew Yankowitz, Kai-Mei Fu, Daniel Gamelin, Jihui Yang, Jun Liu, Alexandra Velian, … I want to express thankfulness to even more collaborators outside UW. Chengxin Xiao from Prof. Wang Yao's theoretical group provides numerical ideas and concepts on how to perform simulations and reconstructions on excitonic responses, which lead me to an insightful understanding of exciton formations and hybridizations that will be discussed in this thesis. The twisted TMD project is initiated in close collaboration with Xirui Wang and Kenji Yasuda from Prof. Pablo Jarillo-Herrero's group at MIT. I also want to express my thankfulness to Jiaqiang Yan for growing the most reliable TMD crystals I've ever seen, and of course, Takashi Taniguchi and Kenji Watanabe for the world's best hexagonal boron nitride crystals. As I attend more scientific conferences, I earn more friendships with researchers around the world.

Finally, I owe my deepest gratitude to my parents. They have been visiting me by over-20-hour international flights, especially during the pandemic. They inspired me to pursue scientific research when I was a kid, and now they are extremely supportive and proud of what I am doing here. My luckiest moment in the past five years was when I met my girlfriend, Evelyn, who is always there in my toughest moments. Thank you for your endless patient, understanding, and for always being my advocate.

Dedication

To my family.

CHAPTER 1. INTRODUCTION

1.1 TWO-DIMENSIONAL MATERIALS AND HETEROSTRUCTURES

While I'm sitting in front of my desktop and typing down this chapter, I realize that most of us are living in a three-dimensional space. We humans are so used to every physics rule and theory in three dimensions, that we are sometimes not easy to understand what happens to the worlds with different numbers of dimensions. In high school, I learned that time can be included as the fourth dimension to the space following the Theory of Special Relativity and form the four-dimensional Minkowski space, where the spacetime interval between two events are described by a four-dimensional distance and are independent of the choice of the inertial frame of reference. In modern physics, the dimensions used to describe a physical picture are going higher and higher. For instance, the current versions of string theory require ten spatial dimensions plus time as the eleventh dimension in total. Although confusing, physicists and mathematicians have developed methods to generalize high-dimensional spaces. For instance, I'm always into the calculation of a N-dimensional sphere's volume/surface area by considering the integral $\int e^{-(x_1^2+\cdots+x_N^2)}dx_1 \dots dx_N$ over the entire N-dimensional space. The result is $\pi^{N/2}$ if we divide the integral into N one-dimensional Gaussian integrals. On the other hand, the integral can be written as:

$$\int e^{-(x_1^2+\cdots+x_N^2)}dx_1 \dots dx_N = \int_0^\infty e^{-r^2} N\varsigma(N) r^{N-1} dr = \pi^{\frac{N}{2}} \tag{1.1}$$

where $\varsigma(N)$ is the N-dimensional unit sphere's volume ($r = 1$). Therefore, we obtain the volume of N-dimensional sphere equal to $V = \varsigma(N)r^N = \frac{\pi^{N/2}}{(N/2)!}r^N$. This can be used in calculating the phase space and density of states (DOS) of a N distinguishable particles system.

On the contrary of going higher, in condensed matter physics, we are going to the other limit of lower dimensions. Middle school biology teacher said that lower-dimensional creatures are struggling since they must share their inlets and outlets of their bodies, while their bodies will

be penetrated and split into two pieces otherwise. However, low-dimensional quantum materials such as quantum dots, nanotubes, and two-dimensional (2D) thin films have been thriving for decades due to their unique properties and potential applications across various fields. The discovery of graphene in 2004 by Geim and Novoselov marked the beginning of a new era in material science[1], leading to extensive research on 2D materials beyond graphene. The history of 2D materials can be traced back to the isolation of graphene, which was achieved using a simple method known as mechanical exfoliation, or the "Scotch tape" method, which will be mentioned in Chapter 1.3. This discovery earned Geim and Novoselov the Nobel Prize in Physics in 2010 and sparked a global surge of interest in other 2D materials.

2D materials are characterized by their atomic-scale thickness, consisting of a single layer or a few layers of atoms. These materials exhibit remarkable structural properties, including high mechanical flexibility that can be manipulated by pressure and strain and can be applied as NEMS (nanoelectromechanical systems) such as suspended membranes for environmental sensing[2,3], large surface area to volume ratios that can be applied as light sensors and catalysts for electrochemistry[4,5], and their unique electronic and optical properties that will be elaborated throughout this thesis.

The structural properties of 2D materials can be broadly categorized based on their composition and bonding. The very first and most commonly used 2D material, graphene, consists of sp2-bonded carbon atoms forming a hexagonal lattice. The strong in-plane covalent bonding provides graphene with exceptional mechanical strength. Other 2D materials, such as transition metal dichalcogenides (TMDs), boron nitride (BN), and black phosphorus (BP), have different lattice structures while sharing some important similarities. For example, hexagonal boron nitride (hBN) has a structure similar to graphene but with alternating boron and nitrogen atoms, giving it excellent thermal and chemical stability. However, they all possess weak van der Waals (vdW) interlayer interactions but strong intralayer covalent bonding, allowing for easy exfoliation into few layers and even monolayers from their bulk crystals.

2D materials possess multiple advantages over their three-dimensional counterparts. For instance, graphene exhibits carrier mobilities exceeding 10^5 $cm^2/V \cdot s$, which makes graphene an

excellent candidate for high-speed electronic devices. Similarly, TMDs such as MoS_2 and WSe_2 with tunable bandgaps (direct-to-indirect bandgap transition[6-8]) offer advantages for electronic and optoelectronic applications such as laser generation and light sensing, where bandgap engineering is crucial for optimizing device performance. The mechanical properties of 2D materials also provide significant advantages. Graphene's tensile strength and flexibility make it ideal for use in flexible and wearable electronics/soft materials. Other 2D materials, such as hBN, provide excellent thermal stability and can be used as insulating layers in electronic devices, enhancing their performance and reliability.

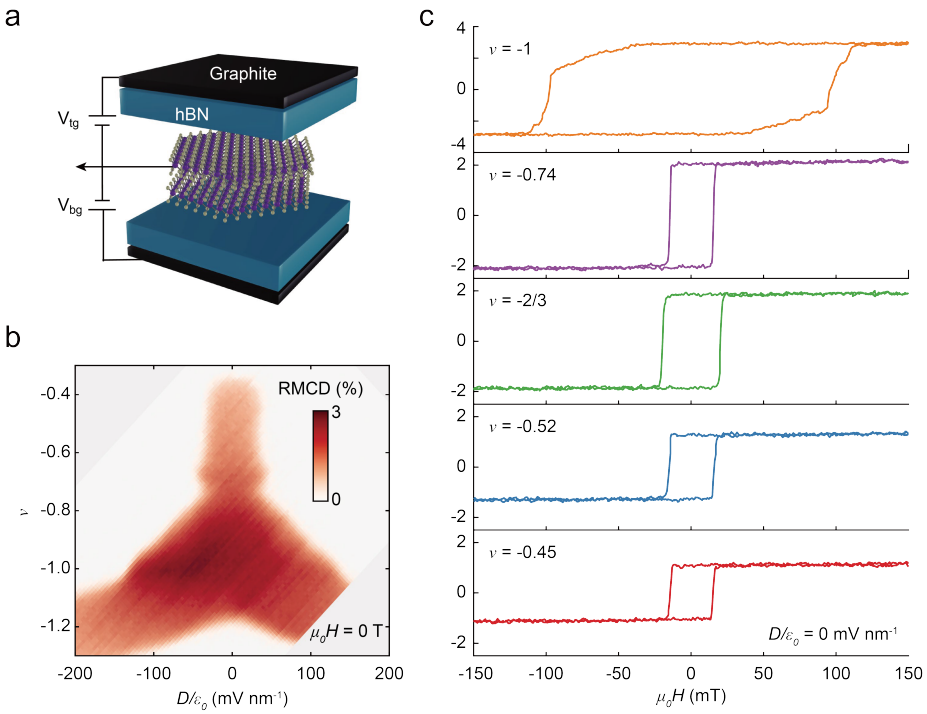

Figure 1.1: Tunable magnetism in twisted $MoTe_2$ devices. a, Schematic of dual-gated twisted $MoTe_2$ device structure. **b,** magnetization (RMCD signal) versus filling factor ν and electric field D at zero magnetic field. The phase space with non-vanishing signal corresponds to the ferromagnetic state. **c,** magnetization (RMCD signal) versus magnetic field swept back and forth at selected fillings. Reproduced from Ref. [9] with permission.

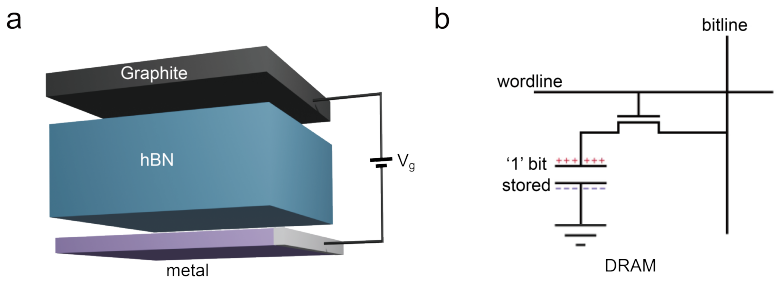

Figure 1.2: Capacitor model in 2D heterojunctions and its applications. a, Schematic of a 2D capacitor. **b,** Simplified circuit of a DRAM unit.

The exploration of new 2D materials has led to the discovery of materials with novel properties. For instance, 2D ferromagnetic materials, such as CrI_3 and Fe_3GeTe_2, exhibit intrinsic ferromagnetism[10-13]. These materials open up new opportunities for spintronic applications, where the spin of electrons, rather than their charge, is used for information processing. The ability to control and manipulate spin in 2D materials could lead to the development of spin-based transistors and memory devices.

Nevertheless, as a group of thin film materials where all the z-motions of carriers are limited, 2D materials allow us to engineer and stack different thin films together like LEGO blocks[14]. By stacking different 2D thin films layer by layer, or by stacking the same 2D materials in a way different from their natural stacking orders, different layers can talk to each other through transport or proximity effect, leading to exotic physical phenomena and applications. Furthermore, by stacking different 2D thin films together, we can realize nano-devices with functionalities. For instance, the twisted $MoTe_2$ device in Fig. 1.1a is a tunable ferromagnetic device whose magnetic state can be tuned by changing the top and bottom gate voltages (Figs. 1.1b, c). And the ferromagnetism in this twisted $MoTe_2$ material system, on the other hand, is realized by stacking two non-ferromagnetic $MoTe_2$ monolayers together with a misalignment angle between their crystal orientations, which will be discussed in Chapter 5.4.

To demonstrate how important the role layer-stacking plays in 2D materials. We can consider the simplest structure of two conducting films (such as graphene) encapsulating an

insulating dielectric layer (such as hBN) (Fig. 1.2a). We then realize a parallel-plate capacitor, which is one of the most common structures in computer and hardware engineering. For instance, DRAM (dynamic random-access memory) is one of the most basic units nowadays in CPU and GPU, that contains a capacitor to store a bit information by turning on and off the transistor (Fig. 1.2b). It is more robust and reliable against power instability, compared to the traditional RAM that uses current flowing directions to store binary information. Companies like Micron Technologies are currently trying to increase the dielectric constant of their capacitor for a smaller size and lower leakage and power consumption.

If we replace one metal plate by a semiconducting thin film, this capacitor model can then be leveraged for electrostatic doping this semiconducting 2D material. The number of carriers doped into the semiconducting plate will change the Fermi level and can be calculated using the capacitor model:

$$n = \frac{c}{e} V_g = \frac{\varepsilon}{ed} V_g \tag{1.2}$$

where e is the elementary charge, V_g is the gate voltage applied to metal plate, and $c = \varepsilon/d$ is the unit capacitance with ε as the dielectric constant and d as the thickness of the dielectric layer. However, the semiconducting plate also feels an electric field from the other plate that can modulate the band structure. Therefore, we can build another capacitor and form a symmetric dual-gated geometry to compensate for the electric field, which will be further discussed in Chapter 1.3. This additional gate allows us to independently control both the doping density and the electric field that is applied to the semiconducting layer.

1.2 DISSERTATION OUTLINE

The group of materials that we are going to focus is called transition metal dichalcogenides, or TMD, with the general formula MX_2, where M represents a transition metal (such as Mo, W, or

Ti) and X represents a chalcogen (such as S, Se, or Te). The transition metal atom is bonded by two chalcogen atoms, and forms a hexagonal crystal lattice, which is also similar to graphene (Fig. 1.3a)[15]. The monolayer TMDs are discovered almost the same time as the first successful isolation of monolayer graphene. These materials have gained significant attention due to their unique electronic, optical, and mechanical properties. Popular candidates include MoS_2 and WSe_2 for their potential in nano-photonics and opto-electronics[16], and $MoTe_2$ for its recently observed fractional Chern insulator state and tunable ferromagnetism[9,17,18].

Unlike graphene, TMD materials usually have a sizable bandgap in the visible and near-infrared range[19]. Furthermore, monolayer TMD features a direct bandgap at the K valley, which facilitates the population of the direct excitons, where the electron and hole constituents can recombine at the K valley's band edge without the assistance of phonon and defect scatterings, leading to a strong photoluminescence (PL) emission. The reduced dielectric screening in 2D materials leads to a strong Coulomb interaction and further enhances its optical emission, compared to higher-dimensional materials[20-22]. But when we increase the layer number of a TMD material, its band structure will undergo a direct-to-indirect bandgap transition, leading to rich excitonic responses including interlayer and intervalley excitons, which will be demonstrated in Chapter 2.

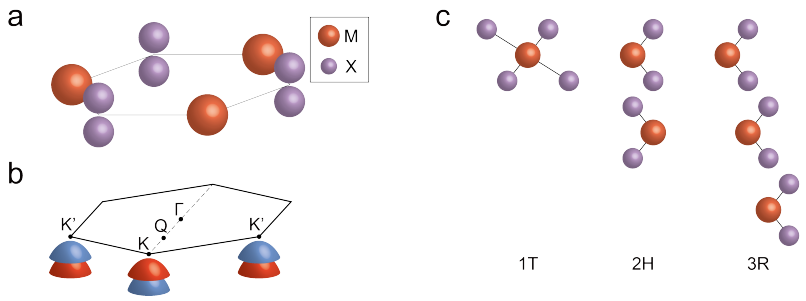

Figure 1.3: Real-space lattice structure and reciprocal-space band dispersion of TMD monolayers. a, Crystal structure of a TMD monolayer in real space. **b,** spin-valley coupled band edges in reciprocal space. Different valleys are labeled. **c,** Schematic of 1T, 2H, 3R stacking orders in TMD multilayers.

Furthermore, the conduction and valence band edges at the K valley have a sizable spin splitting that is contributed from the heavy transition metal atoms. In a monolayer TMD, the sign of the spin splitting for both conduction and valence bands have a valley dependence due to the broken inversion symmetry, which gives rise to the spin-valley locking effect[23]. In the momentum space of a monolayer TMD, adjacent corners of the hexagonal Brillouin zone have opposite spin splitting (Fig. 1.3b). We can therefore label K and K' valleys alternatingly to distinguish their signs of the spin splitting. For different TMD materials, the sign of conduction band spin splitting might also be different. In a certain K/K' valley, W-based TMD materials have the same spin splitting for both conduction and valence bands, while Mo-based TMD materials' conduction band spin splitting is opposite to their valance band spin splitting, leading to a bright exciton ground state[22].

Nevertheless, monolayer TMD has a unique light-matter interaction due to the valley selection rule, where the right and left circular polarized light can only induce optical transitions at the K and the K' valleys[24-26]. Therefore, the connections among spin, valley, and light chirality are well established and give rise to rich physics, such as the every-other-layer dipolar excitons in multilayer TMD that will be discussed in Chapter 3. Therefore, TMDs are an excellent platform for valleytronic quantum devices, where information is encoded in the valley degree of freedom of electrons, which could lead to the development of novel quantum applications.

Few-layer TMDs possess another distinct degree of freedom, named layer pseudospin. TMDs can exist in 3 polytypes (Fig. 1.3c), depending on the co-ordination of chalcogen atoms around the transition metal atoms and the stacking order of the layers. The first, 1T, is a metallic crystal with octahedral co-ordination that has recently been artificially synthesized for device applications[27]. The more common 2H (hexagonal) and 3R (Rhombohedral) polytypes are semiconducting, with trigonal prismatic coordination. For simplicity, we call them H-stacked and R-stacked instead. They have been experimentally synthesized and observed[28]. The properties of H-stacked and R-stacked TMDs have been reported to be almost identical[29], with little observable change in their Raman spectra. But they have rather different symmetry. For instance, R-stacked TMD bilayer breaks both inversion and mirror symmetries, which contributes to significant second

harmonic generation (SHG) signals and possible ferroelectricity (Chapter 4). When the TMD flakes are getting thicker, their possible out-of-plane stacking orders become more complicated, with unique properties for each stacking order. Therefore, stacking order has become another tuning knob for TMD material engineering.

In summary of the dissertation outline, I'll first introduce the methodology from device fabrications to characterizations for the rest of this chapter. In Chapter 2, I'll summarize the optical spectroscopy of TMD materials, with a focus on monolayer and bilayer WSe_2 specifically. Direct-to-indirect bandgap transition and emergent interlayer and intervalley exciton species are included and analyzed by photoluminescence and reflectance spectroscopy separately. Based on Chapter 2, I'll focus on the spin-valley locking effect in H-stacked multilayer TMD in Chapter 3. A spin-valley locked superlattice chain is identified in this system with rich industrial applications, and a new type of dipolar exciton with large tunability and hybridization behavior is first observed. In Chapter 4, we play with the stacking order and artificially engineer ferroelectricity using the originally non-ferroelectric TMD monolayers/bilayers. Finally, in Chapter 5, I'll report our recent discovery of multiferroics in R-stacked twisted bilayer TMD systems. Exciton hybridization appears in a similar process mentioned in Chapter 3, and is further coupled with the ferroelectricity arising from the moiré interface mentioned in Chapter 4. Magnetic correlated states are also characterized in the same system leveraging magneto-optic effect measurements.

1.3 METHODS FOR FABRICATING TWO-DIMENSIONAL HETEROSTRUCTURES

In the field of 2D materials, if we want to measure something, we will engineer and build a device by ourselves. As shown in Fig. 1.4, we can start from flakes like graphene, Boron Nitride, and finally fabricate a dual-gated device with a hall bar geometry to perform complicated measurements. In this section, I will introduce the experimental setups and techniques used to produce the results presented in Chapter 2-5. A detailed description of sample fabrications and characterizations is provided. Fabrication of reproducible thin films with high qualities is of vital

significance for vdW heterostructure research. Furthermore, new techniques for semiconductor fabrication innovations have also been developed in our lab during the past several years.

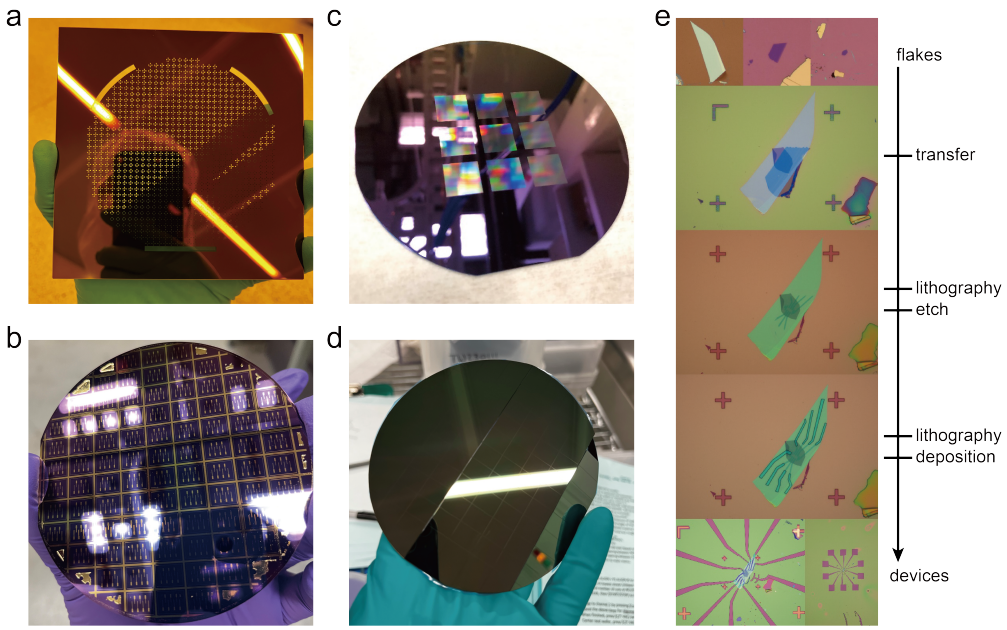

Figure 1.4: Semiconductor manufacturing process. a-d, photos of a photomask (**a**), a wafer after photolithography and PVD (**b**), a wafer after plasma etching (**c**) and a diced wafer (**d**). **e,** Optical microscope images of a typical 2D device fabrication process.

To fabricate nanodevices with functionalities, the core idea is to collect all the "LEGO blocks" used to assemble, which usually includes a substrate, 2D thin films, metal contacts, and sometimes polymer protective coatings. In our lab, a successful and complete device fabrication typically includes substrate preparation, mechanical exfoliation, flake transfer, metal deposition, and packaging. The general process procedures are described below:

Step 1 – Substrate preparation: A successful device fabrication starts with a proper substrate. To select the right substrate, intended applications and physical properties need to be considered. Typically, 285 nm SiO_2 on 500 μm p-doped Si wafer is used for most of the nanodevices and flakes

exfoliations such as graphene, due to the optimized contrast for graphene flake visualization[30]. Alternatively, 90 nm SiO_2 is used for hBN exfoliations and related device applications also due to a better contrast. Besides, thin silicon, GaAs, sapphire are also used for different purposes such as strain and better thermal conductivities.

A cleaning process such as oxygen plasma etching should be taken before any flake is put onto the substrate, because the ultraviolet (UV) light and high-energy charged particle bombardment are efficient in breaking most organic bonds[31,32], resulting in an effective removal of dangling bonds and polymer residues, and a better adhesion to the 2D flakes. Therefore, a higher exfoliation yield can be achieved.

Step 2 – Mechanical exfoliation: Scotch tape is used to peel bulk vdW crystals (either commercial or grown by collaborators) into thinner layers by peeling one piece of thin bulk into multiple thinner copies on the same tape or multiple tapes (Fig. 1.5a)[33]. The tapes are then gently pressed onto the selected substrates with bubbles squeezed out. In addition to oxygen plasma mentioned above, annealing the tape-on-chip structure at a high temperature on a hot plate can also increase the exfoliation yield, where the temperature and duration depend on the material being exfoliated. Typically, graphene is heated at 90 °C for 2 min while TMD is heated at 120 °C for 5 min to reach the optimal yield. Due to vdW force between the flakes and substrate, a number of thin layers stay at the substrate after peeling off the tape, which are further selected by optical microscope and atomic force microscope (AFM), assisted by second harmonic generation (SHG) measurement. Alternatively, PDMS sometimes can be used to replace the scotch tape for materials that are hard to pick up by PC films. But its drawback comes from the polymer residues on the exfoliated flakes' surface, compared to the ideally atomic clean surface of the tape-exfoliated flakes.

Step 3 – Flake transfer: To stack 2D thin films layer by layer and form a functional structure, dry transfer method is carried out (Fig. 1.5b). Typically, a flat PC stamp, which will be described in detail in Chapter 3.2, is used to pick up 2D flakes at high temperatures (details are described in

3.2). During the transfer, the flakes are monitored under optical microscope and the Z-axis motion of the PC stamp is controlled by a motor. The rotary stage gives another degree of freedom to manipulate the twist angle between two flakes, which facilitates the control of moiré superlattice periodicity. Scanning probe imaging such as piezoresponse force microscope (PFM)[34] can be performed upon the flakes on the stamp during the transfer, in order to obtain the sample topography as well as the moiré superlattice periodicity. The considerable AC conductance of PC film promises a decent grounding to the flakes being imaged by scanning probe. The flakes are eventually melted down together with the PC film onto the designated substrate, which is washed off by chloroform solvent to remove the PC residues. Alternatively, polypropylene carbonate (PPC) film and PDMS can be used sometimes in substitute of PC film due to a lower melt-down temperature, while these polymers are always harder to pick up 2D materials as a trade-off.

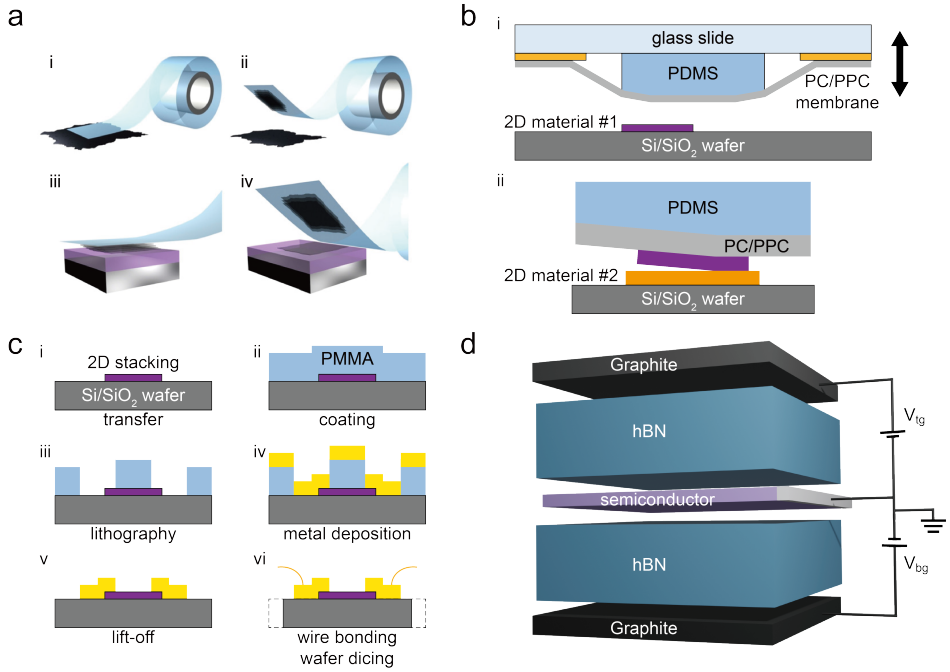

Figure 1.5: Fabrications of 2D heterostructures. a, Illustration of mechanical exfoliation by scotch tapes. Reproduced from Ref. [33]. **b,** Illustration of dry transfer techniques. **c,** Illustration of metal deposition and packaging. **d,** Schematic of a dual-gated device structure with top and bottom capacitor structures for electrostatic doping.

Step 4 – Metal deposition: Physical vapor deposition (PVD) techniques such as electron beam evaporation, thermal evaporation, and sputtering are used (Fig. 1.5c). Typically, 70 nm gold is used for gate/drain/source/contact electrodes after assembling all the flakes into a stack. For TMD materials, platinum electrodes are used instead for a matched work function to the valence band as well as a strong spin-orbit coupling induced by the heavy nucleus of platinum[35]. To prevent the metal deposited from being easily removed, 2-7 nm chromium is used as an adhesion layer between the metal layer (gold/platinum) and the SiO_2 substrate and forms covalent bond (Cr-O).

To transfer the pattern of electrodes, lithography techniques such as electron beam lithography (EBL) (Fig. 1.4e) and photolithography (Fig. 1.4a) are carried out, among which photolithography is intended for wafer scale and repeated patterns, with 1.0-1.1 μm thick AZ1512 as the photoresist, while EBL is intended for smaller scale pattern writing with 500 nm thick A4 495 or A4 950 polymethyl methacrylate (PMMA) as the e-beam resist.

If necessary, dry etching techniques such as reactive ion etching (RIE) and inductively coupled plasma (ICP) etching are carried out to trim and shape 2D materials. Generally, ICP etching with 40 sccm fluoroform (CHF_3) and 4 sccm oxygen and 70 W radio frequency (RF) power at 20 °C is used to etch most 2D materials including graphene, hBN and TMD with a high selectivity.

Step 5 – Calibration of doping density and electric field. The electrostatic doping densities in the heterobilayer are determined from the applied gate voltages based on a parallel-plate capacitor model (Fig. 1.5d)[36]. The thickness of hBN is determined by atomic force microscopy, typically around 10-20 nm thick. Similar to (1.2), the doping density is calculated as $c_b V_{bg} + c_t V_{tg}$, where c_t and c_b are the capacitances of the top and bottom gates and V_{tg} and V_{bg} are the applied gate voltages relative to the level of the valence/conduction band edge. The geometric capacitance is calculated using $c_{t,b} = \varepsilon_0 \varepsilon_{hBN} / d_{t,b}$ with the dielectric constant of hBN $\varepsilon_{hBN} \sim 3$ (Ref. [37]). The

out-of-plane electric displacement field is calculated using $D = (c_b V_{bg} - c_t V_{tg})/2$ and the electric field is calculated using $E_Z = D/\varepsilon_0 \varepsilon_{hBN}$. We can therefore write down the relation as:

$$\begin{pmatrix} n \\ E_Z \end{pmatrix} = \begin{pmatrix} \frac{\varepsilon}{e}\frac{1}{d_t} & \frac{\varepsilon}{e}\frac{1}{d_b} \\ -\frac{1}{2}\frac{1}{d_t} & \frac{1}{2}\frac{1}{d_b} \end{pmatrix} \begin{pmatrix} V_{tg} \\ V_{bg} \end{pmatrix} \tag{1.3}$$

Step 6 – Packaging: Before measurement, post-transfer process such as wafer dicing and wire bonding are used to package the device-on-chip and load it to a chip carrier (Fig. 1.5c). For wafer dicing, silicon blade with 30000 rpm is used to trim the SiO_2/Si substrate into a smaller size that can fit the chip carrier, typically below 1 cm^2. The diced chip is then glued onto the chip carrier by silver paste and is connected by gold wires.

1.3.1 PC-BASED DRY TRANSFER TECHNIQUE

The PC stamp dry transfer technique mentioned above are of vital significance for 2D nanodevice fabrication (Fig. 1.5b). A dish of PDMS is first made by mixing standard curing agent and base at a ratio of 1:10 and pumped under vacuum for degassing and baked at a high temperature. A hole-puncher is used to cut the PDMS into a cylinder shape. The PDMS cylinder is then placed onto a clean glass slide before being covered by a PC film. PC films are typically prepared by spreading PC droplets between two clean glass slides, while PC solvent is made by dissolving PC powder into chloroform with a 7–10% mass ratio and stirring for more than 14 days. PC thin films are covering both glass slides' surface after sliding the two glass slides apart and drying for 10 mins. A basic PC stamp is prepared by transferring the PC film from the glass slide to the top of PDMS cylinder using a scotch tape and razor. Ideally, the PC film forms a tent over the PDMS cylinder. Similarly, a PPC stamp can also be made by transferring the PPC film onto the PDMS cylinder, while the PPC film is often prepared by spin coating the PPC in anisole solvent (around 20%) onto silicon chips and baking at 90 °C.

During the transfer, the PC stamp is fixed by the transfer stage with a Z-axis motor control. Substrate with the target flake is loaded onto a rotary stage with temperature control. An optical microscope is used to monitor the distance between the PC stamp and the substrate, and to align flakes. Lateral adjustment to the substrate is made for alignment before slowly touching the PC stamp down to the substrate at a high temperature (typically 90 °C for graphene, 80 °C for hBN, 70 °C for TMD). After picking up all the flakes, the PC stamp is heated up to 180 °C while in touch with the clean substrate, so that the PC film that holds the flakes is melted down onto the substrate. Chloroform solvent is then used to wash off the PC film while leaving the flakes sticking to the substrate. While for PPC stamp dry transfer, flakes are picked up at 30 – 40 °C, while they are dropped down on SiO_2/Si chip at 70 – 90 °C. Anisole is used to wash off the PPC residues if needed.

Nevertheless, mutations of PC dry transfer also play an important role in our study. They are described below:

PC stamp flip transfer: Before being picked up by a PC stamp, the bottom surface of an exfoliated flake is atomically clean. This is because the bottom surface has never been in contact with residues after being peeled off from the bulk crystal. This offers an ideal platform for scanning probe imaging such as piezoresponse force microscope (PFM) and Kelvin probe force microscope (KPFM) for any domain characterizations, especially during the transfer of a moire superlattice (twisted TMD). Therefore, a solvent-free, flip transfer technique is adopted to fabricate samples with atomically clean top surface specially for scanning probe imaging measurements.

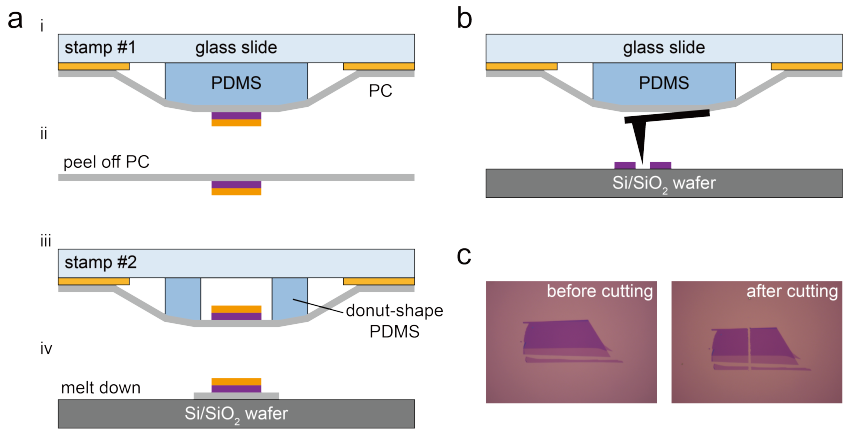

Figure 1.6: Mutations of PC dry transfer techniques. a, Illustration of the PC stamp flip transfer technique. **b,** Illustration of the tip cutting technique. **c,** Optical microscope images of a bilayer WSe_2 flake before (right) and after (left) tip cutting.

For this purpose, a PC flip stamp is prepared using almost the same process as a PC stamp, except that a thermal release tape (with a release temperature at 100-130 °C) is inserted between the glass slide and the PC film. As demonstrated in Fig. 1.6a, after picking up the flakes (below the release temperature) just like normal PC dry transfer, the PC film together with the flakes is peeled off after heating the stamp over the release temperature. It is then flipped and taped onto a "donut"-shape PDMS (it can be cut using two hole-punchers with different size). The flakes picked up by the PC film is suspended over the "donut" hole and facing toward the glass slide, so that the top surface stays atomically clean. A normal melt-down process is taken to leave the clean flakes onto the substrate, which is ready for scanning probe imaging measurement without any further chemical treatment.

Tip cutting technique: Adopting the similar ideas, flakes can be mechanically cut by a stamp holding a sharp tip. Lateral movement of the stage while the tip contacting the substrate is able to cut the flake along the path (Figs. 1.6b, c). To make such stamp holding a tip, a PDMS cube is first cut and put onto a glass slide. Tips for atomic force microscope (AFM) is selected due to a sharp profile and low cost. The cantilever of the AFM tip is then carefully taped on to the PDMS by

scotch tape. This method can be applied to assist the tear-and-stack technique for stacking homobilayer structure, which will be described below.

1.3.2 ALIGMENT OF 2D CRYSTALS

Stacking two 2D thin films with a certain alignment between their crystal orientations, either being accurately aligned or twisted by a certain rotational angle, is significant in determining the physical properties. Therefore, an accurate determination and control of the crystal orientation is as significant.

Tear-and-stack technique: In this method, an exfoliated 2D flake can be torn apart into two pieces. One piece can be picked up first and rotated by a certain angle by the rotary stage, before being stacked onto the other piece. A precise alignment is thus realized. Normally, a relatively soft 2D flake, such as graphene or TMD, is torn by the sharp edge of a thick hBN flake on the stamp, due to a much greater adhesion from hBN (vdW interaction) than the PC film. During the transfer, a straight edge of the hBN flake on the stamp should be aligned to the middle of the target flake. The slightly tilted stamp should approach the chip at an extremely slow rate, until the hBN edge covers half of the target flake, while the other half remains atomically clean and not in contact with the stamp. The target flake is likely to be torn while slowly lifting the stamp at a lower temperature. If successful, half of the target flake will be picked up by the stamp while the rest remains on the chip. However, failure happens especially if the target flake is too small (less than 8 μm). The small target flake might be dragged or even be picked up as a whole by the stamp.

Due to the uncertainty, improvement has been made by using the tip cutting technique mentioned above. By aligning the straight edge of the hBN flake and the cut on the target flake, half of the flake is easily picked up and then stacked onto the other half without any concern.

Second harmonic generation: If the inversion symmetry is broken in the crystal structure of the target flake such as odd-layer TMD, its crystal orientation can be determined using optical characterizations such as linear-polarization-resolved second harmonic generation (SHG)[38]. the

intensity of the SHG co-linearly polarized with the excitation laser is analyzed as a function of crystal orientation. The orientation of the armchair edges is determined by fitting the angular dependence of the intensity to the equation, $I = I_0 \cos^2(3\theta)$, where I_0 is the maximum SHG intensity and θ is the angle between the laser polarization and the armchair edge[39,40]. The relative angle between two flakes can therefore be obtained by fitting their SHG intensities. We note that this technique is not sensitive to the SHG phase and thus the specific direction along the armchair edge is unknown. Phase-resolved SHG can be used to verify the absolute stacking orientation[41].

Piezoresponse force microscope: During PC-based tear-and-stack process, high temperature as well as the pressure/strain applied to the PC stamp might cause lattice relaxation and therefore inaccuracy of the crystal orientation alignment. Piezoresponse force microscope (PFM) is sometimes used to accurately measure the twist angle in the middle of the transfer. In this method, an AC bias is applied between the tip and sample that induces a periodic deformation of the sample. Local electromechanical response is then collected by the tip[34]. For marginally twisted flakes with a moiré superlattice, domain boundaries between adjacent moiré sites have the greatest strain-gradient and therefore give strong electrical polarization signal due to the flexoelectric effect. As a result, hexagonally distributed superlattice pattern of the domain boundaries can be measured by PFM. The superlattice periodicity λ can be converted into the twist angle ϕ using[42]:

$$\lambda = a\frac{1+\delta}{\sqrt{2(1+\delta)(1-\cos\phi)+\delta^2}} \tag{1.4}$$

where a is the lattice constant, δ is the lattice mismatch between the two flakes.

1.3.3 AFM-BASED METALLIC CONTACT IMPROVEMENT TECHNIQUE

While applying gate voltages to the fabricated nano-device, a low contact resistance will lead to a much more accurate control of device's doping density and electric field. For normal 2D materials like graphene, metal contact can be directly deposited onto the flakes with a relatively

low contact resistance. Alternatively, graphene encapsulated by hBN can be etched and metal can be deposited to the edge to form an edge contact[43].

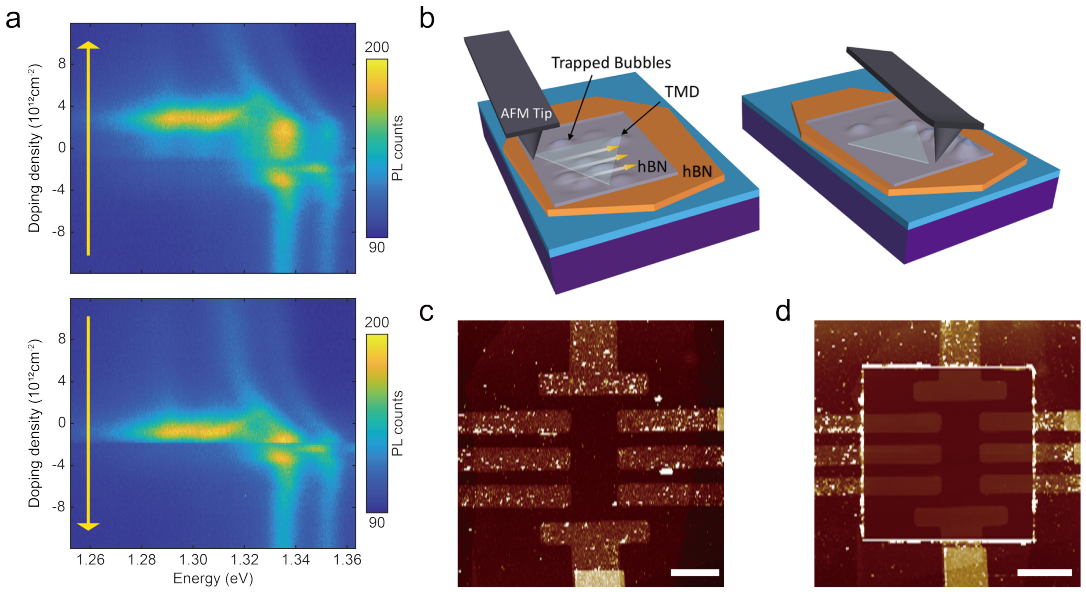

Figure 1.7: AFM-based metal contact cleaning techniques. a, Doping density dependence of dR/R from a twisted bilayer WSe2 device at opposite sweeping directions. **b,** Schematic of AFM cleaning techniques. Reproduced from Ref. [44]. **c,d,** AFM images of a prepatterned backgate before (**c**) and after (**d**) AFM cleaning. Scale bar, 3 μm.

On the other hand, due to a relatively lower mobility and larger bandgap, a high contact resistance can be found, which causes a high energy barrier for the carriers. For instance, hysteresis loop might appear while sweeping device's doping density from hole-doping to electron-doping, and reversely from electron-doping to hole-doping (Fig. 1.7a). The high contact resistance comes from the many defects between the metal and TMD. To solve this problem, an atomic-clean metal-TMD interface should be achieved. An alternative fabrication process is to first prepattern the metal contacts onto the substrate/backgate before transferring TMD onto the metal. This can also prevent TMD from degradation because the transfer of TMD can be done in the glovebox.

AFM cleaning technique is then used to clean the metal surface (Fig. 1.7b)[44]. After locating the target area of the prepatterned metal contacts, the AFM tip (OTESPA-R3) is then brought down to contact the metal surface with a 0.20 – 0.80 V deflection and scratch the target area over and over at a scan rate around 20 μm/s. The residues from evaporation and polymer resist are effectively pushed to the side of the target area and leave an atomic-clean area (Fig. 1.7c). After transferring the TMD, there will be covalent bond at the interface which metalize the TMD on top of the metal[35] and significantly lower the contact resistance down to ~3 kΩ at 2 K. This is lower than h/e^2 (Ref. [45]), indicating a high signal-to-noise ratio while measuring the Hall effect.

1.3.4 CRYOGENIC OPTICAL MEASUREMENTS

The photoluminescence (PL) and differential reflectance (dR/R) measurements are performed using a home-built confocal microscope in reflection geometry. The sample is mounted in an exchange-gas cooled cryostat with temperatures down to 5K unless otherwise specified. For dR/R measurement (Fig. 1.8a), a tungsten halogen white light source is used to excite the sample through a single mode optical fiber. The dR/R spectrum is obtained as $dR/R \equiv (R' - R)/R$, by comparing the reflected light intensity from the sample (R') to that of a featureless spectrum (R) from graphite/hBN/graphite area in the same sample. For PL measurement (Fig. 1.8b), continuous-wave (CW) excitation is generated by a 632.8-nm helium-neon laser or a power-stabilized and frequency-tunable narrow band (< 50 kHz) Ti:Sapphire laser (M2 Solstis) at 1.70 eV (730 nm). The beam diameter on the sample is about 1 μm. The reflected light is collected by a high-NA objective lens (LUCPLFLN40X) and passes through a 50 μm pin hole and is eventually captured by a spectrometer with a silicon charge-coupled device (CCD). Polarization resolved measurements are performed with a set of broad-band half-wave plates, quarter wave plates and linear polarizers.

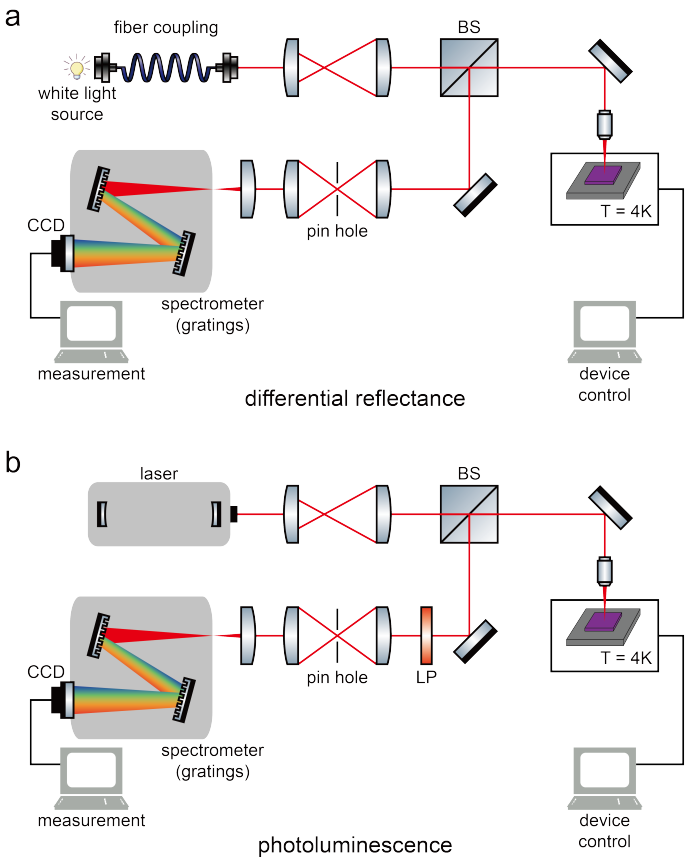

Figure 1.8: Experimental setups for dR/R and PL measurements. a,b, Schematics of light paths in dR/R (**a**) and PL (**b**) measurements. BS, CCD and LP denote beamsplitter, charge-coupled device and linear polarizer, respectively.

CHAPTER 2. EXCITONIC RESPONSES IN TRANSITION METAL DICHALCOGENIDES

In the last chapter, we've discussed the crystal lattice and the band structure of TMD materials, which results in potential industrial applications in optoelectronics, optomechanics and nanophotonics. In this chapter, we are going to elaborate why TMD materials are excellent candidates with respect to their rich excitonic response in optical spectroscopy measurement such as photoluminescence (PL) and differential reflectance (dR/R). This includes the large tunability of their electronic band structures and optical spectra under varying external tuning knobs such as electrostatic doping density, out-of-plane electric field, as well as stacking order and layer number. We will see the direct-to-indirect bandgap transition and the consequent rich interlayer and intervalley excitonic responses while increasing the TMD layer number. This chapter is designed as a general introduction to the optical characterization of TMD materials and lays the groundwork for Chapter 3-5.

2.1 FORMATION OF EXCITONS

The concept of excitons can be traced back to 1931 when Yakov Frenkel was describing the electron and the hole bound by Coulomb force in an atomic lattice[46]. Looking at the electronic band structure of a semiconductor, if an electron is excited to the conduction band, it will thus leave a positively charged hole in the valence band. A bound state will form due to the attractive Coulomb interaction between the two carriers, which also results in a negative Coulomb binding energy. This quasi-particle is called an exciton and is used to describe an elementary excitation that transport energy without transporting net electric charge[47-50]. After a certain length of the exciton's lifetime, the electron and the hole will recombine at the band edges in the band diagram picture (Fig. 2.1a). The radiative recombination results in a luminescence emission with the photon

energy equal to the exciton's energy, which is slightly lower than the size of the bandgap of the semiconductor due to the Coulomb binding energy. The excitons can be excited thermally, electrically, or optically (photonically), resulting in a thermoluminescence, electroluminescence (EL)[51], or photoluminescence (PL)[52-54] process, respectively. The resulted luminescence processes have led to various real-world applications in optoelectronics including light-emitting diode (LED)[51,55,56].

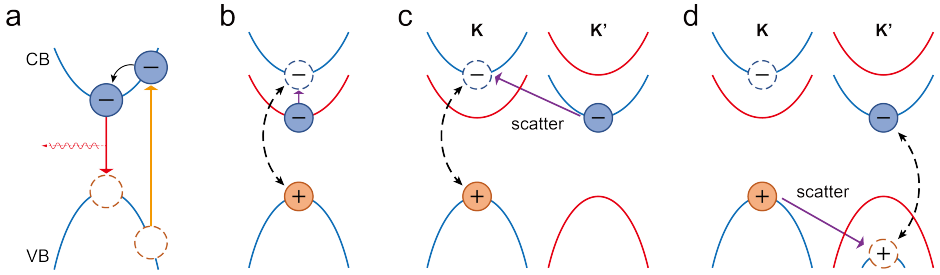

Figure 2.1: Recombination of excitons. a, Schematic of an excited electron and hole recombined at the band edge with a photon emission. **b-d,** Schematics of exciton recombination through spin flipping (**b**) and valley flipping (**c, d**) with assistance of defect and phonon scatterings.

In our studies, PL is used widely to characterize the band structure of semiconductors, due to the advantages of a nondestructive measurement and an insensitivity to the sample's inhomogeneity. To perform PL spectroscopy, a single-wavelength laser that has a higher photon energy than the bandgap passes through a high-NA objective lens (LUCPLFLN40X) and is focused on the sample surface (Figs. 2.2a, c). The PL response that contains information upon the bandgap has a smaller energy and can be filtered from the reflected light by a long pass filter and sent to a spectrometer for analysis (Fig. 1.8b).

2D materials have a strong quasiparticle confinement along the z axis and a reduced dielectric screening, which increases the electron-hole overlap (smaller exciton Bohr radius) as well as the Coulomb interactions[20-22]. The combination of these effects therefore leads to a strong exciton oscillator strength and a large binding energy, and the formation of tightly bound trions

when the system is doped. As mentioned in Chapter 1.2, monolayer TMD has a direct bandgap at the K valley. The direct transition of the exciton gives a strong PL emission and leads to a short lifetime that falls within the picoseconds range[19,57-60]. On the contrary, the single-particle bandgap becomes indirect due to a downshift of the conduction band at the Q valley and an upshift of the valence band at the Γ valley while increasing the layer number of TMD materials[6-8]. As a result, optically dark momentum-indirect transitions such as Q-K and Q-Γ dominates the PL spectra. Due to a vanishing in-plane optical dipole of the dark excitons[61,62], the majority of their PL emissions propagates towards the in-plane direction, resulting in a lower efficiency even with a high-NA objective lens[63,64]. Furthermore, due to the momentum mismatch between the electron and the hole constituents of a momentum-indirect exciton, phonon and defect scatterings are involved as an alternative radiative recombination channel during its PL emissions (Figs. 2.1b, c, d). Such scattering processes significantly increase the decay time of the indirect excitons to tens or hundreds of picoseconds[57].

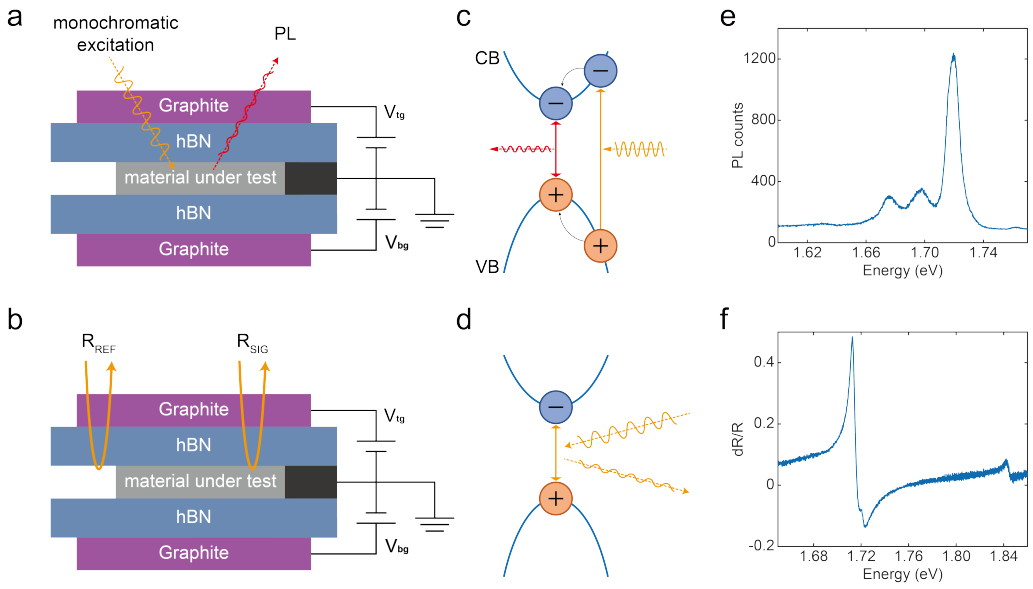

Figure 2.2: Mechanisms of PL and dR/R. a,b, Side views of optically exciting 2D heterostructures in PL (**a**) and dR/R (**b**) measurements. **c,** Schematic of PL excitation and emission in band picture. CB and VB denote conduction band and valence band. **d,** Schematic of dR/R resonance in band picture. **e,f,** PL (**e**) and dR/R (**f**) spectra of monolayer WSe_2 at charge neutrality.

Furthermore, excitons in TMD materials are always bound to other physical properties. Examples include the satellite states[65] by defect trapping[59], phonon sidebands and replicas when excitons are bound to phonons[66], the formation of charged excitons (also as known as trions)[65,66], moiré potential trapped excitons and trions[67,68], and the coupling between excitons and interfacial ferroelectricity[69], which will be discussed in Chapter 4.4.

On the other hand, differential reflectance, or dR/R, is another spectroscopy technique to measure sample's excitonic response and characterize the band structure[16]. In this method, a tungsten halogen white light source that covers a continuous broad range of wavelengths is used to excite the sample. By taking the difference between the reflectance signal from the sample (R') and off the sample (R) as the reference (Fig. 2.2b), which is normalized by the reference signal to obtain dR/R = (R'-R)/R, only the wavelength component that has a resonant energy as the direct bandgap is absorbed and leaves a heartbeat-shape resonance in the dR/R spectrum (Fig. 2.2d). Compared to PL, only the bright excitons that can directly interconvert with photons are visible. As a result, in the following section, we will see an absence of indirect transitions from the intervalley excitons' signal from the dR/R spectra of multilayer TMD devices.

In addition, the shape of a material's dR/R spectrum resembles a heartbeat, with a dip at slightly higher energy accompanied by a peak at lower energy. This can be explained by the Kramers-Kronig relations in complex index of refraction $\tilde{n} = n + i\alpha$, where the absorption coefficient α peaks at the resonant energy. Therefore, the real index of refraction n should behave as α's first order derivative, which is heartbeat shape. As a result, the reflectance dR/R which is a function of n due to the Fresnel equations also presents heartbeat shape.

The combination of PL and reflectance helps us identify excitonic responses in a system, and further gives an insight into the band structure of a material.

2.2 DOPING AND FIELD DEPENDENT SPECTROSCOPY FROM MONOLAYER TMD

Using the nanofabrication techniques (transfer, lithography, PVD) mentioned in Chapter 1.3, we can build devices with a dual-gated geometry, as shown in Fig. 1.5d, to tune the electrostatic doping density and the out-of-plane electric field independently, using (1.3). At the early stages of characterizing TMD devices, strong hysteresis appears while tuning the doping density from hole-doping to electron-doping and back from electron-doping to hole-doping due to the huge contact barrier (Fig. 1.7a), thus leading to an inaccurate control of the electrostatic gating and misleading results. Therefore, the AFM tip cleaning technique mentioned in Chapter 1.3.3 was originally developed for the purpose of a better metallic contact to TMD materials and much more accurate characterizations. In this chapter, we are focusing on the PL and dR/R measurements of TMD materials with tuning doping density and electric field.

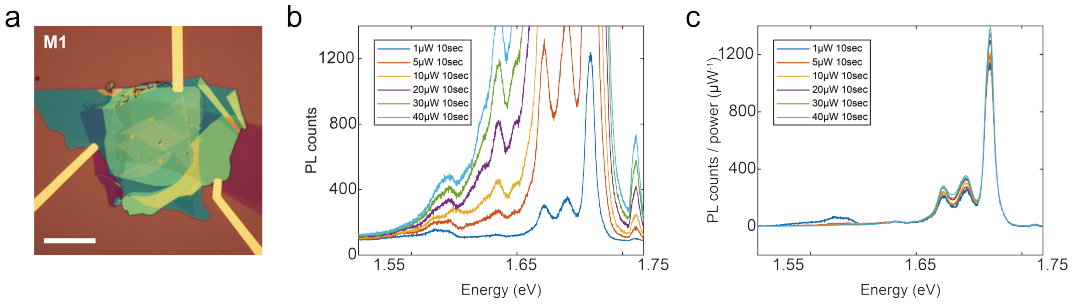

Figure 2.3: Power dependence of monolayer WSe_2 excitons and defect-bound PL emissions. **a,** Optical microscope image of WSe_2 device M1 that has monolayer, bilayer WSe_2 regions. Scale bar, 20 μm. **b,** Power dependence of monolayer WSe_2's PL spectra. **c,** Normalized PL at different excitation powers.

The PL of monolayer WSe_2 device (M1) is shown in Fig 2.2e and Fig. 2.3, with 1-μW laser power and 10-second exposure time. A pronounced A exciton peak with co-circular polarization appears at 1.720 eV as the electron from the top valence band at the K valley recombines with the hole from the bottom conduction band at the same valley. The A exciton is therefore momentum

direct and bright. It is accompanied by two more weaker peaks at 1.697 eV and 1.675 eV, which could be the trion peaks due to the intrinsic doping. The PL spectra vary with sample qualities. In another sample (M2) shown in Fig. A.1, its A exciton peak is located around 1.740 eV, possibly due to strains, defects, dielectric environment and temperature fluctuations. Nevertheless, the dark exciton peak is found at 1.699 eV thanks to the high-NA objective lens and the recombination path assisted by phonon and defect scatterings.

Furthermore, a broad peak at around 1.576 eV is also spotted in device M1, which is attributed to the excitons that are trapped by the defects. While increasing the laser power, the overall exciton population within the excited region. But due to the limited population of excitons that are trapped by material's defects, the defect peak should saturate very fast at a relatively stronger laser intensity. Figure 2.3b shows the power dependence of the PL from the same monolayer WSe_2 sample, with Fig. 2.3c showing the normalized PL counts by the laser power. This defect peak is identified by a saturated peak height at different laser intensities. The spectra of monolayer WSe_2 flakes vary a lot, largely due to the defect states. For instance, the monolayer WSe_2 as shown in Fig. A.1 exhibits multiple defect peaks ranging from 1.61 eV to 1.69 eV. Practically, power dependence measurements are used broadly to examine the defect level and the crystal qualities of TMD monolayers from any unknown batches.

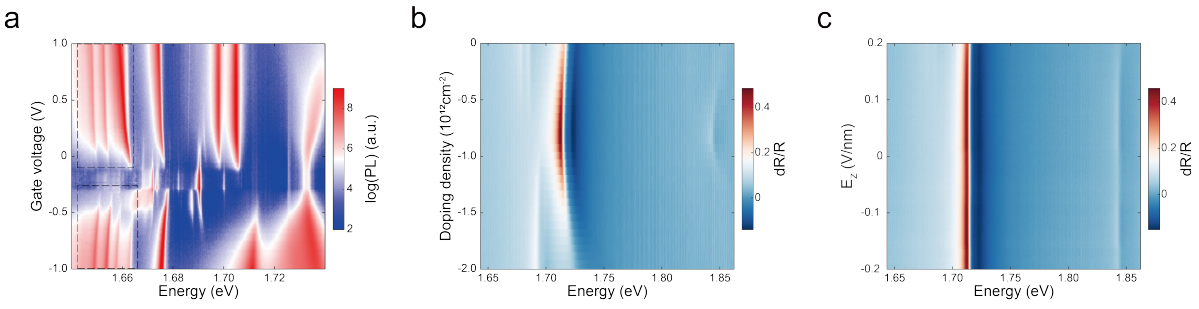

Figure 2.4: Tunability of monolayer WSe_2's optical spectra. a, Doping density dependence of monolayer WSe_2's PL emissions. Reproduced from Ref. [66] with permission. **b,c,** Doping density (**b**) and out-of-plane electric field (**c**) dependences of monolayer WSe_2's dR/R resonances.

While taking the spectra at different gate voltages that are applied to the dual gated device, a 2D plot can be drawn, with the X-axis equal to the PL emission energy that can be converted from the emission wavelength by

$$\epsilon = hc/\lambda \tag{2.1}$$

and the Y-axis corresponding to either the electrostatic doping density or the out-of-plane electric field. The doping density dependence of the PL spectra is plotted in Fig. 2.4a, from previous works in our group[65,66]. Multiple features show up especially while doping the WSe_2 monolayer away from charge neutrality. Among these additional peaks, most of the replicas arise from the coupling of optically dark states to the bright ones via a valley-flip or spin-flip process by emitting valley phonons[66,70], which results in a series Stokes-shifted valley phonon-replicas of the dark exciton and dark trions in the PL spectrum. For instance, the quadruplet PL peaks that are boxed at a minus gate voltage find their origin from the coupling of D^+ with valley phonons K_1, K_2, K_3 and Γ_5 (Ref. [66]).

Besides all the valley phonon replicas, we find PL species that only appear at a non-zero electrostatic doping density, as labeled D^+, X^+ to the hole-doping side and D^-, X_S^-, X_T^- to the electron-doping side, with certain energy differences from the neutral excitons D^0 and X^0, respectively. These charged exciton species are known as trions, which originate from neutral excitons bound to free carriers when there's enough doping density. When electrons or holes are attracted by the neutral excitons and form a new bound state, extra Coulomb binding energy is released and causes a lower emission energy of the trion states. In addition, the fine energy difference between the two negatively charged bright trions X_S^- and X_T^- come from different trion formations. For X_S^- (X_T^-) state, the extra electron is from the same (opposite) valley index, which leads to an intravalley (intervalley) trion structure[71]. The energy deviation between the spin singlet and the spin triplet states gives rise to the fine structure of the splitting negatively charged trion states.

The dR/R spectrum of the monolayer WSe_2 device M3 is shown in Fig. 2.2f. From the heartbeat-like spectrum, the A exciton's resonance can be found at 1.71 eV, which is close to the value of its PL emission energy, indicating a similar emission process. Compared to PL, no other

feature (such as defect states and phonon replicas) can be seen in monolayer WSe_2's dR/R spectrum because only the bright excitons that can directly interconvert with photons are visible in this technique. Thus ideally, higher order orbital states or Rydberg states of a bright exciton are also bright and can be observed with a higher energy but with much weaker intensities, such as the 2S state of the A exciton around 1.84 eV (Fig. 2.2f)[72]. In Chapter 3, we will see that dR/R method can provide a direct and clear study on the K valley excitons in TMD materials, which is dictated by the spin-valley locking. The powerful combination of PL and dR/R techniques gives a thorough excitonic investigation into the electronic band structures of semiconductors.

Figure 2.4b demonstrates the dR/R spectra at a varying electrostatic doping density on another WSe_2 device M3. It's doping dependence resembles the doping dependence of the PL spectra in Fig. 2.4a. However, the dark neutral exciton D^0 together with its charged trion states D^+ and D^- is missing. But we can still see the bright species including the neutral exciton X^0 emission at 1.713 eV (with the absorption dip at 1.723 eV), the positively charged trion X^- at 1.691 eV, and the negatively charged trions X_S^- at 1.678 eV and X_T^- at 1.684 eV. We can thus estimate the binding energy of an additional electron to be 32 meV, and an additional hole to be 45 meV (for intravalley) and 39 meV (for intervalley). Nonetheless, a higher order orbital of the A exciton 2S state is resolved at 1.842 eV.

In monolayer materials, carriers including electrons and holes are constraint in the z-axis, thus limiting their out-of-plane motions. Therefore, the excitons or trions formed within the monolayer material should have their electron and hole constituents within the monolayer plane. In another word, the excitons or trions have a limited electric dipole moment component along the out-of-plane direction. As the electric field dependence dR/R spectra shows in Fig. 2.4c, the excitonic spectrum does not change under a varying out-of-plane electric field. This is because the additional energy from the coupling of an electric dipole moment under an electric field is equal to the minus dot product of the dipole moment and the field vector, known as the Stark energy shift[16]. On the other hand, when we increase the layer number, electron and hole constituents can reside in different layers, known as the interlayer exciton. This leads to an out-of-plane electric

dipole moment and a non-trivial field dependence of the excitonic spectra from multilayer materials, as presented below.

2.3 DIRECT-TO-INDIRECT BANDGAP TRANSITION IN BILAYER TMD

The PL spectrum at charge neutrality of the hexagonal-stacked (H-stacked) bilayer WSe_2 region from the same device M1 is plotted in Fig. 2.5a. Similar to monolayer WSe_2's PL spectrum, a prominent PL peak at 1.703 eV with co-circular polarization is found and corresponds to the intravalley direct excitons at the K valley. Due to the opposite valley index from the adjacent layer in H-stacked TMD and the selection rule, the interlayer transition at the K valley is forbidden[73], which means this intravalley excitonic transition must be intralayer without an out-of-plane electric dipole moment. This is supported by the electric field dependence of the excitonic spectra in Fig. 2.5f. Compared to monolayer WSe_2, the redshift of this K-K exciton emission energy is due to a higher dielectric screening in bilayer. Furthermore, a secondary peak is spotted around 1.690 eV and overlaps with the major peak, which can be explained by the same transition but in the other layer of the bilayer WSe_2, with the energy deviation coming from the inhomogeneous strain induced during fabrication and an inhomogeneous dielectric environment between the top and bottom layers, while another plausible origin of this fine structure is phonon replicas[74].

Different from monolayer, multiple PL peaks appear at a smaller energy ranging from 1.55 eV to 1.63 eV. These peaks do not belong to defect states as the low-energy peaks shown in monolayer TMD's PL spectrum (Figs. 2.3b, c), due to a broader linewidth and higher saturation point while increasing the laser power. In fact, they are unique in multilayer TMD and belong to momentum-indirect transitions such as Q-K and Q-Γ and their phonon replicas[75], which will be elaborated in the following paragraphs. A finite interlayer coupling results in a downshift of the conduction band at the Q valley and an upshift of the valence band at the Γ valley[6]. These momentum-indirect excitons possess a much longer decay time hundreds of picoseconds to tens of nanoseconds[74] due to the scatterings from phonons and defects for momentum conservation[15,54],

compared to sub-picoseconds from monolayer's direct transitions[19,57-60]. Their doping density dependence also resembles the monolayer case, as shown in Fig. 2.5b. To the higher doping density of either electrons or holes, these indirect excitons are bound to free carriers and form trion states, with extra Coulomb binding energies around 17 meV.

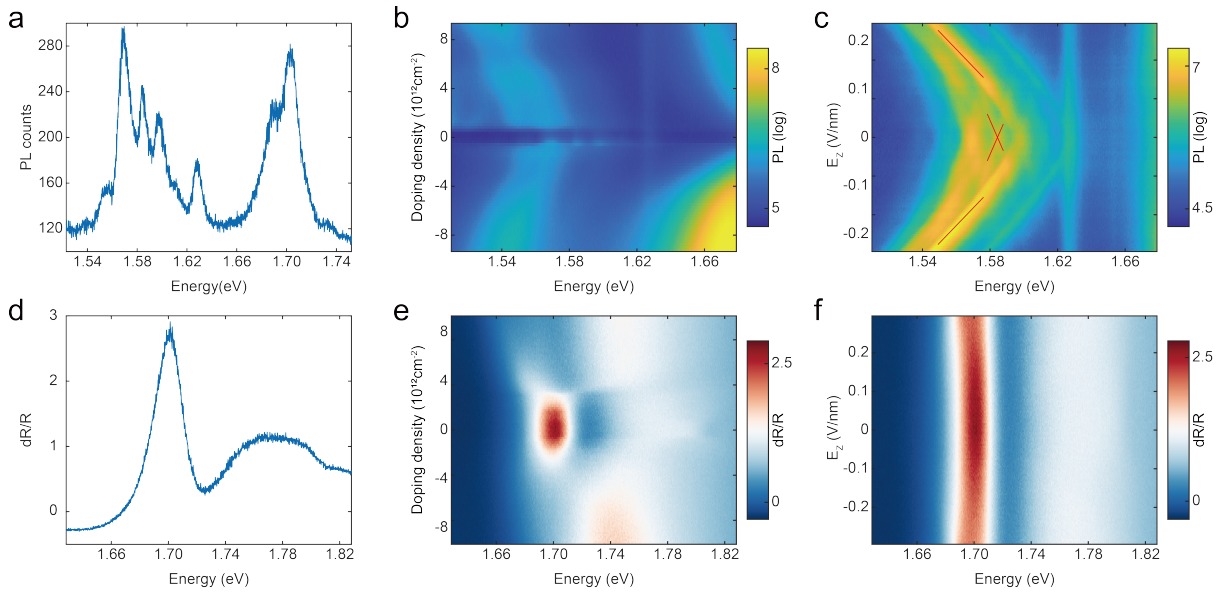

Figure 2.5: Tunable optical spectroscopy of bilayer WSe_2. a, PL spectrum of bilayer WSe_2 at charge neutrality in device M1. **b,c,** Doping density (**b**) and out-of-plane electric field (**c**) dependences of bilayer WSe_2's PL emissions. The red lines in **c** mark the excitons' energy shifts versus the electric field. **d,** dR/R spectrum of bilayer WSe_2 at charge neutrality in device M1. **e,f,** Doping density (**e**) and out-of-plane electric field (**f**) dependences of bilayer WSe_2's dR/R resonances.

However, what makes these momentum-indirect excitons distinct and special is their dispersion under an out-of-plane electric field. Figure 2.5c shows the electric field dependence of their spectra. At a first glance, multiple crossing features can be seen, which is attributed to the interlayer structural properties of these indirect excitons. In a bilayer TMD, a large portion of its excitonic transitions are interlayer excitons[74,75], which have the electron and hole constituents

separated in different layers, e.g., an electron in the top layer and a hole in the bottom layer for a neutral interlayer exciton in a bilayer TMD. An out-of-plane electric dipole moment is therefore formed pointing from the electron to the hole, with its electrostatic energy deviation that can be described by the optical Stark effect $\Delta\epsilon = -\boldsymbol{p} \cdot \boldsymbol{E}$, where $\boldsymbol{p}$ is the electric dipole moment and $\boldsymbol{E}$ is the electric field that the dipolar exciton feels. Specially, for a neutral exciton (or its replicas) with an electron and a hole separated in different layers, its energy can be expanded as:

$$\epsilon = \epsilon_0 - \boldsymbol{p} \cdot \boldsymbol{E} = \epsilon_0 \pm el \frac{\varepsilon_{\mathrm{hBN}}}{\varepsilon_{\mathrm{WSe_2}}} E_Z \tag{2.2}$$

where e is the elementary charge, l is the layer separation between the layers where the electron and the hole reside, E_Z is the out-of-plane electric field calculated in the hBN layer, which is converted by the gate voltages through (1.3). $\varepsilon_{\mathrm{hBN}} \approx 3$ and $\varepsilon_{\mathrm{WSe_2}} \approx 7$ are used to convert E_Z to the field that is applied to the dipolar excitons, dictated by Maxwell's equations. When the electron and the hole that constitute the exciton are separated in different layers, an out-of-plane electric dipole $\boldsymbol{p} = e\boldsymbol{l}$ will point from the electron to the hole. Using this equation, we can linearly fit each excitonic responses and obtain their layer separation (red lines in Fig. 2.5c). The layer separations $|\boldsymbol{l}|$ of the excitonic crossing features at lower electric field is around 0.18 e·nm, which are assigned to the Q-Γ excitons in bilayer WSe_2 (Ref. [75]). Moreover, at higher external electric field, new exciton species with larger layer separations (0.448 e·nm) begin to dominate, which should come from the Q-K excitons where the electron and hole constituents are further apart[75].

Figs. 2.5e, f present the electrostatic doping density and the out-of-plane electric field dependence of the dR/R spectra of the same bilayer WSe_2 region from device M1, respectively. Similar to the monolayer case but different from the bilayer WSe_2's PL spectra, only the K-K momentum-direct transitions are visible due to its direct interconversion with photons. Trion states can also be observed at higher doping density levels. A weak oscillation around 1.80 eV can also be seen in Figs. 2.5e, f, which corresponds to the 2S Rydberg state of the K-K direct excitons.

For the electric field dependence data shown in Fig. 2.5f, it also resembles the monolayer case very much except for a broader linewidth. But this does not mean nothing. In bilayer TMD, we can imagine there could be K-K direct exciton with its electron and hole constituents separated

in different layers. If the recombination of such an exciton is allowed, we can see crossing features in the electric field dependence of the dR/R spectra due to the out-of-plane electric dipole. However, the absence of such exciton species indicates that such transition is forbidden. In fact, the interlayer hopping between adjacent layers in H-stacked TMD bilayer is forbidden due to the annihilated electron interlayer hopping amplitude and the huge energy barrier in the valence band that stops the hole hopping[73]. The huge energy barrier that the carriers encounter while hopping between adjacent layers is caused by the opposite spin splitting that depends on the valley index, which is called the spin-valley locking effect in TMD[23]. The spin-valley locking effect gives rise to a variety of interesting phenomena in TMD systems, including the spin-layer locking effect[73] and the light-valley interaction that leads to the chiral selection rule[24-26]. Therefore, in the next chapter, we will be focusing on the spin-valley locked superlattice structure and the resulted exciton spectra in trilayer TMD and thicker samples that are significantly different from the monolayer and bilayer cases.

CHAPTER 3. EVERY-OTHER-LAYER DIPOLAR EXCITONS IN A SPIN-VALLEY LOCKED SUPERLATTICE

Monolayer semiconducting transition metal dichalcogenides (TMDs) possess broken inversion symmetry and strong spin-orbit coupling, leading to unique spin-valley locking effect. In 2H stacked pristine multilayers, spin-valley locking yields an electronic superlattice structure, where alternating layers correspond to barriers and quantum wells, respectively, depending on the spin-valley indices. Here, we show that the spin-valley locked superlattice hosts a kind of dipolar excitons (DXs) with the electron and hole constituents separated in an every-other-layer configuration, i.e., either in two even or two odd layers. Such excitons become optically bright via hybridization with intralayer excitons. This effect is also manifested by the presence of multiple anti-crossing patterns in the reflectance spectra, as the DX is tuned through the intralayer resonance by an electric field. The reflectance spectra further reveal an excited state orbital of the every-other-layer exciton, pointing to a sizable binding energy in the same order of magnitude as the intralayer exciton. As layer thickness increases, the DX can form one-dimensional Bose-Hubbard chain displaying a layer number dependent fine spectroscopy structures.

3.1 SPIN-VALLEY LOCKED SUPERLATTICE IN TMD

In van der Waals crystals, layer stacking arrangement plays a critical role in determining the material physical properties. Examples include the localized charge hopping and thus flat band formation in magic angle twisted graphene[76,77], the sign switching of interlayer magnetic coupling between rhombohedral and monoclinic stacked 2D magnet CrI_3[78,79], and the formation of interfacial ferroelectricity in AB/BA stacked hexagonal boron nitride (hBN)[80-82]. For transition metal dichalcogenides, such as WSe_2, its monolayer features a sizable spin splitting at the band edges located at the $\pm K$ valleys at the corners of hexagonal Brillouin zone, where time reversal

dictates a valley-contrasted sign of the splitting[23-26,73,83,84]. Multilayers of the 2H stacking feature the 180° rotation between adjacent layers, which is an operation that swaps the spin states between the valleys (Fig. 3.1a). Consequently, for carrier of a given spin-valley index, the dispersion edge alternates between the two split values in even and odd layers. These realize perfect superlattice confinements in the out-of-plane direction (Fig. 3.1b): for a spin up carrier in the K valley ($K,\uparrow$), the even layers serve as energy barriers defining the odd layers as quantum wells (QW), while for carrier with opposite spin-valley index ($K,\downarrow$) the odd and even layers swap their roles[73,85-89].

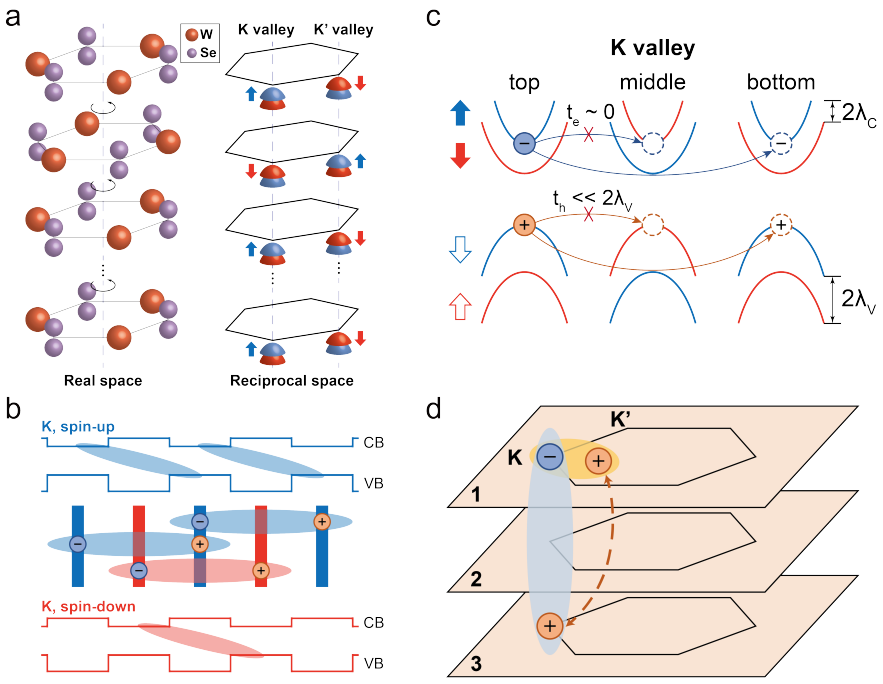

Figure 3.1: Spin-valley locked superlattice. a, Crystal structure of multilayer 2H-WSe_2 in real space (left) and spin-valley coupled band edges in reciprocal space (right). Blue and red arrows stand for spin up and down. **b,** Schematic of the spin-valley dependent superlattice confinement of band edge carriers in 2H-WSe_2 multilayer, and every-other-layer DXs. CB and VB denote conduction and valence band. Light blue/red ellipses represent DXs formed in odd/even layers. **c,** Interlayer hopping between adjacent layers is forbidden due to spin-valley locking, while every-other-layer hopping is allowed. **d,** Coupling between DX (light blue) and intralayer (orange) excitons in trilayer geometry.

In such spin-valley configured superlattice, the barrier height corresponds to the spin splitting[89]. Use WSe_2 as an example, the spin-orbital coupling induced spin splitting is as large as ~ 480 meV in the valence bands[90,91]. Therefore, the low energy holes are well confined in the QW regions (Fig. 3.1b). Electrons see a lower barrier (~30 meV), but their interlayer hopping is forbidden at the $\pm K$ points by the rotational symmetry (Fig. 3.1c). These are reminiscent of the semiconductor superlattices from the periodical growth of two alternating III-V compounds which underlies a broad range of important optical phenomena and applications[92], but now realized in a homogeneous compound, featuring spin-valley dependent confinement (Fig. 3.1b).

In this work, we report the observation of a type of DXs in such spin-valley locked superlattices in multilayer WSe_2. The dipolar exciton, with electron and hole separated in an every-other-layer configuration, has large electric dipole but vanishing optical dipole (Fig. 3.1d). However, it can become optically bright by hybridizing with the intralayer excitons via a weak next-nearest-neighbor interlayer hopping of carriers conserving spin and valley indices (Figs. 3.1c, d), which also indicates that the every-other-layer DXs acquire the same polarization and optical selection rules as the intralayer direct excitons. We first present the results from a trilayer WSe_2 as the building block for such superlattice, i.e., a double QWs.

3.2 SPECTROSCOPIC SIGNATURES OF EVERY-OTHER-LAYER DIPOLAR EXCITONS

Figure 3.2a shows the differential reflectance spectrum normalized by the background reflectance (dR/R) in trilayer WSe_2 without applying gate voltage. The inset of Fig. 3.2a is the optical microscope image of the device, where the WSe_2 is sandwiched by hBN in a dual-gated geometry (see Methods). The doping dependence of dR/R at zero electric field is shown in Fig. 3.2b. There are three resonances at charge neutrality, while the broad background at high energy is caused by optical interference. The spectral features near 1.705 eV and 1.798 eV correspond to the 1S and 2S intralayer excitons, respectively[93-95]. The 1S intralayer exciton state is schematically indicated in Fig. 3.1d by the electron-hole pair enclosed by orange ellipse. Besides, there's a

relatively weaker state at 1.767eV, which is not seen from monolayer and bilayer WSe_2 spectra (Fig. 2.4c and Fig. 2.5f). The origin of this feature, corresponding to the every-other-layer DX with the electron-hole pair enclosed by blue ellipse shaded in Fig. 3.1d, will become clear later in the electrical field dependent measurements. The larger spatial separation of the electron and hole pair leads to a smaller binding energy of the DX compared to the intralayer 1S exciton, and thus higher energy in optical spectrum.

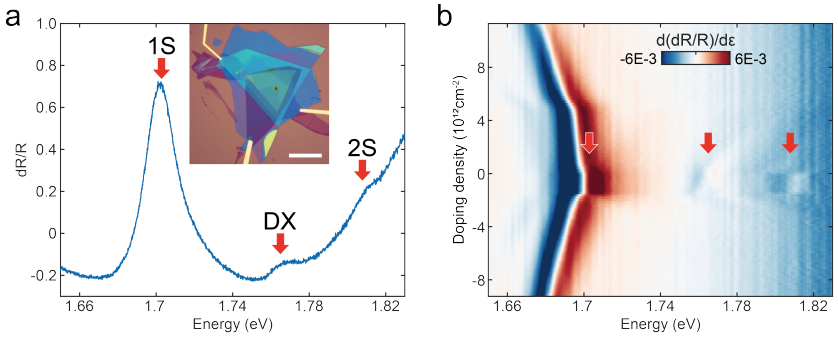

Figure 3.2: Spectroscopy signatures of every-other-layer DXs in trilayer WSe_2. a, dR/R spectrum from trilayer WSe_2 at charge neutrality and zero electric field. DX and intralayer 1S and 2S excitons are indicated by red arrows. The inset shows an optical microscope image of the dual-gated trilayer WSe_2 device. Scale bar, 20 μm. **f,** Doping dependence of differentiated dR/R from trilayer WSe_2 at zero electric field.

We examine optical reflection versus the out-of-plane electric field $\mathbf{E_Z}$ at charge neutrality (Fig. 3.4a. The photoluminescence measurement is shown in Fig. 3.3). As expected, the peak position of both 1S and 2S intralayer excitons are independent of $\mathbf{E_Z}$. In contrast, the exciton feature at 1.767 eV evolves into two branches, whose energies shift linearly with $\mathbf{E_Z}$ and develop an X pattern centering at zero-field resonance. Since there are two energy degenerate DXs but with opposite electric dipoles at $\mathbf{E_Z} = 0$, the applied electric field breaks their degeneracy, linearly decreases (increases) the exciton energy, and forms the observed X pattern. By fitting the stark effect, we can determine the electric dipole to be $d = \frac{\varepsilon_{TMD}}{\varepsilon_{hBN}} \frac{\Delta Energy}{\Delta Ez} \sim 1.4$ e·nm, using dielectric constant $\varepsilon_{TMD} \sim 7$ and $\varepsilon_{hBN} \sim 3$. This extracted dipole is exactly twice of the usual interlayer

exciton observed in heterobilayer TMDs, demonstrating that the electron and hole are now separated in every other layer.

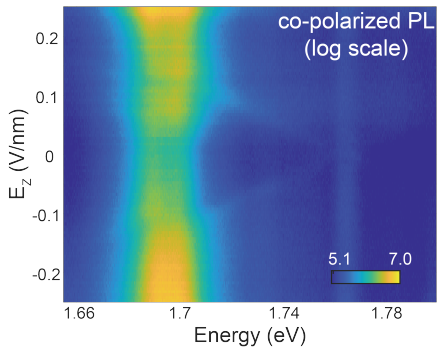

Figure 3.3: Electric field dependence of PL spectra in trilayer WSe_2. In addition to the dR/R data, we examine PL spectra and its $\mathbf{E_Z}$ field dependence on the same trilayer WSe_2. Near K-K direct transition region (around 1.7 eV), we find similar anti-crossing feature as dR/R spectra, supporting the formation of every-other-layer DXs. The field-independent PL feature around 1.76 eV is instrument artefact.

3.3 EXCITON HYBRIDIZATIONS

Figure 3.4a also shows several avoided-crossing features as the DX is tuned across the intralayer exciton resonances[96]. For instances, as $\mathbf{E_Z}$ is around ±0.1 V/nm (±0.06 V/nm), the energy of the DX is nearly resonant with intralayer 1S (2S) excitons, where DXs hybridize with intralayer ones. This hybridization stems from the carrier hopping between layer 1 and 3 (Figs. 3.1c, d), and is crucial for the observation of the every-other-layer DX. We note that such DX has vanishing optical dipole by itself, and becomes visible through hybridization with bright intralayer exciton states, even tens of meV away from the 1S (2S) resonances.

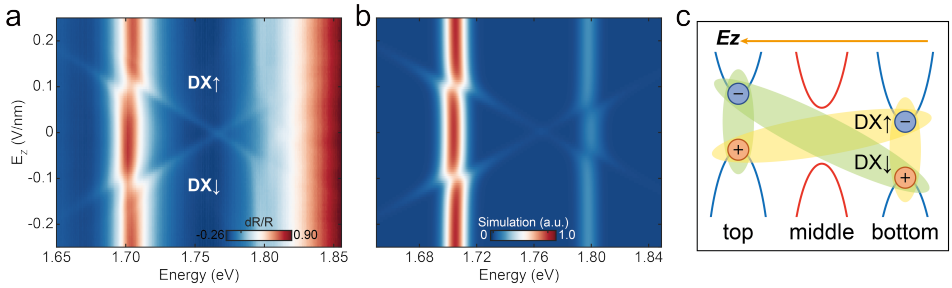

Figure 3.4: Electric field tuning of exciton hybridization. a, Electric field dependence of dR/R spectra from trilayer WSe_2 at charge neutrality. The anti-crossing feature signifies the hybridization between DX and intralayer 1S and 2S excitons. $DX_{\uparrow}$ ($DX_{\downarrow}$) stands for DX with hole and electron in the top (bottom) and bottom (top) layers of the trilayer. **b,** Calculated electric field-dependent spectral density. **c,** Schematic of energy bands and exciton structures under positive electric field, where $DX_{\uparrow}$ hybridizes with the intralayer 1S exciton close by in energy.

To quantitatively understand the observation in trilayer, we examine the coupling of the relevant excitonic basis states: $|1S^{top}\rangle$, $|1S^{bottom}\rangle$, $|2S^{top}\rangle$, $|2S^{bottom}\rangle$, $|DX_{\uparrow}\rangle$, $|DX_{\downarrow}\rangle$, denoting respectively the 1S and 2S orbital intralayer excitons in top and bottom layer, and every-other-layer DXs with electrical dipole pointing up and down. The diagonal part of the Hamiltonian can be written as:

$$H_0 = \begin{pmatrix} \varepsilon_{1S} & 0 & 0 & 0 & 0 & 0 \\ 0 & \varepsilon_{1S} & 0 & 0 & 0 & 0 \\ 0 & 0 & \varepsilon_{DX} - E_Z \cdot d & 0 & 0 & 0 \\ 0 & 0 & 0 & \varepsilon_{DX} + E_Z \cdot d & 0 & 0 \\ 0 & 0 & 0 & 0 & \varepsilon_{2S} & 0 \\ 0 & 0 & 0 & 0 & 0 & \varepsilon_{2S} \end{pmatrix} \tag{3.1}$$

Here, ε_{1S}, ε_{2S}, ε_{DX} denote the energies of intralayer and DXs at zero electrical field, extracted from Fig. 3.4a. Term $\pm E_Z \cdot d$ corresponds to the Stark shift of $|DX_{\downarrow\uparrow}\rangle$ away from their zero-field energy ε_{DX}. The coupling between the DX and 1S (2S) intralayer exciton is through the carrier hopping

with amplitude t_1 (t_2). t_1 (t_2) arises from the overlap in the envelope function of excitonic states and determines the anti-crossing gap near the 1S (2S) resonance.

To understand how carrier hopping can lead to band coupling, and furthermore exciton hybridization, we can first describe in the band picture the every-other-layer hopping. According to Fermi's golden rule, we have:

$$\begin{aligned} \langle e^{\mathrm{top}} | H_{\mathrm{CB}} | e^{\mathrm{bot}} \rangle &= t_e \\ \langle h^{\mathrm{top}} | H_{\mathrm{VB}} | h^{\mathrm{bot}} \rangle &= t_h \end{aligned} \tag{3.2}$$

Here, states $|e^{\mathrm{top/mid/bot}}\rangle$ and $|h^{\mathrm{top/mid/bot}}\rangle$ stand for the conduction and valence band edge wavefunctions at the top/middle/bottom layer, $H_{\mathrm{CB/VB}}$ is the Hamiltonian matrix of the conduction/valence band edges. On the other hand, we can also describe in the band picture the forbidden adjacent-layer hopping:

$$\begin{aligned} \langle e^{\mathrm{top}} | H_{\mathrm{CB}} | e^{\mathrm{mid}} \rangle &= 0 \\ \langle e^{\mathrm{bot}} | H_{\mathrm{CB}} | e^{\mathrm{mid}} \rangle &= 0 \\ \langle h^{\mathrm{top}} | H_{\mathrm{VB}} | h^{\mathrm{mid}} \rangle &= 0 \\ \langle h^{\mathrm{bot}} | H_{\mathrm{VB}} | h^{\mathrm{mid}} \rangle &= 0 \end{aligned} \tag{3.3}$$

Therefore, the Hamiltonian matrices H_{CB} and H_{VB} can be expressed as:

$$H_{\mathrm{CB}} = \begin{pmatrix} E_{\mathrm{CB}}^{\mathrm{top}} & 0 & t_e \\ 0 & E_{\mathrm{CB}}^{\mathrm{mid}} & 0 \\ t_e^* & 0 & E_{\mathrm{CB}}^{\mathrm{bot}} \end{pmatrix} \tag{3.4}$$

and

$$H_{VB} = \begin{pmatrix} E_{VB}^{top} & 0 & t_h \\ 0 & E_{VB}^{mid} & 0 \\ t_h^* & 0 & E_{VB}^{bot} \end{pmatrix} \tag{3.5}$$

On the other hand, if we choose new base vectors as the product of the electron and hole at different layers $|e^{\mathrm{i}}\rangle \otimes |\mathrm{h}^{\alpha}\rangle$, (i, α = top, mid, bot), and create a new Hilbert space of 9 dimensions. We can transform the old Hamiltonians that describe the band picture in the new space as the tensor product:

$$H^{\text{new}}_{\text{CB, i}\alpha j\beta} = H_{\text{CB}} \otimes I = H_{\text{CB, ij}}\delta_{\alpha\beta} \tag{3.6}$$

and

$$H^{\text{new}}_{\text{VB, i}\alpha j\beta} = I \otimes H_{\text{VB}} = \delta_{\text{ij}} H_{\text{VB, }\alpha\beta} \tag{3.7}$$

If we ignore the exchange interaction between the electron and hole constituents, we can define exciton states as:

$$\begin{aligned} |\text{X}^{\text{top}}\rangle &\equiv |e^{\text{top}}\rangle \otimes |\text{h}^{\text{top}}\rangle \\ |\text{X}^{\text{bot}}\rangle &\equiv |\text{e}^{\text{bot}}\rangle \otimes |\text{h}^{\text{bot}}\rangle \\ |\text{DX}_{\uparrow}\rangle &\equiv |\text{e}^{\text{bot}}\rangle \otimes |\text{h}^{\text{top}}\rangle \\ |\text{DX}_{\downarrow}\rangle &\equiv |\text{e}^{\text{top}}\rangle \otimes |\text{h}^{\text{bot}}\rangle \end{aligned} \tag{3.8}$$

Finally, we define the excitons' Hamiltonian as the conduction band edge minus the valence band edge $H_{\text{X, i}\alpha j\beta} \equiv H^{\text{new}}_{\text{CB, i}\alpha j\beta} - H^{\text{new}}_{\text{VB, i}\alpha j\beta}$:

$$H_{\text{X}} = \begin{pmatrix} E^{\text{top}}_{\text{CB}} - E^{\text{top}}_{\text{VB}} & 0 & t_e & -t_h \\ 0 & E^{\text{bot}}_{\text{CB}} - E^{\text{bot}}_{\text{VB}} & -t_h^* & t_e^* \\ t_e^* & -t_h & E^{\text{bot}}_{\text{CB}} - E^{\text{top}}_{\text{VB}} & 0 \\ -t_h^* & t_e & 0 & E^{\text{top}}_{\text{CB}} - E^{\text{bot}}_{\text{VB}} \end{pmatrix} \tag{3.9}$$

The carrier hopping between the top and bottom layers eventually leads to an off-diagonal coupling term between $\text{DX}_{\downarrow\uparrow}$ and intralayer states. After re-arranging the matrix with real and symmetric hopping amplitudes and considering the 1S/2S states, we finally obtain the excitons' Hamiltonian in trilayer WSe_2 as:

$$H = H_0 + H_1 = \begin{pmatrix} \varepsilon_{1\text{S}} & 0 & t_1 & t_1 & 0 & 0 \\ 0 & \varepsilon_{1\text{S}} & t_1 & t_1 & 0 & 0 \\ t_1 & t_1 & \varepsilon_{\text{DX}} - E_Z \cdot d & 0 & t_2 & t_2 \\ t_1 & t_1 & 0 & \varepsilon_{\text{DX}} + E_Z \cdot d & t_2 & t_2 \\ 0 & 0 & t_2 & t_2 & \varepsilon_{2\text{S}} & 0 \\ 0 & 0 & t_2 & t_2 & 0 & \varepsilon_{2\text{S}} \end{pmatrix} \tag{3.10}$$

where t_1 (t_2) stands for the coupling strength between $\text{DX}_{\downarrow\uparrow}$ and intralayer 1S (2S) state.

After diagonalization of $H = H_0 + H_1$ by $H_D = U^{\dagger} H U$, we obtain six eigenstates ($|\text{X}_1\rangle$, $|\text{X}_2\rangle$, $|\text{X}_3\rangle$, $|\text{X}_4\rangle$,$|\text{X}_5\rangle$, $|\text{X}_6\rangle$),

$$\begin{pmatrix} |\mathrm{X}_1\rangle \\ |\mathrm{X}_2\rangle \\ |\mathrm{X}_3\rangle \\ |\mathrm{X}_4\rangle \\ |\mathrm{X}_5\rangle \\ |\mathrm{X}_6\rangle \end{pmatrix} = U^{\dagger} \begin{pmatrix} |1\mathrm{S}^{\mathrm{top}}\rangle \\ |1\mathrm{S}^{\mathrm{bottom}}\rangle \\ |\mathrm{DX}_{\uparrow}\rangle \\ |\mathrm{DX}_{\downarrow}\rangle \\ |2\mathrm{S}^{\mathrm{top}}\rangle \\ |2\mathrm{S}^{\mathrm{bottom}}\rangle \end{pmatrix} \tag{3.11}$$

and eigenenergies $H_D = diag(\varepsilon_1(E_z), \varepsilon_2(E_z), \varepsilon_3(E_z), \varepsilon_4(E_z), \varepsilon_5(E_z), \varepsilon_6(E_z))$, as function of electric field (we can also use the perturbation theory to estimate). These mixed eigenstates are close to the base vectors, except around $\varepsilon_{\mathrm{DX}} \pm E_Z \cdot d \approx \varepsilon_{1\mathrm{S}/2\mathrm{S}}$ regions, where $\mathrm{DX}_{\downarrow\uparrow}$ hybridize with intralayer 1S/2S and anti-crossing features appear. By fitting the resonance features in the measured dR/R data (Fig. 3.5a and Fig. C.1), we obtain the coupling strength $t_1 \approx t_2 \approx 5.5\ meV$. Given that every-other-layer DX has rather different Bohr radius from that of the intralayer one, it is not that surprising that its envelope function can have comparable overlap with 1S and 2S envelope function of intralayer exciton.

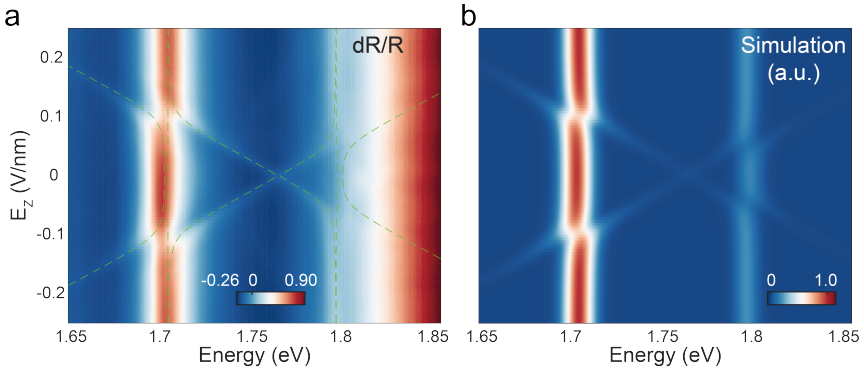

Figure 3.5: Modeling and reconstructing the every-other-layer DXs in trilayer WSe_2. a, E_Z dependence of measured differential reflectance spectra in trilayer WSe_2. The green dashed lines show the curve fitting results based on the Hamiltonian Equation (3.10). **b,** Simulation results after considering the spectral intensity and width.

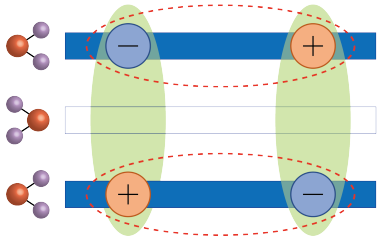

Figure 3.6: Second order carrier hopping. $DX_{\uparrow}$ and $DX_{\downarrow}$ are coupled through intralayer virtual states residing at the top and bottom layers.

In addition, we notice a tiny gap opening between ε_3 and ε_4 (the center of the crossing at 1.767 eV), which becomes even larger at higher hopping amplitude (Fig. C.1). It appears due to the second order perturbation, whose physics picture can be described by a two-step coupling process between the $DX_{\uparrow}$ and the $DX_{\downarrow}$ states with the help from an intralayer virtual state (Fig. 3.6).

We further model the spectral density of each excitonic state as a Gaussian distribution with a bandwidth w_i and intensity I_i ($i = 1S^{top/bottom}$, $DX_{\downarrow/\uparrow}$, $2S^{top/bottom}$), the optical reflectance spectrum as a function of incidence energy ε and electric field E_z is given by:

$$I(\varepsilon,\, E_z) = \sum_j \sum_i I_i \left|U_{ij}\right|^2 e^{-\left(\varepsilon - \varepsilon_j(E_z)\right)^2 / 2w_i^2} \tag{3.12}$$

Figure 3.5b is a plot using $I_{1S}^{top} = I_{1S}^{bottom} = 0.5$, $I_{DX,\downarrow/\uparrow} = 0$, $I_{2S}^{top} = I_{2S}^{bottom} = 0.1$, $w_{1S} = 5.5\ meV$, $w_{2S} = 4.5\ meV$, where we have assumed negligible optical oscillator strength of the every-other-layer DX. Nevertheless, $DX_{\downarrow\uparrow}$ states become visible through hybridization with intralayer 1S/2S states. Therefore, the calculation well reproduces the differential reflectance spectra in Fig. 3.4b, which further supports our interpretation of the results.

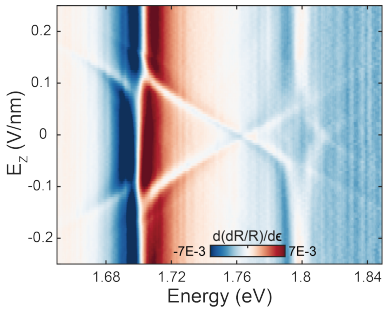

Figure 3.7: Reflectance spectrum differentiated with respective to photon energy. An excited state orbital of $DX_{\uparrow\downarrow}$ becomes visible as a higher-energy X pattern.

We take the derivative of dR/R spectra in Fig. 3.4a versus the energy axis, $d(dR/R)/d\epsilon$. As shown in Fig. 3.7, it reveals subtle spectral features. A second X pattern above the intralayer 2S state appears, centering at 1.813 eV. This X pattern exhibits the stark effect with the same slope corresponding to electric dipole $d \sim 1.4$ e·nm. Therefore, we attribute this second anti-crossing to the higher orbital state of the every-other-layer exciton, which becomes visible through hybridizing with the intralayer 2S state. The energy separation between the ground and excited states of this every-other-layer DX is about 46 meV at $\mathbf{E_Z} = 0$, which sets the lower bound of the binding energy. In comparison to the intralayer 1S-2S exciton energy difference of about 93 meV, the binding energy of the DX is of the same order of magnitude. The observation of such a large energy scale for the every-other-layer binding is remarkable, which suggests the screening effect in trilayer is still strongly suppressed.

3.4 STACKING DEPENDENCE

Every-other-layer DX relies strongly on the spin-valley locked spin superlattice chain. If we break this periodicity in the stacking order, the DX can be switched off. For this purpose, we

measured artificially twisted double bilayer WSe_2 samples. Figures 3.8 a-c show the dR/R intensity plot of a naturally 2H-stacked 4-layer (Fig. 3.8a), near 0° twist (Fig. 3.8b) double bilayers, and near 60 twisted double bilayers (Fig. 3.8c). In the natural 4-layer sample, the X spectral pattern vs $\mathbf{E_Z}$ demonstrates the every-other-layer DX, which is formed between the layer number with same parity, i.e., either $1^{st}/3^{rd}$ layer or $2^{nd}/4^{th}$ layer. Similar X pattern is observed in the zero-degree stacked double bilayers. In contrast, the 60-degree stacked double bilayers shows drastically different spectra features compared to both naturally 2H and zero-degree twisted samples. As shown in Fig. 3.8c, only the 1S intralayer exciton is observed, which is insensitive to $\mathbf{E_Z}$.

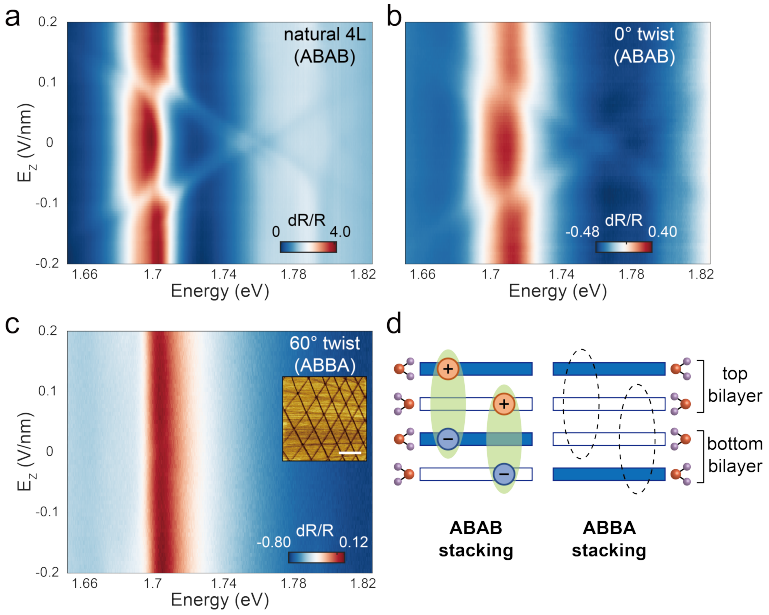

Figure 3.8: Stacking-dependent every-other-layer DX. a,b, Electric field dependence of dR/R from natural four-layer (**a**) and near-0° twisted double-bilayer WSe_2 (**b**). **c,** Electric field dependence of dR/R from near-60° twisted double-bilayer WSe_2. The inset shows that triangular domains appear in the piezo response force microscopy image of a near-60° twisted double-bilayer WSe2 device. Scale bar, 200 nm. **d,** Cartoon of every-other-layer DX formation in double bilayers with ABAB stacking in comparison with the ABBA stacking.

The 0° twisted sample resembles the natural 4-layer WSe_2 in their ABAB stacking order, where each layer sits on top of another with 180° rotation (Fig. 3.8d). Due to the small twist angle

between the double bilayers, moiré superlattices form at the interface between the two WSe_2 bilayers[34,97,98]. In Fig. 3.8b, the intralayer 1S (1.706 eV), 2S (1.803 eV) and DX (1.763 eV) states are all observed as well as the anti-crossing features near the intralayer 1S resonance. An electric dipole of 1.4 e·nm is obtained, evidence for the every-other-layer configuration of the DX. Features from 0° twist sample exhibits broader linewidth than natural 4-layer sample, possibly due to the inhomogeneity of 2H domain structures formed at the twisted interface. In comparison, the every-other-layer DX is absent from the 60° twisted double bilayer WSe_2 (Fig. 3.8c). Different from 0° twisted and natural 4-layer samples, 60° twisted sample is stacked in an ABBA order (Fig. 3.8d). The comparison of the two stacking further confirms our understanding of the spin-valley locked superlattices in the 2H structure, which is necessary for the formation of every-other-layer DX.

3.5 LAYER NUMBER DEPENDENCE

Finally, we examine DXs in samples with different thickness. As demonstrated in Chapter 2.2 and Chapter 2.3, we do not observe exciton feature with such a large electrical dipole in either monolayer or bilayer samples (see Fig. 2.4c and Fig. 2.5f). This confirms the basic unit for such an exciton is trilayer. While in samples thicker than 4 layers, fine structures of multiple X patterns appear in the differential reflectance spectra. In 5-layer sample (Fig. 3.9a), there are two X patterns with a modest energy splitting of about 20 meV. Possible mechanisms to split the X pattern include a second order carrier hopping process which couples two DXs through an intralayer exciton as the virtual intermediate state. We use DX_{ij} to denote the DX between the ith and j^{th} layer. As schematically shown in Fig. 3.9c, through hole hopping process between the 1st and 3rd layer, the DX D_{13} is firstly coupled to the intralayer state at the 3rd layer, which is then coupled to another dipole-up exciton DX_{35} through an electron hopping process between the 3rd and 5th layer. However, given the carrier hopping amplitude $t \sim 5.5$ meV we previously derive from fitting the trilayer

WSe_2's spectra, the above second order coupling process between two DXs is expected to give a smaller splitting than what we observed.

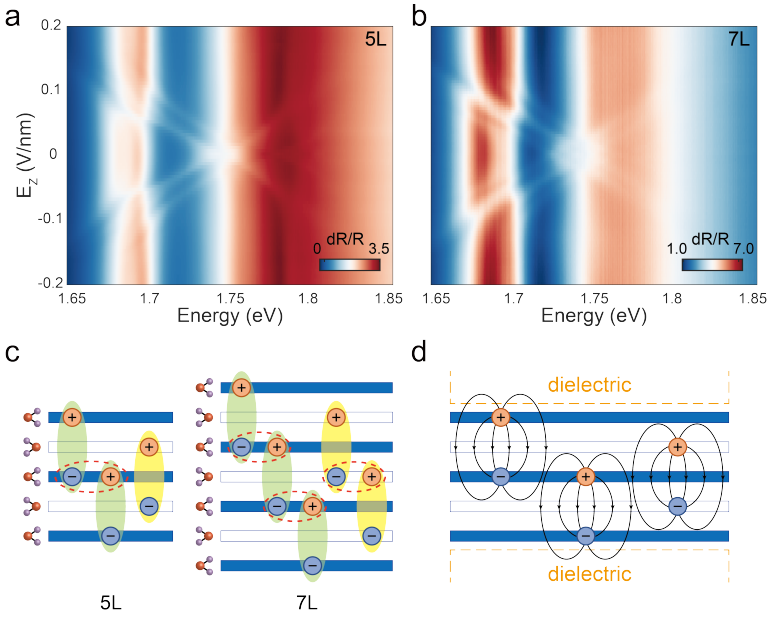

Figure 3.9: Layer number dependence and multiple anti-crossings. a,b, Multiple anti-crossings appear in the electric field dependence of dR/R from five-layer (**a**) and seven-layer (**b**) 2H-WSe_2. **c,** Hopping of DXs in the out-of-plane direction through a virtual intralayer state in five and seven layers. Dashed red ellipses stand for the intralayer exciton states, which are coupled to two adjacent DXs. **d,** Illustration of different dielectric environment for DXs in a five-layer geometry.

A more plausible explanation is the inhomogeneous dielectric environment along the vertical axis of the device stacking[22,99,100]. The large layer separation of the every-other-layer DX leads to a larger Bohr radius, making it more sensitive to the surrounding dielectric environment. For example, comparing the DX_{13} and DX_{24} in a five-layer (Fig. 3.9d), the former is influenced more by the hBN layers which has different dielectric screening from the TMD layers. Such different dielectric environment for different DXs results in slight difference in their binding

energies. Likewise, in 7-layer sample, DX_{13} (DX_{57}), DX_{24} (DX_{46}) and DX_{35} will split into three different branches for the same reason, which agrees with what we observed in Fig. 3.9b. In comparison, in 4-layer WSe_2, DX_{13} and DX_{24} do not couple to each other, and have the same dielectric environment under the symmetric geometry with hBN capping layer and substrate. The two thus have similar resonance energy (Fig. 3.8a).

Furthermore, using a similar method, we can fit and reconstruct the spectra of 5-layer WSe_2. The corresponding Hamiltonian becomes:

$$H = H_0 + H_1 = \begin{pmatrix} H_{1S} & 0 & 0 \\ 0 & H_{DX} & 0 \\ 0 & 0 & H_{2S} \end{pmatrix} + \begin{pmatrix} 0 & H_{1S-DX} & 0 \\ H_{1S-DX}^{\dagger} & 0 & H_{2S-DX}^{\dagger} \\ 0 & H_{2S-DX} & 0 \end{pmatrix} \tag{3.13}$$

where

$$H_{1S/2S} = \begin{pmatrix} \varepsilon_{1S/2S}^{(1)} & 0 & 0 & 0 & 0 \\ 0 & \varepsilon_{1S/2S}^{(2)} & 0 & 0 & 0 \\ 0 & 0 & \varepsilon_{1S/2S}^{(3)} & 0 & 0 \\ 0 & 0 & 0 & \varepsilon_{1S/2S}^{(4)} & 0 \\ 0 & 0 & 0 & 0 & \varepsilon_{1S/2S}^{(5)} \end{pmatrix} \tag{3.14}$$

$\varepsilon_{1S/2S}^{(i)}$ standing for the energy of intralayer 1S/2S exciton within the ith layer, and

$$H_{DX} = \begin{pmatrix} \varepsilon_{DX}^{(13)} & 0 & 0 & 0 & 0 & 0 \\ 0 & \varepsilon_{DX}^{(31)} & 0 & 0 & 0 & 0 \\ 0 & 0 & \varepsilon_{DX}^{(35)} & 0 & 0 & 0 \\ 0 & 0 & 0 & \varepsilon_{DX}^{(53)} & 0 & 0 \\ 0 & 0 & 0 & 0 & \varepsilon_{DX}^{(24)} & 0 \\ 0 & 0 & 0 & 0 & 0 & \varepsilon_{DX}^{(42)} \end{pmatrix} \tag{3.15}$$

$\varepsilon_{DX}^{(ij)}$ standing for the energy of every-other-layer DX between the ith and j^{th} layer.

H_{1S-DX} (H_{2S-DX}) stands for the off-diagonal coupling between 1S and DX (2S and DX) states through the electro or hole interlayer hopping.

$$H_{1S-DX/2S-DX} = \begin{pmatrix} t_{1/2} & t_{1/2} & 0 & 0 & 0 & 0 \\ 0 & 0 & 0 & 0 & t_{1/2} & t_{1/2} \\ t_{1/2} & t_{1/2} & t_{1/2} & t_{1/2} & 0 & 0 \\ 0 & 0 & 0 & 0 & t_{1/2} & t_{1/2} \\ 0 & 0 & t_{1/2} & t_{1/2} & 0 & 0 \end{pmatrix} \tag{3.16}$$

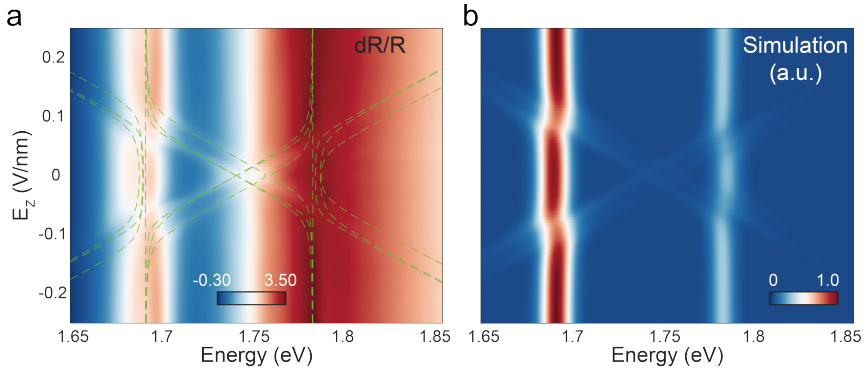

Figure 3.10: Modeling and reconstructing the every-other-layer DXs in five-layer WSe_2. a, E_Z dependence of measured differential reflectance spectra in five-layer WSe_2. The green dashed lines show the curve fitting results based on the Hamiltonian Equation (3.13). **b,** Simulation results after considering the spectral intensity and width.

Using the same fitting parameters $t_1 = t_2 = 5.5\,meV$ as in the trilayer case, the eigenenergies of the five-layer Hamiltonian are plotted as the green dashed curves in Fig. 3.10a. Note that, considering the different dielectric environment of $DX_{13/35}$ and DX_{24}, we have assigned different values to $\varepsilon_{DX}^{(24/42)}$ and $\varepsilon_{DX}^{(13/31/35/53)}$. Fig. 3.10b shows the optical spectrum, with the spectral intensity and width parameters $I_{1S}^{(i)} = 0.2$, $I_{DX,\downarrow/\uparrow}^{(ij)} = 0$, $I_{2S}^{(i)} = 0.06$, $w_{1S} = 5.5\,meV$, $w_{2S} = 4.5\,meV$.

3.6 SUMMARY AND APPLICATIONS

Semiconductor superlattices underly a broad range of fundamental science and technological applications[92]. 2H-stacked transition metal dichalcogenide thin films host unique valleytronic superlattices where even/odd layers form barriers/quantum wells depending on the spin-valley indices. In multilayer WSe_2, we found a DX with Coulomb-bound electron and hole in every-other-layer configuration, resulting in a large electrical dipole of 1.4 e·nm, twice that of interlayer excitons in TMD heterobilayers. These DXs have tunable exciton hybridization, large binding energy, and layer-thickness dependent spectroscopy features. Combined with demonstrated layer stacking control, these findings may open avenues in engineering many-body effects of interacting bosons, as well as nanophotonics and quantum optoelectronics via valleytronic superlattice engineering.

CHAPTER 4. ENGINEERING FERROELECTRICITY IN RHOMBOHEDRAL-STACKED TRANSITION METAL DICHALCOGENIDES

In the last chapter, we compared the ABAB-stacked WSe2 with the ABBA counterpart, and drew the conclusion that the every-other-layer dipolar exciton only appears in ABAB stacking order. In this chapter, we are going to focus on the ABBA stacking order because there are also exciting physical phenomena such as ferroelectricity emerging from the system. We will first introduce the origin of the spontaneous electric polarization as well as the ferroelectricity in twisted Rhombohedral-stacked (3R-stacked) TMD systems and discuss the domain effects. We will then demonstrate the scanning probe imaging results of the alternatingly polarized domain distribution, which serves as direct evidence for the existence of the ferroelectricity. Finally, we will report the observation of dipolar excitons coupled with the ferroelectricity as indirect evidence. In this chapter, the twisted Rhombohedral-stacked TMD is suggested as a new candidate of ferroelectric thin films with potential applications due to the light-matter interactions.

4.1 FERROELECTRICITY IN A DIELECTRIC

In undergraduate textbooks, ferroelectricity has been described as a characteristic of certain materials that have a spontaneous electric polarization that can be reversed by the application of an external electric field[101,102]. Ferroelectric materials have two properties: the remanent polarization at zero external electric field and the hysteresis effect of the electric polarization while sweeping the external field at opposite directions. Known as the P-E curve (Fig. 4.1), when we plot the electric polarization as a function of the external electric field, we notice that there is a

hysteresis loop between the opposite field-sweeping directions, and that the electric polarization at zero field remains nonzero, depending on the field-sweeping history (Fig. 4.1b). Practically, it worth noting that the switching of the polarized direction versus the external electric field is not vertical due to the domain effects, i.e., different domain has unique coercive field and remanent polarization (Fig. 4.1c). Ferroelectric materials have long been used in applications such as ferroelectric random-access memory (FeRAM) for computer non-volatile memory storage[103-106] and ferroelectric tunnel junction (FTJ) due to an electroresistance effect[107].

In condensed matter physics, 2D ferroelectricity comes from the broken mirror symmetry. Normally, monolayer TMD does not have ferroelectricity. Hexagonal-stacked TMD is not ferroelectric due to the mirror-symmetric crystal structure in its repeating unit. However, by engineering its stacking order (Chapter 4.2) or modifying its growth conditions[108], its mirror symmetry can be broken. In Fig. 4.2, schematics of 3R-stacked TMD structure is shown. In 3R-stacked TMD bilayer, its top and bottom layers are relatively shifted to reach the lowest stacking energy. Due to the broken mirror symmetry, 3R-stacked TMD bilayer has two possible structures – MX and XM, where the transition metal atoms sit on top of or beneath the chalcogen atoms, respectively. These two stacking structures are mirror flipping copies of each other (Fig. 4.2).

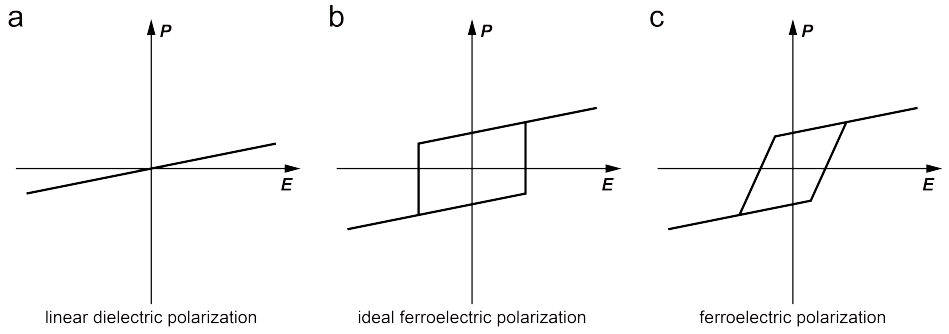

Figure 4.1: Hysteresis loop in P-E curves. a, P-E curve for linear dielectric polarization. **b,c,** P-E curves for ideal (b) and real (c) ferroelectric materials.

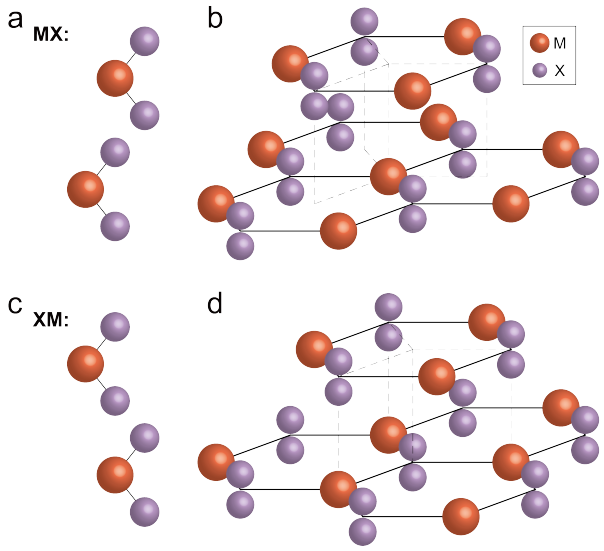

Figure 4.2: MX and XM stackings in R-stacked TMD. a,b, Atomic stacking orders of MX (**a**) and XM (**b**) in R-stacked bilayer TMD.

Surprisingly, it has been recently discovered that spontaneous electric polarizations can appear in 3R-stacked TMD[109] because of charge transfer. Due to the lateral interlayer displacement between top and bottom layers in XM (MX) stacking structure, electrons at the K valley can only tunnel between the conduction band of the top (bottom) layer and the valence band of the bottom (top) layer due to the selection rule[24-26]. The asymmetric interlayer coupling mixes the wave functions from different layers, causing the Wannier center of the valence band of the bottom (top) layer to shift toward the top (bottom) layer. The offset of the overall Wannier center results in an out-of-plane spontaneous electric polarization ($\boldsymbol{P}$)[26,110-113], with a potential difference

$$\Delta V = |\boldsymbol{P}|d/\varepsilon \tag{4.1}$$

where ε is the dielectric constant and d is the interlayer distance.

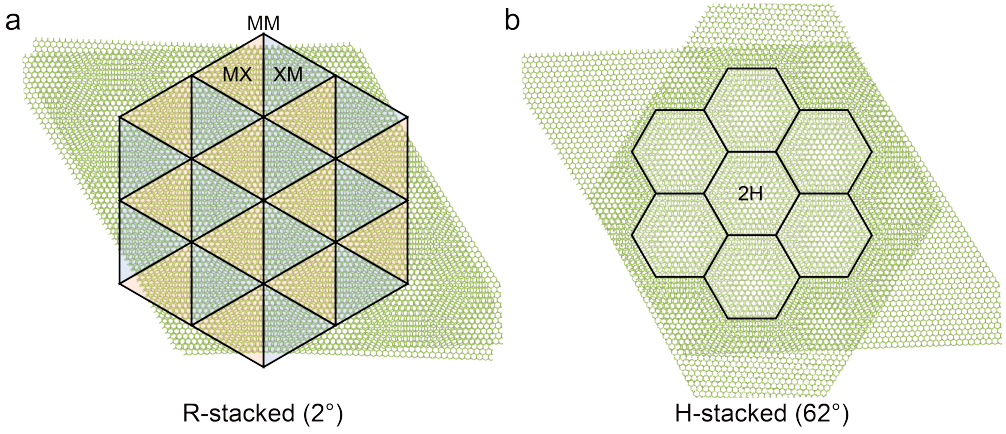

Figure 4.3: Lattice reconstruction in twisted TMD. a,b, Schematics of lattice reconstructions and the consequent domain distributions in R-stacked (**a**) and H-stacked (**b**) twisted bilayer TMD.

However, the existence of spontaneous electric polarization is not equivalent to ferroelectricity, because the ability of flipping the electric polarization direction needs to be examined. In a homogeneous 3R-stacked TMD bilayer system, its spontaneous electric polarization also homogeneously points to the same out-of-plane direction, depending on whether it's MX or XM. The only way to flip its spontaneous electric polarization's direction (without flipping the bilayer flake itself) is by transforming the bilayer's stacking order between MX and XM, which requires a minimum lateral interlayer shift of a material's lattice constant. The amount of energy barrier that the bilayer needs to overcome to homogenously shift one layer by a lattice constant is huge and therefore impossible to realize.

On the other hand, a switchable electric polarization can be realized in a twisted TMD system[69,82,109,114]. If two TMD monolayers are stacked in a parallel crystal orientation way, but with a small misalignment angle (less than 5°), moiré pattern, or moiré superlattice, will be formed as a spatial interferometry between the top and bottom TMD's hexagonal lattices (Fig. 4.3). Different from the spin-valley locked superlattice mentioned in Chapter 3, the moiré superlattice is an in-plane distributed periodic structure. Triangular domains composed of MX and XM stacking regions will be formed along the interface and correlated with the moiré superlattice. This is because MX and XM stacking orders are the local energy minima in the parallel-stacked form.

After lattice relaxation, MX and XM stackings will homogeneously fill the triangular domains in an alternating configuration, with mirror-symmetric (non-ferroelectric) MM stacking order residing at the corner and appearing at the domain walls[115-120] (Fig. 4.3a). As a result, triangular domains with alternating electric polarization are formed, and interfacial ferroelectricity is realized through domain size expansion and contraction. Additionally, similar interfacial ferroelectricity has also been observed in twisted hexagonal Boron Nitride (hBN) systems[80-82]. On the contrary, hexagonal domains appear after lattice relaxation in 2H-stacked twisted TMD (Fig. 4.3b) and 3R-stacked twisted TMD with a large twist angle[116].

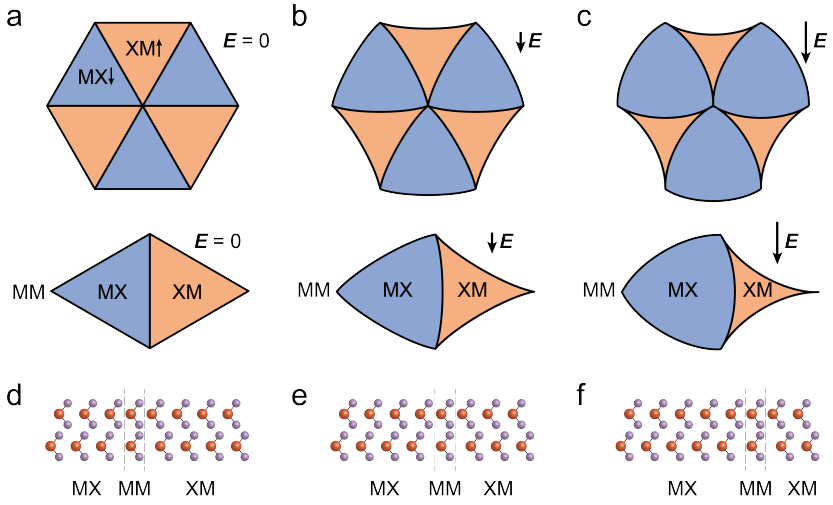

Figure 4.4: Domain wall dynamics under external electric field. a,b,c, Schematics of domain shape change under an out-of-plane electric field. **d,e,f,** Domain wall dynamics illustrated by atomic stacking orders.

At zero field, triangular domains all have straight domain walls and equal size, resulting in a zero net electric polarization. However, while gradually applying a pointing-down electric field $-E_Z$, the XM domains which have pointing-up spontaneous polarizations will contract their sizes, due to a rising electrostatic energy, and the MX domains with pointing-down polarizations will become energy-favored and expand (Fig. 4.4). The domain size expansion and contraction results from the competence among the stacking's intralayer elastic energy from the intralayer stress, its

interlayer stacking energy from the interlayer van der Waals (vdW) interaction, and its electrostatic energy from the coupling between the local dipole moment and the electric field as well as the bilayer's dielectric response[120,121]. To reach a balance among these three interactions while applying an external electric field, the domain walls will move through an in-plane interlayer shear motion. Only a small portion of the XM stackings near the domain boundaries will become MX stackings due to the interlayer shear motion (Figs. 4.4d, e, f). The energy cost of the domain wall dynamics is therefore much smaller than shifting the entire layer in a homogeneous 3R-stacked bilayer mentioned earlier.

The transition will reach a saturation point where almost all the XM area is replaced by the MX stacking order. While we gradually decrease the out-of-plane electric field from negative back to zero, the XM domains will recover their area. But they are still slightly smaller than the MX domains due to resistance such as the interlayer friction and domain wall stiffness. Consequently, a remanent electric polarization will appear after sweeping the out-of-plane external electric field back to zero (Figs. 4.5c, d).

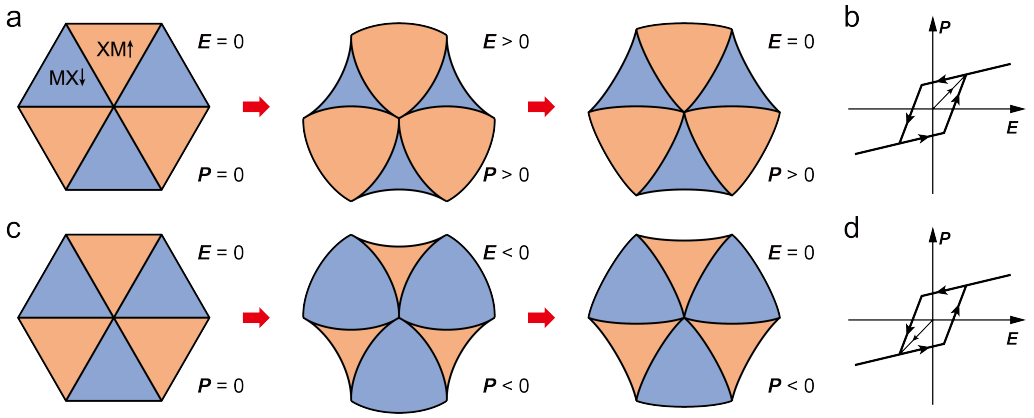

Figure 4.5: Mechanisms of the hysteresis loop in twisted TMD. a, Illustrations of domain area dynamics while increasing the external electric field and sweeping back and forth. **b,** P-E curve of the processes in **a**. **c,d,** Sample plots for decreasing the external electric field and sweeping back and forth.

On the other hand, same situation happens when applying a pointing-up electric field. The up-polarized XM domains will become energy-favored and expand while the MX domains will contract their sizes, resulting in a pointing-up net electric polarization. The XM domains remain slightly larger than the MX domains after recovering back to zero electric field, leaving a pointing-up remanent electric polarization. Furthermore, a hysteresis loop is formed while sweeping the external electric field back and forth (Figs. 4.5a, b). Therefore, interfacial ferroelectricity is realized with the existence of a remanent electric polarization and a hysteresis loop.

4.2 DEVICE FABRICATIONS

The PC stamp dry transfer technique mentioned in Chapter 1.3.1 is of vital significance for 2D nanodevice fabrication. In order to investigate the interfacial ferroelectricity, scanning probe techniques are carried out to image the triangular 3R-stacked domains with alternating spontaneous electric polarizations. The device structure is thus required to have an exposed surface of the twisted TMD, since any encapsulation of 2D materials will significantly decrease the signal contrast and give an inaccurate measurement of the surface potential difference between adjacent 3R-stacked domains. On the other hand, if normal PC stamp dry transfer is used to fabricate the exposed twisted TMD surface, clusters of polymer residues will be sticked to the TMD surface and hard to remove after wash-off. Although the AFM tip cleaning technique mentioned in Chapter 1.3.3 can be used to clean the sample surface, TMD layer might be easily torn by the tip because TMD is much more fragile compared to other 2D materials such as hBN. For this purpose, we invent a solvent-free, PC stamp flip transfer technique.

Before being picked up by a PC stamp, the bottom surface of an exfoliated flake is atomically clean. This is because the bottom surface has never been in contact with residues after being peeled off from the bulk crystal. If this atomically clean bottom surface can be flipped to the very top, scanning probe imaging such as piezoresponse force microscope (PFM) and Kelvin probe

force microscope (KPFM) can be performed with a high accuracy and signal-to-noise ratio. As mentioned in Chapter 1.3.1, a PC flip transfer technique can be adopted (Fig. 1.6a).

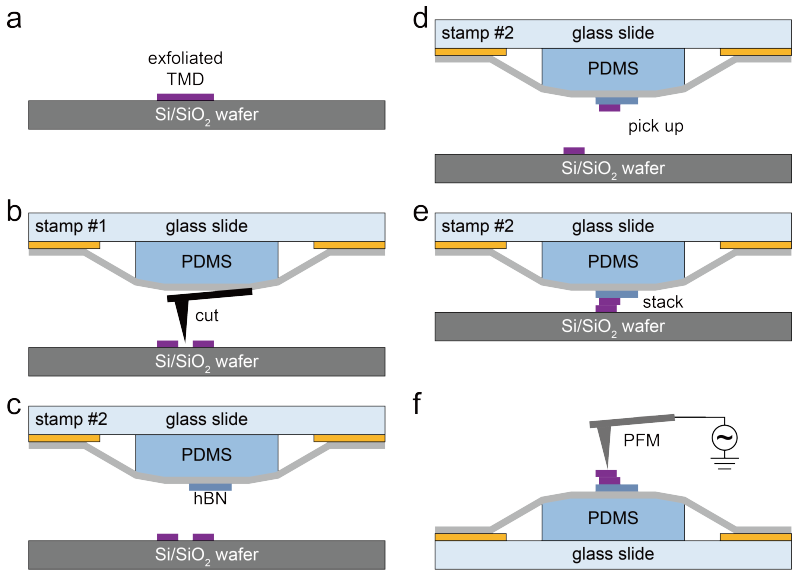

Figure 4.6: Tear-and-stack techniques for fabricating twisted TMD. a,b, Illustrations of cutting TMD flakes. **c,d,e,** Illustrations of stacking the TMD flakes after cutting. **f,** Illustration of performing PFM during the transfer.

While making twisted TMD samples with moiré superlattice, a precise control of the misalignment angle between the top and bottom layers is of vital importance because the moiré superlattice periodicity, or moiré wavelength, is determined by the misalignment between the top and bottom layers following (1.4). Physical properties such as flat band formation[76,77,118,119,122] is determined by the moiré wavelength. Lattice relaxation as well as the intralayer elastic energy and the interlayer stacking energy will also be influenced by the domain size. For instance, the domain shape can be modified at a larger misalignment angle[115].

For this purpose, we adopt a tear-and-stack technique, where an exfoliated 2D flake can be torn apart into two pieces and then stacked into a homobilayer[123,124]. After cutting the 2D flake into two pieces (Figs. 1.6b, c), one piece will be picked up first and rotated by a certain angle by the

rotary stage, before being stacked onto the other piece (Figs. 4.6d, e). A precise alignment is thus realized. Normally, a relatively soft 2D flake, such as graphene or TMD, is torn by the sharp edge of a thick hBN flake on the stamp, due to a much greater adhesion from hBN (vdW interaction) than the PC film. During the transfer, a straight edge of the hBN flake on the stamp should be aligned to the middle of the target flake. The slightly tilted stamp should approach the chip at an extremely slow rate, until the hBN edge covers half of the target flake, while the other half remains atomically clean and not in contact with the stamp. The target flake is likely to be torn while slowly lifting the stamp at a lower temperature. Half of the target flake will be picked up by the stamp while the rest remains on the chip (Fig. 4.6d).

Furthermore, improvement has been made by using the tip cutting technique (mentioned in Chapter 1.3.2), which is also a mutation of the PC stamp dry transfer technique. In this method, flakes can be mechanically cut by a stamp holding a sharp tip. Lateral movement of the stage while the tip is in contact with the substrate can cut the flake along the path (Fig. 4.6b). By aligning the straight edge of the hBN flake and the cut on the target flake, half of the flake is easily picked up and then stacked onto the other half without any concern. This method can be applied to assist the tear-and-stack technique by lowering the failure chance that the target flake might be dragged or even be picked up as a whole by the stamp if it's too small (less than 8 μm).

Additionally, linear-polarization-resolved second harmonic generation (SHG) technique mentioned in Chapter 1.3.2 is also used to characterize the crystal orientation of a 2D flake that has a broken inversion symmetry such as odd-layer TMD and hBN[38-41]. The relative angle between two odd-layer flakes can be obtained by fitting their SHG intensities. Even for even-layer TMD flake which has an odd-layer part attached, the crystal orientation can be determined by performing SHG on its odd-layer attachment. Therefore, SHG serves an ultimate weapon for fabricating twisted TMD devices (both homobilayer and heterobilayer) and characterizing their misalignment angle.

Combining the tear-and-stack, AFM tip cutting and SHG techniques, dual-gated optical devices with a certain moiré wavelength can be fabricated following the exact same processes in Chapter 1.3.

4.3 VISUALIZATION OF INTERFACIAL FERROELECTRICITY

To find the interfacial ferroelectricity in Chapter 4.1, a direct observation of the triangular 3R-stacked domains with alternating spontaneous electric polarization by scanning probe techniques such as AFM[82,109], scanning electron microscope (SEM)[114] and transmission electron microscope (TEM)[69].

As mentioned in Chapter 1.3.2, piezoresponse force microscope (PFM) is always used to determine the twist angle of a moiré superlattice in an accurate way during the PC stamp dry transfer process. PFM is a mutation of contact-mode AFM. An AC bias is applied between the tip and sample that induces a periodic deformation of the sample (Fig. 4.7b). Local electromechanical response is then collected by the tip[34,125]. For marginally twisted flakes with a moiré superlattice, domain boundaries between adjacent moiré sites have the greatest strain-gradient and therefore give strong electrical polarization signal due to the flexoelectric effect.

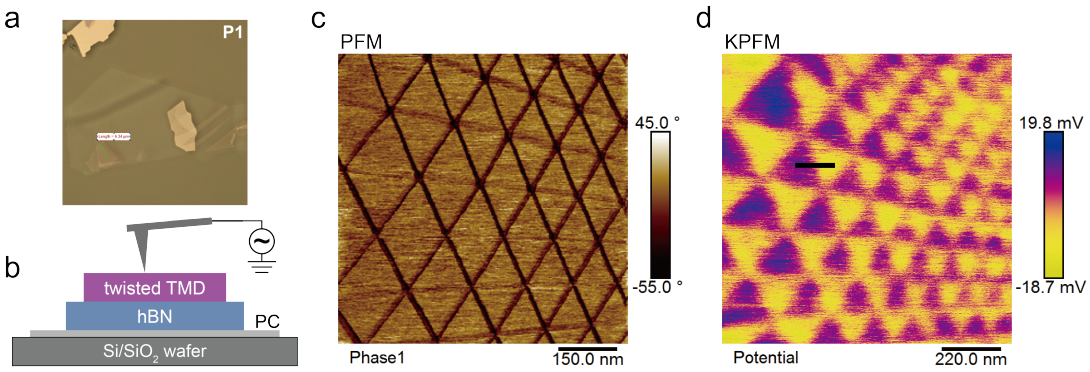

Figure 4.7: Visualization of interfacial ferroelectricity. a, Optical microscope image of the flipped device P1. The label indicates the scale of the sample size is 7 μm. **b,** Side view of a flipped device and PFM measurement. **c,d,** PFM (**c**) and KPFM (**d**) images of the same area on device P1.

We first perform PFM measurement on a flipped device which is specially fabricated for scanning probe imaging by the PC flip stamp transfer technique (Figs. 4.7a, b). We use SCM-PIT-V2 cantilever (75 kHz resonant frequency and 3.0 N/m spring constant) as the tip due to its sharp profile and metal coating. The contact force between the cantilever and the TMD top surface is set to ++0.08V voltage amplitude, which is much lighter than the AFM tip cleaning technique (Chapter 1.3.3) to avoid destruction but is high enough to make sure the tip won't fly off the surface. The drive amplitude of the tip generating periodic deformation is set to be 200 mV. We find the resonance frequency of the electromechanical response between the tip and the TMD around 750 kHz. The amplitude and phase from both horizontal and vertical channels are read by two lock-in amplifiers. However, the vertical channel always contains mixed component from the horizontal channel[34] which dominates the total signal in our case due to the cantilever. In addition, the PC film that is left at the bottom of the device won't reduce the AC grounding of the TMD surface due to a considerate AC conductance at 750 kHz[126].

Figure 4.7c demonstrates the horizontal PFM phase signal of device P1, which uses double bilayer WSe_2 as the TMD layers in a parallel stacking order (ABBA) to generate interfacial ferroelectricity from the B-B interface (the middle two layers). Another reason to use ABBA double bilayer WSe_2 is to correlate with the optical characterizations in Chapter 4.4, due to the rich excitonic responses in bilayer TMD systems. Hexagonally distributed superlattice pattern of triangular domains is visualized. The inhomogeneity of the triangle sizes possibly comes from the strain induced during the fabrication process, including annealing, tip cutting and pressure during the transfer. From the amplitude and phase channels, the signals from the domain walls dominate and shape the boundary of the triangular domains. The domain walls are typically tens of nanometer wide and contain a large strain gradient due to the different stacking orders on both sides, while the strain gradients are negligible inside the domains. The average stacking order through the domain walls should be parallel stacking without a lateral displacement between the top and bottom layers, as known as MM stacking (Figs. 4.4d, e, f). On the other hand, the topography of the twisted region is measured simultaneously with the PFM amplitude and phase channels. From the topography channel, the strain gradient that gives a strong PFM signal at the domain walls does not have a significant height difference. Furthermore, the weak patterns from

the topography channel can also be caused by the electronic crosstalk from the PFM channel. Therefore, the PFM results confirm our understanding of the lattice relaxation and domain formation in parallelly twisted TMD.

To correlate with the domain wall distribution from the PFM measurements, the distribution of the surface potential, which is caused by the alternating domain polarizations, should also be measured and performed on the same region. For this purpose, Kelvin probe force microscope (KPFM) technique is carried out to visualize the surface potential of the twisted TMD. KPFM is also a mutation of AFM technique in a non-contact mode[127,128]. Based on a similar mechanism as a parallel plate capacitor, where the conductive cantilever (SCM-PIT-V2) and the grounded sample surface become the parallel plate with a fixed distance, the potential difference in between is then measured as a modulation to the cantilever's AC-driven oscillation and is converted to the surface work function. To keep a fixed distance between the cantilever and the sample surface, the tip scans twice on a single line. During the first scan, KPFM works as a normal non-contact mode AFM and measures the topography of the sample surface. During the second scan, the tip descends to a certain scan height (5-20 nm in our case) and follows the stored surface topography data to maintain a fixed distance between the cantilever and the sample surface, while responding to the surface potential.

Figure 4.7d demonstrates the KPFM results in the potential channel of the same region of interests in device P1. Hexagonally distributed superlattice pattern of triangular domains with alternating colors is visualized. Different from the PFM results, adjacent triangular domains present drastic potential difference signal while the domain walls do not have a strong response anymore. By correlating with the PFM results, we identify that the triangles in the KPFM image align with the triangular domain walls in the PFM image, meaning that the alternating surface potentials come from the triangular domains, which is originally from the lattice relaxation while forming the moiré superlattice. This thus confirms the connection between the ferroelectricity and the moiré superlattice. Furthermore, we notice that the resolution of the KPFM imaging is lower than the PFM technique, due to a larger distance between the tip and the sample. The tip thus collects an average value over a certain range. The alternating triangles become blurred when the domain size becomes smaller than 100 nm. Furthermore, due to the non-contact mode, charge

accumulation might become severe over time especially when the grounding to the sample degrades.

The potential difference between adjacent triangles is around 20 mV. We note that even though the domain sizes are inhomogeneous in device P1, the potential differences are the same over the twisted region. Furthermore, multiple twisted double bilayer WSe_2 devices are fabricated and examined, while the same value is obtained (Fig. B.1 and Fig. B.2). More surprisingly, the same potential difference value is also measured in domains with irregular shapes. After measuring device P2 (Fig. B.1), it dropped onto the floor and a strong and sudden strain was induced to the sample, causing the domain distribution to reconstruct. Multiple triangular domains are merged and form a huge domain with an irregular shape. When we try to correlate its PFM and KPFM images again, we find the potential difference between two huge domains still equal to 20 mV (Fig. B.2b). The independence of potential difference on domain size (at a small twist angle) further supports our understanding that the stacking order within a triangular is relaxed into either XM or MX configuration, which generates the spontaneous electric polarization. However, in different TMD systems, the potential difference can vary with materials and number of layers[109].

Furthermore, a 150 nm moiré superlattice periodicity is measured in both PFM and KPFM images of device P1. We can thus determine the misalignment angle between the top and bottom WSe_2 bilayers to be around 0.13°, using (1.4) and setting $\delta = 0$ and $a = 0.33$ nm.

4.4 DIPOLAR EXCITONS COUPLED WITH INTERFACIAL FERROELECTRICITY

TMD is well-known for its rich excitonic properties, including the formation of excitons and trions (excitons bound to carriers), due to its direct-to-indirect bandgap transition and the spin-valley locking effect as mentioned in Chapter 3.1. These excited quasiparticles can also be bound to other properties including defects and phonons and generate exotic physics. Therefore, there is also possibility of these excitonic responses coupled with the interfacial ferroelectricity in twisted TMD systems.

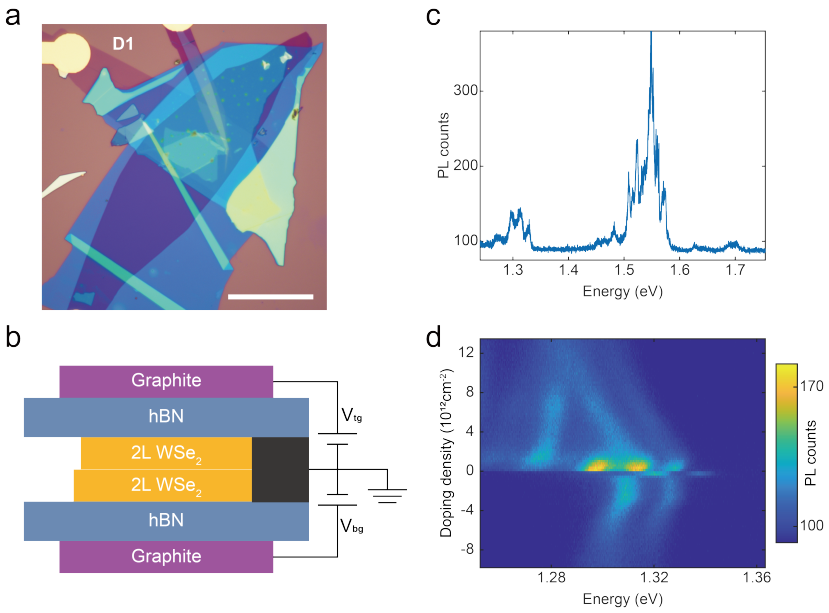

Figure 4.8: PL spectra in ABBA twisted double bilayer WSe_2. a, Optical microscope image of the dual-gated ABBA WSe_2 device D1. Scale bar, 20 μm. **b,** Schematic of the device structure. **c,** PL spectrum of ABBA twisted double bilayer WSe_2 at charge neutrality. **d,** Doping density dependence of the PL emissions at zero electric field.

In this chapter, we are focusing on double bilayer TMD system for the reasons that bilayer TMD (WSe_2) has an indirect bandgap, and that multiple interlayer and intervalley excitonic transitions can appear with comparable PL emission intensities. Unlike monolayer TMD where the K-valley direct transition dominates the PL, bilayer TMD's PL spectrum is dominated by excitons such as Q-K and Q-Γ transitions and their phonon replicas, as demonstrated in Chapter 2.3 (Ref. [75]). A high-NA (0.6) objective lens (LUCPLFLN40X) allows for the collection of the dark exciton species that have out-of-plane optical dipoles.

Twisted double bilayer WSe_2 devices for optical characterizations are fabricated using transfer, tear-and-stack, lithography and PVD techniques. The top and bottom WSe_2 bilayers form an ABBA stacking order, so that the B-B interface becomes parallel stacked and generates interfacial ferroelectricity. The optical microscope image and the cross section of a typical device is demonstrated in Figs. 4.8a, b. The dual-gated geometry gives an independent control of both the electrostatic doping density as well as the out-of-plane electric field, as demonstrated in (1.3).

Additionally, the metal/graphite contact in this case should be in contact with both the top and bottom TMD layers for a better grounding and a more accuracy control.

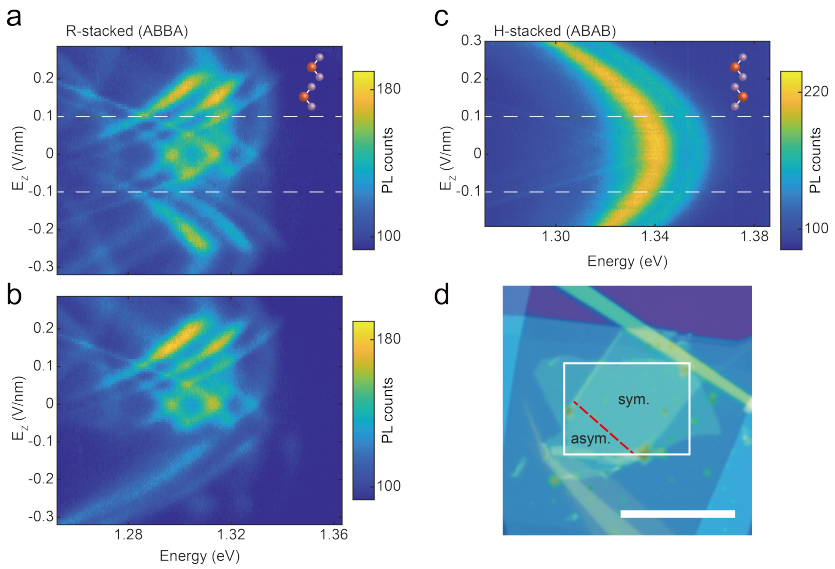

Figure 4.9: Electric field dependent PL emissions in ABBA twisted double bilayer WSe_2. a,b, PL spectra collected at different spots under varying out-of-plane electric field. The field dependent spectra in **b** are asymmetric. **c,** Field dependence of PL emissions in an ABAB twisted double bilayer WSe_2 sample. **d,** Distribution of symmetric (**a**) and asymmetric (**b**) field dependent patterns on the sample. Scale bar, 20 μm.

The PL spectra of more than ten ABBA-twisted double bilayer WSe_2 devices are measured and share similarities at charge neutrality, as shown in Fig. 4.8c as device D1's PL (with 5-μW laser power and 30-second exposure time). Ranging from 700 nm (1.77 eV) to 1000 nm (1.24 eV) PL wavelength, the PL spectrum of an ABBA-twisted double bilayer WSe_2 can be divided into three parts.

First, the intravalley excitons at the K valley of WSe_2 can always be found at around 1.7 eV. Similar to monolayer (Fig. 2.3), bilayer (Fig. 2.5a) and trilayer (Fig. 3.3) WSe_2's PL, they have very weak emissions in the PL spectra due to a higher energy and thus smaller population, while they dominate the differential reflectance (dR/R) spectra because they are momentum-direct

transitions. Compared to monolayer WSe_2, the intravalley species in multi-layer WSe_2 have an energy deviation (redshift) possibly due to a different dielectric screening.

The strongest PL emission can be found in the range from 1.47 eV to 1.59 eV, which can be attributed to the PL from the excitons recombined within one single WSe_2 bilayer flake, or intra-bilayer response. Compared to the Q-K and Q-Γ transitions from the isolated WSe_2 bilayer from Chapter 2.3 (Ref. [75]), they share the same photon energy. But sharp peaks appear in the intra-bilayer PL of the ABBA-twisted double bilayer, which are possibly caused by the moiré potential modulation[67].

The second strongest PL response comes from the range from 1.26 eV to 1.34 eV. These excitonic species come from the inter-bilayer transitions between the top and bottom WSe_2 bilayer flakes. Due to the type-II band alignment of the two bilayers' electronic energy bands, the inter-bilayer excitons have smaller photon emission energies than the intra-bilayer species. In this exciton configuration, the electron and hole reside separately in the top and bottom WSe_2 bilayer flakes, so that the inter-bilayer excitons' wavefunction crosses the interface. Therefore, we should focus on these species because they have a chance to be coupled with the interfacial ferroelectricity.

While zooming in the inter-bilayer transitions in ABBA-twisted double bilayer WSe_2, four separate PL peaks can be resolved at 1.27 eV, 1.30 eV, 1.31 eV and 1.33 eV, with around 10 meV linewidth. They might come from the recombination of an electron at Q valley and a hole at K or Γ in the conduction band. Figure 4.9a demonstrates the electric field dependence of the PL spectra of the inter-bilayer excitons. While applying an out-of-plane electric field through gate tuning, the energy degeneracies are lifted for the four peaks and multiple crossing features are visualized due to the optical Stark effect[16], due to the electrostatic energy deviations of the inter-bilayer excitons' out-of-plane electric dipole moments under an electric field, as described in Chapter 2.3.

Furthermore, we also notice that when we shine the laser spot at different locations on the twisted region, the electric field dependence data vary. At some locations, only half of the pattern can be seen instead of a symmetrical and complete pattern, as shown in Fig. 4.9b. In order to visualize the spatial dependence of this symmetrical-asymmetrical pattern distribution, a fine spatial scan map is measured on a 12.8 μm × 8.0 μm rectangular on the twisted region with 1.6 μm

spatial resolution (Fig. 4.9d). The red dotted line indicates a rough boundary between a symmetrical electric field dependence (to the top right side of the boundary line) and an asymmetrical electric field dependence (to the bottom left of the boundary line).

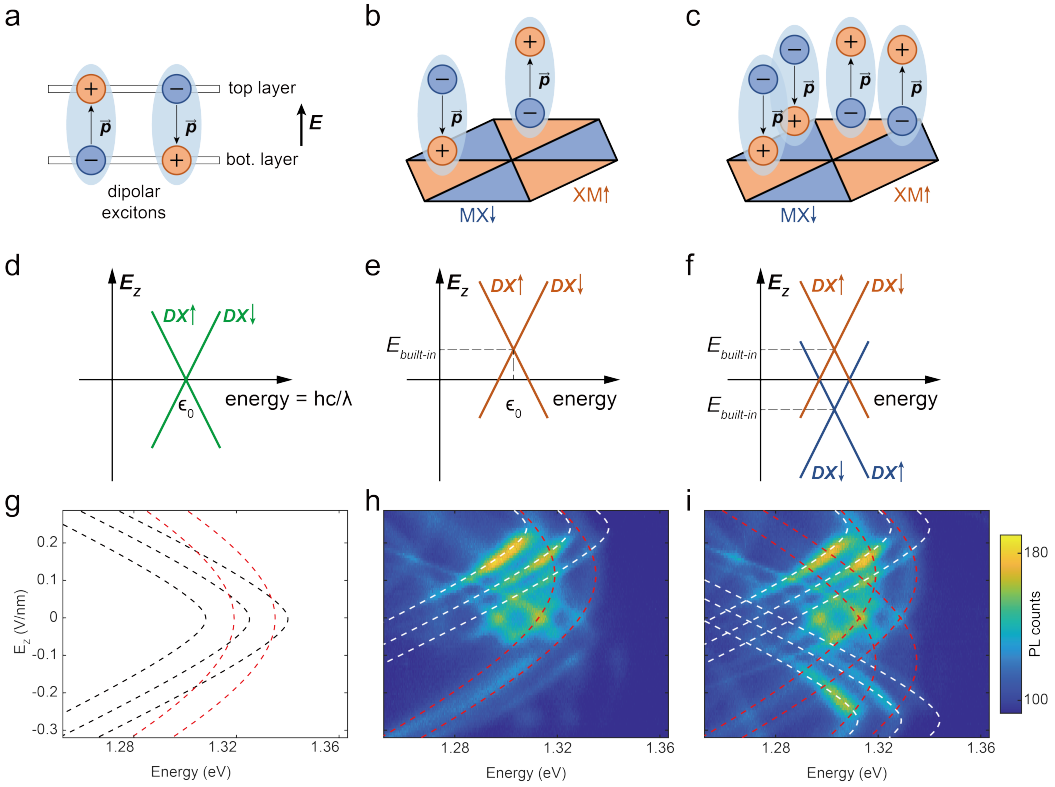

Figure 4.10: Dipolar excitons coupled with interfacial ferroelectricity. a, Schematic of DXs in multilayer TMD under an out-of-plane electric field. **b,c,** DXs residing in XM domains (**b**) and both domains (**c**). **d,e,f,** Schematics of the optical Stack effect in excitonic responses coupled with zero domain polarization (**d**), spontaneous polarizations only from XM domains (**e**), and alternating domain polarizations (**f**). **g,h,i,** Simulated spectra of Q-K and Q-Γ inter-bilayer DXs coupled with zero domain polarization (**g**), spontaneous polarizations only from XM domains (**h**), and alternating domain polarizations (**i**).

The layer separations of each excitonic peak in the field dependence plot are typically from 0.7 e·nm to 0.9 e·nm, using (2.2) to linearly fit the excitonic responses. Figure 4.10d demonstrates the ϵ-E_Z relation of dipolar excitons (DXs) with opposite dipole directions under an electric field.

During the linear regression, we notice that some crossing features are biased as if there is a built-in electric field that is added to the external electric field

$$\epsilon = \epsilon_0 - \boldsymbol{p} \cdot (\boldsymbol{E} + \boldsymbol{E}_{\mathbf{built-in}}) \tag{4.2}$$

so that the crossings are shifted upwards or downwards in the plot. As a comparison, no bias of the crossings is observed in the electric field dependence plots of the ABAB-twisted double bilayer WSe_2 devices (Fig. 4.9c). As a hypothesis, we attribute the built-in electric field in the ABBA-twisted devices to the coupling between the inter-bilayer excitons and the interfacial ferroelectricity.

In a triangular domain with XM-stacked interface, the spontaneous electric field points up from the transition metal atom to the chalcogen atoms, which gives a pointing-down electric field $\boldsymbol{E}' < 0$ between the two WSe_2 bilayers. The total electric field that the DXs with opposite dipole directions becomes $\boldsymbol{E} + \boldsymbol{E}'$, which replaces the $-\boldsymbol{p} \cdot \boldsymbol{E}$ term and becomes $-\boldsymbol{p} \cdot (\boldsymbol{E} + \boldsymbol{E}_{\mathbf{built-in}})$. The crossings from the DXs under electric field are therefore biased upwards in the ϵ-E_Z plot, as the orange curves shown in Fig. 4.10e. This explains the asymmetrical patterns that is found during the spatial scan. When the laser spot (around 1 μm in diameter) only shines on a single and huge domain (with XM-stacked interface), the huge domain in device P2 (Fig. B.2b) for instance, the crossings will only appear at a positive electric field.

On the other hand, while the laser spot covers multiple domains with alternating domain polarizations (for instance the domains in device P1 as shown in Figs. 4.7c, d), it will excite the DXs over these domains with opposite built-in electric field. As a result shown in Fig. 4.10f, two sets of crossings are visualized with the DXs from the MX domains being biased downwards (blue curves) and the DXs from the XM domains being biased upwards (orange curves). Therefore, we can imagine the domain distribution in the twisted region of the device D1 is inhomogeneous, which can be caused by the strain induced during sample fabrication (similar to the sudden strain induced to device P2 mentioned in Chapter 4.3).

Furthermore, we can estimate the values of the built-in electric field that the DXs feel by simulating the excitonic responses. Similar to the model in Chapter 3.3, the single-particle Hamiltonian of electrons and holes can be written as:

$$H_{CB} = \begin{pmatrix} \epsilon_{CB}^{top} & t_e \\ t_e^* & \epsilon_{CB}^{bot} \end{pmatrix} \tag{4.3}$$

and

$$H_{VB} = \begin{pmatrix} \epsilon_{VB}^{top} & t_h \\ t_h^* & \epsilon_{VB}^{bot} \end{pmatrix} \tag{4.4}$$

where $\epsilon_{CB}^{top/bot}$ and $\epsilon_{VB}^{top/bot}$ are the band edge energies of the conduction and valence band at the top/bottom layer, respectively, and $t_{e/h}$ is the interlayer hopping amplitude for electrons/holes. If taking the hopping amplitudes as real numbers and considering the bandgap ϵ_g and the interlayer potential difference $U = (E + E_{build-in})d$, (4.3) and (4.4) can be written as:

$$H_{CB} = \begin{pmatrix} \epsilon_{VB}^{top} + \epsilon_g & t_e \\ t_e & \epsilon_{VB}^{top} + \epsilon_g + (E + E_{build-in})d \end{pmatrix} \tag{4.5}$$

and

$$H_{VB} = \begin{pmatrix} \epsilon_{VB}^{top} & t_h \\ t_h & \epsilon_{VB}^{top} + (E + E_{build-in})d \end{pmatrix} \tag{4.6}$$

We can analytically obtain the eigenvalues of the hybridized band edge energies by directly diagonalizing (4.5) and (4.6):

$$\epsilon_{CB}^{\pm} = \epsilon_{VB}^{top} + \epsilon_g + \frac{1}{2}\left[(E + E_{build-in})d \pm (4t_e^2 + (E + E_{build-in})^2 d^2)^{1/2}\right] \tag{4.7}$$

and

$$\epsilon_{VB}^{\pm} = \epsilon_{VB}^{top} + \frac{1}{2}\left[(E + E_{build-in})d \pm (4t_h^2 + (E + E_{build-in})^2 d^2)^{1/2}\right] \tag{4.8}$$

If ignoring the Coulomb binding energies and phonon energies, DX's energy can therefore be defined as the bottom conduction band edge ϵ_{CB}^{-} minus the top valence band edge ϵ_{VB}^{+}:

$$\epsilon_{DX}(E) = \epsilon_g - \frac{(4t_e^2 + (E + E_{build-in})^2 d^2)^{1/2}}{2} - \frac{(4t_h^2 + (E + E_{build-in})^2 d^2)^{1/2}}{2} \quad (4.9)$$

By comparing the interlayer hopping amplitudes t_e and t_h with the DFT calculations, we can assign the electrons and holes to certain valleys and further identify the DX species. Table 4.1 presents the fitting results of the Q-K and Q-Γ inter-bilayer DXs, which are plotted as white and red dashed curves in Fig. 4.10h, i. The built-in electric fields are 0.11 V/nm for Q-K inter-bilayer DXs and 0.049 V/nm for Q-Γ inter-bilayer DXs (converted to the dielectric environment of TMD material with $\varepsilon_{TMD} \sim 7$).

Table 4.1: Fitting parameters for DXs coupled with ferroelectricity

parameters	Q-K	Q-Γ
$E_{build-in}$	0.11 V/nm	0.049 V/nm
d	0.7 e·nm	0.9 e·nm
t_1	25 meV	50 meV
t_2	5 meV	200 meV

Finally, we are going to discuss the hysteresis behavior of the excitonic responses in this system. As shown in Figs. 4.5a, c, the cartoon shows the domain wall dynamics that is mentioned in Chapter 4.1. If we assume the exciton density is homogeneous within the laser excited area, the domain area change under an electric field contributes to the population change of the DXs that are coupled with different domains. For instance, while applying a pointing-up electric field, the XM domains that possess a pointing-up spontaneous electric polarization will reduce its electrostatic energy and expand, while the MX domains will contract their sizes. Therefore, the population of DXs (either pointing-up or pointing-down) coupled with the XM domains will be larger than those coupled with the MX domains, thus inducing a difference in the PL emission intensities.

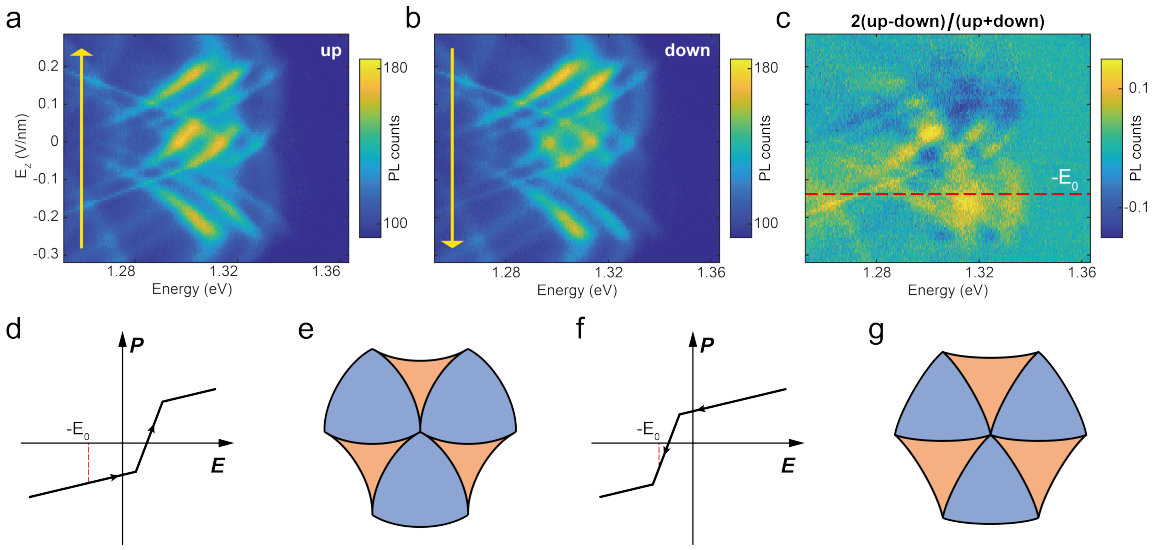

Figure 4.11: Optical signatures of hysteresis loop. a,b, Electric field dependent PL emissions in ABBA twisted double bilayer WSe_2 device D1 under an ascending (**a**) and a descending (**b**) external electric field. **c,** Difference between the ascending field dependent PL spectra (**a**) and the descending field dependent PL spectra (**b**) normalized by their average. **d,** P-E curve with an ascending electric field. **e,** Schematic of domain sizes at $-E_0$ with an ascending field. **f,** P-E curve with a descending electric field. **g,** Schematic of domain sizes at $-E_0$ with a descending field.

Figures 4.11a, b show the electric field dependence of the PL plot with opposite field-sweeping directions. We notice there is difference in the intensities of some exciton branches between the two sweeps. We can further subtract the sweeping-down plot from the sweeping-up plot and obtain a normalized differential plot (Fig. 4.11c). Even though the domain size change is not as significant as it's at the room temperature due to the domain wall stiffness at cryogenic temperature, we can still observe a significant PL intensity difference. When the external electric field is near zero, which means it's smaller than the coercivity, the size of the MX domains at a certain external electric field is larger in the sweeping-up process than in the sweeping-down process. This causes a stronger (weaker) PL emission from the DXs that are coupled with the MX (XM) domains in the sweeping-up process compared to the sweeping-down process.

To explain more specifically, let's consider a certain electric field point $-E_0$ in Fig. 4.11c, and compare the domain sizes in the ascending field case (Fig. 4.11d) and in the descending field case (Fig. 4.11f). During the ascending scan, the MX domains are slowly recovering from their maximum area. But they still have a large size (Fig. 4.11e). For the descending scan, the P-E curve just passed the critical point, where the MX and XM domains have almost the same sizes due to the interlayer friction (Fig. 4.11f). By comparing the two cases, we find that the MX domains have a larger area in the ascending scan process than in the descending scan process. Thus, DXs that are coupled with the MX domain gain a stronger emission in the ascending scan process at $-E_0$, due to the hysteresis behavior of the domain area change. Similar analysis can also be applied to the positive electric field side. The intensity difference in Fig. 4.11c is therefore explained.

4.5 SUMMARY AND APPLICATIONS

Ferroelectric thin films find their potential to multiple industrial applications. For instance, if we replace the dielectric layer in a DRAM (Fig. 1.2b) with a ferroelectric layer, we will get a ferroelectric RAM (FeRAM), where the binary-switch becomes more efficient and much faster than a DRAM, since it's no longer based on the charge and discharge of the capacitor. Instead, it only requires the flip of the spontaneous polarization. In our case, a twisted TMD thin film only needs interlayer sliding around the domain walls (Figs. 4.4d, e, f). Its reliability is also guaranteed by the ability to suffer more than 100 billion cycles of polarization flip[129], making it a reliable candidate for ferroelectric FET or RAM applications.

In 3R-stacked twisted TMD systems, the ferroelectricity emerges through domain wall dynamics, indicating a new type of ferroelectricity that is realized completely through the interlayer shear motion between two non-ferroelectric layers. Moreover, the average domain size in this system can be tuned by the twist angle, which makes moiré superlattice formation a new tuning knob for material engineering, besides doping and field. In this work, the triangular domains

with alternating spontaneous electric polarizations are directly visualized by scanning probe imaging, such as PFM and KPFM. A built-in electric field is observed during the PL characterization, which becomes one signature of the coupling between the excitonic responses in TMD and the alternating domain polarizations. In addition, it's inaccurate to obtain the built-in electric field using the potential difference from the KPFM measurements, due to the different coupling strengths for different DX species such as Q-K and Q-Γ (Fig. 4.10i) as well as the different temperatures. But it can be used as an estimation. Finally, the hysteresis loop of PL emission intensities is observed and further confirms our understanding of the interfacial ferroelectricity in 3R-stacked twisted TMD systems.

Combined with Chapter 3, we see different physics and phenomena between ABAB and ABBA-stacked TMD, which only differs by a 60° rotation. The spin-valley locked superlattice in ABAB-stacked TMD contributes to the formation of the every-other-layer DXs with large electrical tunability, while the interfacial ferroelectricity in ABBA-stacked TMD leads to the coupling between the excitons and the spontaneous polarization. This further indicates the versatility of the potential applications of TMD materials, and a new tuning knob for material engineering.

CHAPTER 5. MULTIFERROICS AND EXCITON HYBRIDIZATIONS IN TWISTED BILAYER TRANSITION METAL DICHALCOGENIDES

In this chapter, we will report the formation of dipolar excitons as well as their hybridization behaviors with the A excitons in a similar process mentioned in Chapter 3, which is further coupled with the interfacial ferroelectricity arising from the R-stacked twisted interface mentioned in the last chapter, in twisted bilayer TMD systems. Specifically, we tested WSe_2 and $MoTe_2$ due to the subtle differences in their band structure. Furthermore, we observed ferromagnetism in both twisted bilayer WSe_2 and $MoTe_2$ systems, indicating a multiferroics property, which is exciting because the pristine TMD flakes are not ferroelectric or ferromagnetic, while they appear as exotic phenomena by engineering the stacking orders.

5.1 PHYSICS IN TWISTED BILAYER TMD

Twisting two-dimensional materials with a small twist angle leads to the formation of moiré superlattice with a plethora of rich physical phenomena. Experimentalists have studied correlated insulating states and signatures of interaction-induced topologically non-trivial states in twisted bilayer WSe_2 (Ref. [122,130,131]) and twisted bilayer $MoTe_2$ (Ref. [9,17,18,132]). In moiré heterobilayers, lower energy states are found primarily in one layer because of the band alignment between two different layered materials, and they can simulate the generalized Hubbard model on triangular lattices[133]. Experimental observations of Mott insulators[134,135], generalized Wigner crystals[135-137], metal-insulator transitions[138,139], and heavy fermion behaviors[140]. Moreover, applying an out-of-plane electric field through electrostatic doping can induce band inversion, which leads to topological moiré bands[141], and topological states in AB-stacked TMD heterobilayers[142-144]. In the

special case of twisted TMD systems, a variety of exotic phenomena have also been theoretically predicted[145-152] including multiferroic[153,154].

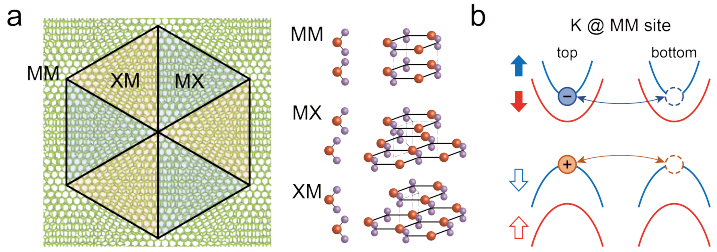

Figure 5.1: Adjacent layer hopping in R-stacked twisted bilayer TMD. a, Schematic of domain distributions and the atomic stacking orders of MM, MX and XM domains in R-stacked twisted TMD. **b,** Interlayer hopping between adjacent layers at MM sites.

Compared to ABBA-twisted double bilayer, where indirect transitions dominate the excitonic responses and only the inter-bilayer transitions can be coupled to the electric polarization, twisted bilayer TMD stacked in a parallel way (R-stacked) has a rather neat spectrum and a less complicated interactions between excitons and stacking orders. On the other hand, intriguing features such as coupled exciton hybridizations with the interfacial ferroelectricity and tunable ferromagnetism show up in the R-stacked twisted bilayer TMD without the screening from additional layers and the effective interlayer coupling that modulates the band structure and results in an indirect bandgap, which will be demonstrated later.

As mentioned in Chapter 2.3 and Chapter 3.1, pristine H-stacked bilayer TMD such as WSe_2 does not present optical Stark effect on its dR/R spectrum, due to the forbidden interlayer hopping for carriers that is further caused by the opposite spin splitting between adjacent layers at the same valley (Fig. 3.1c). However, in the MM site of the R-stacked twisted bilayer TMD, interlayer hopping between adjacent layers is allowed due to the same sign of the spin splitting[155] (Fig. 5.1b), which gives birth to interlayer intravalley dipolar exciton species, with electron and hole constituents separated in different layers. In theory, this exciton species not only has its wavefunction crossing the interface and can be coupled with the interfacial ferroelectricity, as

characterized by the built-in electric field in Chapter 4.4, but it can also hybridize with the intralayer A excitons and become brighter, as shown as the anti-crossing patterns in Chapter 3.2. Furthermore, we can simulate and reconstruct the dipolar excitons' spectra under varying electric field by diagonalizing a similar Hamiltonian matrix to (3.10), by replacing the DX term with the optical Stark effect that is coupled with the built-in electric field as in (4.2). Therefore, double anti-crossing features should be expected in the field dependence of the dipolar excitons' spectra by averaging the excitonic responses from the R-stacked MX and XM triangular domains which have opposite built-in electric field directions. Different from the simulation in Chapter 3.3, we can further obtain the interlayer hopping amplitude for electrons and holes separately if the top and bottom intralayer excitons' energy degeneracy is lifted.

Nevertheless, the periodicity of moiré superlattice is always much larger than the pristine crystal constant, depending on the twist angle and lattice match as described in (1.4). The larger periodicity will fold the original Brillouin zone, leading to a much smaller zone size[156,157] (Fig. 5.1a). Due to the moiré potential modulation, flat band can be formed at certain twist angle. For instance, in twisted bilayer graphene, the flat band appears at around 1.1° twist angle[77,157,158], while for twisted TMD, moiré flat band appears at a wide range of twist angle from 2° to 5° (Ref. [122,151]). The formation of the flat band indicates that the Hamiltonian is largely contributed by the potential term, while the kinetic energies of carriers are frozen due to a zero gradient of the Hamiltonian in the momentum space:

$$\boldsymbol{p} = \frac{m}{\hbar}\nabla_{\boldsymbol{k}} H \tag{5.1}$$

Therefore, strong correlated physics such as superconductivity[75,159,160] and ferromagnetism[9,17,18,151] can be found in these systems due to the localized carriers.

In addition, incompressible correlated states can be found at fractional filling due to the formation of Mott insulator states[134-137] or fractional Chern insulator states[9,17,151] due to the strong correlation and nontrivial topological bands[9,17,151,161-163]. These correlated states can be directly detected by quantum capacitance[164,165]. If we fabricate a device with Hall bar geometry, electrical transport measurement can be performed by monitoring the longitudinal (R_{xx}) and transverse (R_{xx})

Hall resistances[45] at varying parameters including external magnetic field, electrostatic doping density and out-of-plane electric field. Correlated states will appear as insulating peaks due to their incompressible gap[17]. Alternatively, a simpler but more indirect option to probe the correlated states is optical characterization. In PL and dR/R measurements, due to the reduction of material's dielectric constant/screening at insulating states, neutral or charged exciton states experience sudden blueshift of their energies[9,136,166], especially for exciton species with larger Bohr radii such as the Rydberg exciton states[136]. For bands with a nontrivial Chern number, the gapped states will disperse with the magnetic field following the Streda formula $C = \Phi_0 \partial n / \partial B$ (Ref. [9,17]). Plus, reflective magnetic circular dichroism (RMCD) and other magneto-optic effects, such as magneto-optic Kerr effect (MOKE) can be applied to examine materials' magnetism, using coupling between local magnetization and light chirality. If twisted TMD exhibits ferromagnetism from the strong exchange interaction among correlated electrons/holes, hysteresis loop of circular dichroism or Kerr rotation versus external magnetic field will be visualized. We will talk about the magneto-optic effect in Chapter 5.4 in detail.

5.2 EXCITONIC RESPONSES IN TWISTED BILAYER TMD

R-stacked twisted bilayer TMD devices (Fig. 5.2a) are fabricated employing transfer, tear-and-stack, lithography and PVD techniques, with the contact cleaning technique mentioned in Chapter 1.3.3. Specifically, we use WSe_2 and $MoTe_2$ for testing due to their subtle differences in their band structure. For instance, Mo-based TMD has an opposite spin splitting at the conduction band compared to W-based TMD, leading to a bright exciton ground state in Mo-based TMD systems, while in W-based TMD the ground state is the dark neutral excitons[22]. Furthermore, unlike ordinary TMD bilayers that have indirect bandgaps with their valence band maxima at the Q valley, bilayer $MoTe_2$ is special due to the maintenance of its direct bandgap at the K valley[167], resulting in a more effective K-K exciton emission.

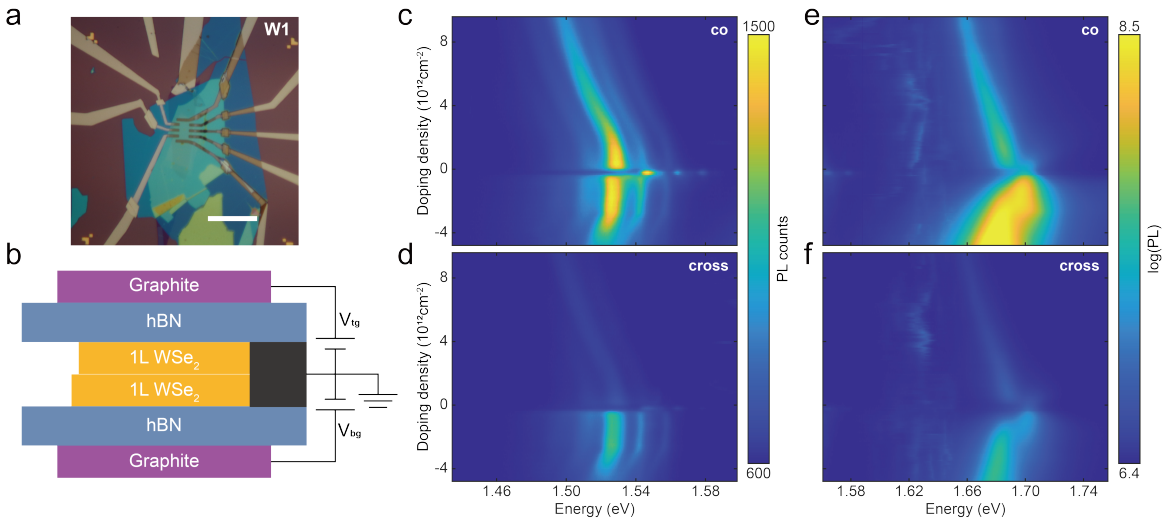

Figure 5.2: Intravalley and intervalley PL spectra of R-stacked twisted bilayer WSe_2 device W1. a, Optical microscope image of device W1. Scale bar, 20 μm. **b,** Schematic of the side view of device W1. **c,d,** Doping density dependence of the intervalley PL emissions with co-circular (**c**) and cross-circular (**d**) polarizations. **e,f,** Doping density dependence of the intravalley PL emissions with co-circular (**e**) and cross-circular (**f**) polarizations.

For R-stacked twisted bilayer WSe_2 devices W1 and W2, the top and bottom layers are parallelly stacked and marginally twisted with a twist angle around 2.6°, while for R-stacked twisted bilayer $MoTe_2$ devices, the twist angle is around 4.5°, both for the formation of flat bands and correlated carriers. Top and bottom graphite layers serve as the gates and hBN layers become the dielectric due to its sizable bandgap ~ 5.9 eV. The electrostatic gating causes independent control of doping density and out-of-plane electric field following (1.3).

For R-stacked twisted bilayer WSe_2 devices, the optical setups for PL and dR/R measurement can be found in Chapter 1.3.4 (Figs. 1.8a, b). Far field in-plane emission from interlayer excitons that have out-of-plane optical dipoles can be captured thanks to our high-NA objective lens (LUCPLFLN40X). Figures 5.2c, d, e, f present the doping density dependence of the PL spectra (from 1.45 eV to 1.75 eV) of device W1 with right circular polarized (σ^+) laser excitation. The co-polarized PL (Figs. 5.2c, e) collects only the reflected PL component with the same light chirality (σ^+) as the incident light, while the cross-polarized PL (Figs. 5.2d, f) collects

the opposite chirality (σ^-). First, we notice that the PL spectrum can be divided into the intravalley and intervalley parts with the same emission energy as the pristine H-stacked WSe_2 bilayer in Chapter 2.3. Although in this system, the intravalley K-K transitions have interlayer component due to the active interlayer carrier hopping, which can also be confirmed by examining the optical Stark effect under varying out-of-plane electric fields (Fig. D.1). Similar to pristine bilayers, charged trion states appear at both electron- and hole-doping side due to excitons bound to extra carriers. Secondly, it's expected that optical selection rule exists in the intravalley K-K transitions due to the coupling between K/K' valleys and excitation chirality[24-26]. However, the electron-doping side of the intervalley transitions also exhibits strong optical selection rule, whose origin is yet to be confirmed but is of great interests.

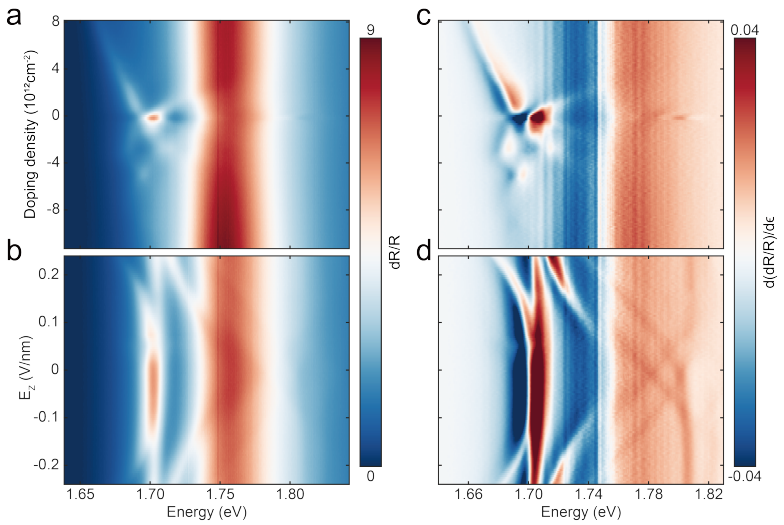

Figure 5.3: dR/R spectra of R-stacked twisted bilayer WSe_2 device W1. a,b, Doping density dependence (**a**) and out-of-plane electric field dependence (**b**) of the dR/R resonances from device W1. **c,d,** Doping density dependence (**c**) and out-of-plane electric field dependence (**d**) of the dR/R spectra differentiated with respective to photon energy.

Figure 5.3a shows the doping dependence of the dR/R spectrum of W1, where only the intravalley direct and bright transitions can be seen. We can further take the derivative of the dR/R spectra over the X-axis to resolve subtle spectral features (Fig. 5.3c). Like the pristine bilayers in

Chapter 2.3, trion states and Rydberg 2S states can be seen. However, energy blueshift happens around 5.0×10^{12} cm^{-2} hole doping density, which exactly corresponds to the full filling state of this system, where two degenerated holes with opposite spins reside in each moiré unit cell, if calculated following (1.4) with a twisted angle equal to 2.6°. In addition, extra peak appears at 2.8×10^{12} cm^{-2} hole doping density, corresponding to the half filling state with one hole per moiré unit cell. I will discuss these states and their magnetic characterization in detail in Chapter 5.4.

On the other hand, the out-of-plane electric field dependence of the dR/R spectra also shows intriguing features, especially after taking the derivative, as shown in Figs. 5.3b, d. Like the every-other-layer dipolar excitons in Chapter 3.2, optical Stark effect happens to the dipolar exciton states with opposite electric dipole orientations, with several avoided-crossing features as the dipolar exciton is tuned across the resonances of the intralayer excitons as well as their Rydberg 2S states[96]. Likewise, this indicates exciton hybridizations between the two exciton species, which we can describe quantitatively in Chapter 5.3. The originally dark dipolar excitons gain optical dipoles through hybridization with the intralayer species and become visible in the dR/R spectra. In this case, the electric dipoles can be determined to be $d = \frac{\varepsilon_{TMD}}{\varepsilon_{hBN}} \frac{\Delta Energy}{\Delta Ez} \sim 0.70$ e·nm, indicating a 0.70 nm layer separation between the electrons and the holes constituents, which is exactly the distance between the top and bottom WSe_2 layers.

However, what makes the exciton hybridizations in R-stacked twisted bilayer WSe_2 special is the involvement of the interfacial ferroelectricity emerged from the R-stacked interface. Surprisingly, two sets of crossing features appear in the spectra. We can understand the two crossings by the built-in electric fields due to the excitonic coupling with the interfacial ferroelectricity, as discussed in Chapter 4.4. In this case, the dipolar excitons find their energies at 1.788 eV, with the 1S states of the A excitons at 1.702 eV and the 2S states at 1.804 eV. The Coulomb binding energy of the dipolar excitons in R-stacked twisted bilayer WSe_2 turns out to be around 20 meV smaller than the every-other-layer dipolar excitons in trilayer WSe_2. Furthermore, the built-in electric field that the dipolar excitons feel is around 0.022 V/nm (converted to the dielectric environment of TMD material with $\varepsilon_{TMD} \sim 7$). Unlike the ABBA-twisted double bilayer WSe_2's PL in Chapter 4.4, however, we fail to observe hysteresis loop of the reflectance intensity

versus the external electric field sweeping back and forth at different directions (Fig. D.2). The reason could be a small moiré periodicity due to a large twist angle (only 7.3 nm at 2.6° twist angle), which stiffens the domain wall dynamic, especially at a cryogenic temperature. Plus, compared to ABBA-twisted WSe_2's PL, the dipolar excitons' emission is weak in the dR/R spectra since it acquires optical dipole through exciton hybridizations with bright excitons. The coupling between exciton hybridizations and interfacial ferroelectricity will be considered in Chapter 5.3 for quantitative reconstructions.

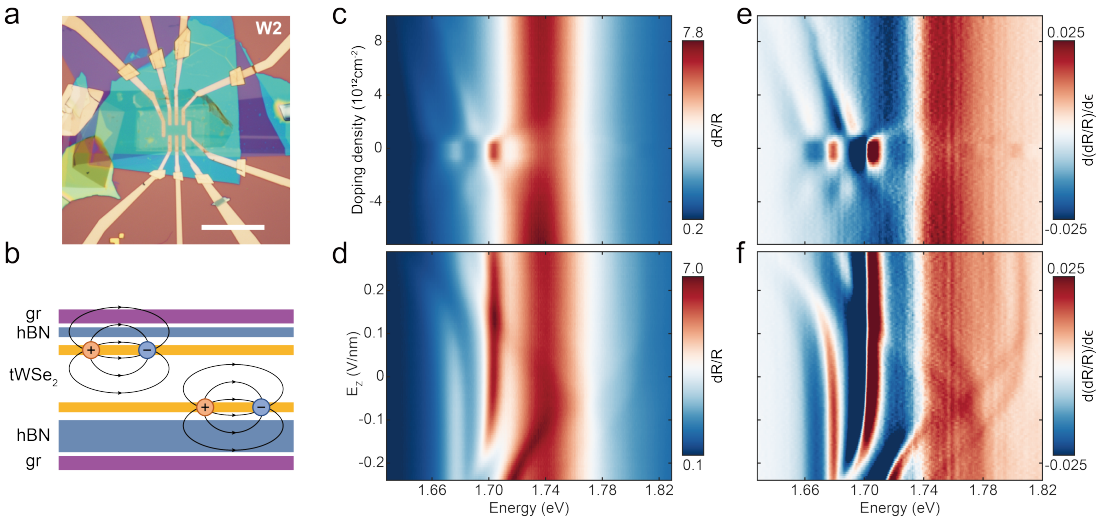

Figure 5.4: dR/R spectra of R-stacked twisted bilayer WSe_2 device W2. a, Optical microscope image of device W2. Scale bar, 20 μm. **b,** Schematic of the asymmetric dielectric screening from the asymmetric hBN encapsulation. **c,d,** Doping density dependence (**c**) and out-of-plane electric field dependence (**f**) of the dR/R resonances from device W2. **e,f,** Doping density dependence (**e**) and out-of-plane electric field dependence (**f**) of the dR/R spectra differentiated with respective to photon energy.

In the previous chapters, we find that K-K direct dipolar excitons are missing in the ABBA-twisted WSe_2's dR/R spectra while sweeping the out-of-plane electric field (Fig. 3.8c). In theory, interlayer excitons with electrons and holes separated into the two adjacent layers from the B-B interface in ABBA system are momentum-allowed and exist in the same spectral range. These

exciton species are not visible in dR/R spectra possibly because of the weak optical dipole. Even though the interlayer exciton's optical dipole is extremely weak by itself, it can become visible in absorption measurement via the hybridization with an adjacent bright intralayer exciton through electron or hole interlayer hopping. For ABBA WSe2 with a small twist angle, at the B-B interface upon lattice reconstruction, Rhombohedral MX and XM domains form. In the high symmetry MX and XM stacking, interlayer electron and hole hopping are both forbidden at the K points because of the distinct eigenvalues of the Bloch states in the two layers under the C3 rotation[155]. Therefore, the concerned interlayer exciton at B-B interface cannot hybridize with an intralayer exciton and remain invisible in absorption.

In Chapter 3, the hopping amplitude of electrons and holes cannot be determined separately from the electric field dependence data due to the energy degeneracy of the intralayer A excitons. The simulations and reconstructions will give similar results if only one carrier (electron or hole) dominates the every-other-layer hopping (Fig. C.2). Likewise, we cannot determine in device W1 whether it's the electrons or the holes that are dominating the interlayer hopping. However, the second R-stacked twisted bilayer WSe_2 device W2 changes the situation. In W2, the energy degeneracy between the top and bottom intralayer excitons, or intralayer bandgaps, is lifted, as shown in the doping density dependence of the dR/R spectra in device W2 (Figs. 5.4c, e). With one 1S A exciton at 1.677 eV and the other at 1.704 eV, the energy difference is as large as 27 meV. The same energy difference goes for the 2S states, with one 2S state at 1.777 eV and the other at 1.804 eV. We attribute the 27 meV energy difference to the inhomogeneous strain induced during device fabrication. For instance, during the PC stamp dry transfer process, the stamp surface is curved especially when it's in contact with the silicon chips. The TMD flakes sitting on top of the stamp therefore gain a hetero-strain between the top and bottom TMD layers. In addition, another major contribution comes from the asymmetric dielectric screening. Compared to device W1, the top hBN dielectric layer (11.5 nm) in W2 is much thinner than the bottom hBN layer (26.3 nm). The thinner top hBN dielectric layer introduces a stronger dielectric screening from the conductive graphite gate layer to the intralayer excitons at the top layer WSe_2 (Fig. 5.4b), resulting in a smaller quasiparticle bandgap and therefore a lower emission energy compared to the

intralayer excitons at the bottom layer[22,99,100] (Although at this time we still do not know which emission peak corresponds to which layer).

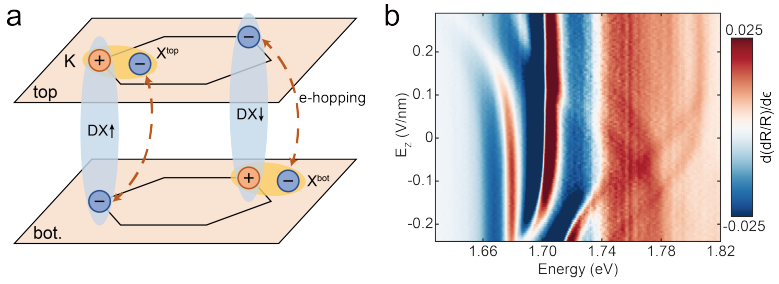

Figure 5.5: Asymmetric carrier hopping in R-stacked twisted bilayer WSe_2. a, Coupling between DX (light blue) and intralayer (orange) excitons in bilayer geometry through an electron-only hopping process. **b,** Out-of-plane electric field dependence of the dR/R spectra differentiated with respective to photon energy.

Figures 5.4d, f and Figure 5.5 demonstrate the electric field dependence of the dR/R spectra in device W2, together with the differentiated plot. The hybridization behavior between the dipolar excitons and the intralayer 1S and 2S states are clear but surprising. The dipolar excitons with pointing up electric dipoles only hybridize with the lower-energy branches of the intralayer 1S and 2S states with the formations of avoided-crossings, but they cross the higher-energy branches directly (Fig. 5.5b). On the contrary, the pointing-down dipolar excitons only hybridize with the higher-energy branches of the intralayer excitons and realize avoided-crossings. This means that only one type of carriers, either electron or hole, is hopping between the top and bottom WSe_2 layers (Fig. 5.5a). If it's electron (hole), the pointing-up dipolar excitons only hybridize with the intralayer excitons residing in the top (bottom) layer. Therefore, as long as we figure out the correspondence between the lower-/higher-energy branches and the intralayer excitons residing in the top/bottom layers, we will know the carrier hopping behaviors in this system. For the rest of this section, I'm going to present how to identify the top and bottom layers' emissions and

therefore capture the type of carriers (electron or hole) that is dominating the interlayer hopping in R-stacked twisted bilayer WSe_2 systems.

To resolve the top and bottom layers' intralayer excitons, we can investigate the layer pseudospin[168], or layer polarization, under an external electric field. For instance, while applying a pointing-up electric field, free electrons will feel a pointing-down electrostatic force and be polarized to the bottom layer, and free holes will be polarized to the top layer. Therefore, if we dope the R-stacked twisted bilayer WSe_2 at a biased layer polarization, the trion formations might be different between the top and bottom layers' intralayer species. To do this, we need to scan the doping density while fixing the system's out-of-plane electric field at a finite value, which can be realized following (1.3) thanks to the independent control from the dual-gated device structure.

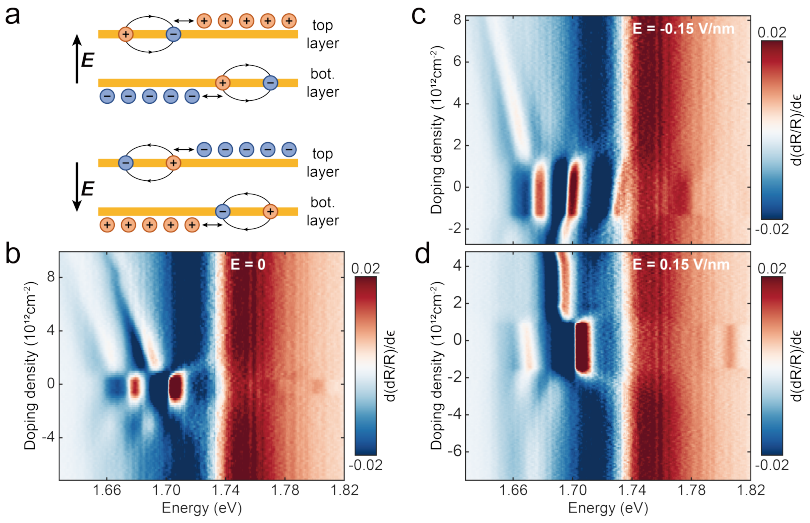

Figure 5.6: Layer polarization analysis. a, Schematic of intralayer trion configurations at a finite interlayer electrostatic potential bias. **b,c,d,** Doping density dependence of the differentiated dR/R resonances at fixed out-of-plane electric fields equal to 0 (**b**), -0.15 V/nm (**c**) and 0.15 V/nm (**d**).

Figures 5.6 c, d demonstrate the differentiated doping density dependence of the dR/R spectra at ±0.15 V/nm out-of-plane electric field (in the dielectric environment of hBN layer with

$\varepsilon_{hBN} \sim 3.1$), together with the zero-field doping dependence result for comparison. The doping density dependent plots at more electric field values are shown in Fig. D.3. At -0.15 V/nm electric field, we observe that only the lower-energy branch of the intralayer 1S state can form negatively charged trion at the electron-doping side, while only the higher-energy branch forms positively charged trion at the hole-doping side shown as the redshifted tail connected to the neutral exciton. And the situation becomes the opposite at +0.15 V/nm electric field. When the WSe_2 bilayer is electrostatically doped with electrons, the extra electrons are polarized to the top (bottom) layer at a pointing-down (pointing-up) electric field. Consequently, only the intralayer excitons in the top (bottom) layer can form intralayer negative trion states with the accumulated electrons from the same layer (Fig. 5.6a), which are also optically bright[66]. For the bottom (top) layer's excitons, forming interlayer negative trion states is possible but optically dark. The trion states are thus missing from the doping dependence of the dR/R spectra. Furthermore, a third peak appears around 1.73 eV at charge neutrality with -0.15 V/nm field bias. After comparing with the electric field dependent plot, we attribute this neutral state to the dipolar exciton with a pointing-down electric dipole and coupled with a pointing-up domain electric polarization (negative built-in electric field) from the interfacial ferroelectricity.

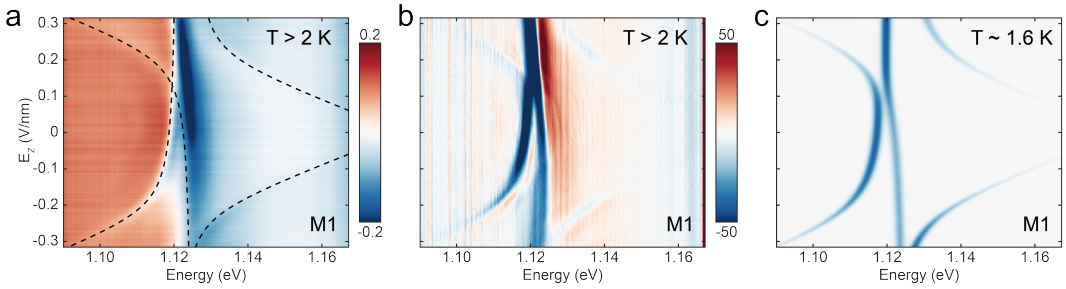

Figure 5.7: Asymmetric carrier hopping in R-stacked twisted bilayer $MoTe_2$. a,b, Out-of-plane electric field dependences of the dR/R resonances (**a**) and the differentiated dR/R (**b**) in a twisted $MoTe_2$ device at T > 2 K. The black dashed curves represent the curve fitting results. **c,** Reconstructed field dependent dR/R spectra at a dilution temperature T ~ 1.6 K.

After layer polarization and trion formation analysis, we identify the lower-energy branch as the intralayer A excitons from the top isolated WSe_2 layer, while the higher-energy branch belongs to the bottom layer. Therefore, conclusion can be reached that only electrons dominate the interlayer hopping and thus exciton hybridizations in R-stacked twisted bilayer WSe_2 system. For the intralayer excitons in the top layer, interlayer electron hopping should enable their hybridization with the dipolar excitons with pointing-up dipoles, while the forbidden interlayer hole hopping prevents them from hybridizing with the pointing-down dipolar excitons. To repeat, we also find asymmetric carrier hopping between adjacent layers in other R-stacked twisted TMD bilayer systems such as twisted $MoTe_2$ (Fig. 5.7).

As mentioned in Chapter 3.1, in pristine H-stacked bilayer WSe_2, the interlayer electron hopping amplitude vanishes due to the three-fold rotational symmetry, while the hole hopping has a finite amplitude[73], which is different from our case, where the bilayer is R-stacked. Different lattice symmetry and structure might change the hopping amplitude and the selection rule[169]. Possible root cause could be the different wavefunction diffusion over the moiré supercell of the electron and hole constituents that form the dipolar excitons. As I just mentioned above, interlayer hopping through the high symmetry MX and XM sites is forbidden in R-stacked twisted TMD bilayer[155]. We can address this question by calculating the single particle wavefunction distribution over the real space of the moiré supercell[170-172]. If the wavefunction of one carrier (electron or hole) diffuses large enough to the boundary of the moiré supercell[166], this carrier can then hop between adjacent layers through the MM site (the domain walls), to enable the interlayer hopping. The asymmetric wavefunctions between the electron and hole constituents finally lead to the asymmetric carrier hopping process. This topic is of great interests and worth further investigation.

5.3 EXCITON HYBRIDIZATIONS COUPLED WITH INTERFACIAL FERROELECTRICITY

Similar to the calculation in Chapter 3.3, we can simulate and reconstruct the hybridizations. Instead, the dipolar excitons are coupled with the interfacial ferroelectricity, resulting in the addition of built-in electric fields.

In R-stacked twisted bilayer WSe_2, the relevant excitonic basis states for the observed hybridization are: $|1S^{top}\rangle$, $|1S^{bot}\rangle$, $|2S^{top}\rangle$, $|2S^{bot}\rangle$, $|DX_{\uparrow}\rangle$, $|DX_{\downarrow}\rangle$, denoting respectively the 1S and 2S orbital intralayer excitons in top and bottom layer, and dipolar excitons with electrical dipole pointing up and down. Adopting (3.10), we add the built-in electric field term to the external electric field as an extra parameter. Energy degeneracies are lifted for dipolar excitons residing in the MX and XM domains, as $|DX_{\uparrow\downarrow}^{MX}\rangle$ and $|DX_{\uparrow\downarrow}^{XM}\rangle$, respectively. The diagonal part of the Hamiltonian of the excitons residing in the MX domains can be written as:

$$H_0^{MX} = \begin{pmatrix} \varepsilon_{1S}^{top} & 0 & 0 & 0 & 0 & 0 \\ 0 & \varepsilon_{1S}^{bot} & 0 & 0 & 0 & 0 \\ 0 & 0 & \varepsilon_{DX}^{u} - (E_Z + E_i)\cdot d & 0 & 0 & 0 \\ 0 & 0 & 0 & \varepsilon_{DX}^{d} + (E_Z + E_i)\cdot d & 0 & 0 \\ 0 & 0 & 0 & 0 & \varepsilon_{2S}^{top} & 0 \\ 0 & 0 & 0 & 0 & 0 & \varepsilon_{2S}^{bot} \end{pmatrix} \tag{5.2}$$

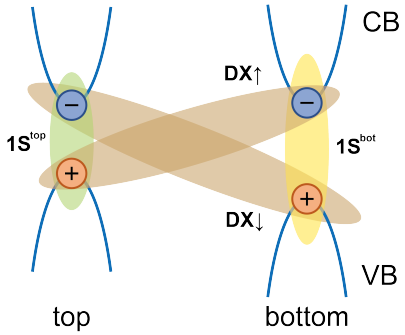

Figure 5.8: Schematic of energy bands and exciton structures in device W2.

where $\pm(E_Z + E_i) \cdot d$ corresponds to the Stark shifts of $|\mathrm{DX}_{\downarrow\uparrow}\rangle$ away from their zero-field energy $\varepsilon_{\mathrm{DX}}^{\mathrm{u/d}}$. The difference between $\varepsilon_{\mathrm{DX}}^{\mathrm{u}}$ and $\varepsilon_{\mathrm{DX}}^{\mathrm{d}}$ in device W2 originates from the band modulation from the inhomogeneous strain, as depicted in Fig. 5.8. In device W1, $\varepsilon_{\mathrm{DX}}^{\mathrm{u}}$ and $\varepsilon_{\mathrm{DX}}^{\mathrm{d}}$ have the same value and are degenerated at $E_z = -E_i$. Similarly, the diagonal part of the Hamiltonian of the excitons residing in the XM domains can be described as:

$$H_0^{\mathrm{XM}} = \begin{pmatrix} \varepsilon_{1\mathrm{S}}^{\mathrm{top}} & 0 & 0 & 0 & 0 & 0 \\ 0 & \varepsilon_{1\mathrm{S}}^{\mathrm{bot}} & 0 & 0 & 0 & 0 \\ 0 & 0 & \varepsilon_{\mathrm{DX}}^{\mathrm{u}} - (E_Z - E_i) \cdot d & 0 & 0 & 0 \\ 0 & 0 & 0 & \varepsilon_{\mathrm{DX}}^{\mathrm{d}} + (E_Z - E_i) \cdot d & 0 & 0 \\ 0 & 0 & 0 & 0 & \varepsilon_{2\mathrm{S}}^{\mathrm{top}} & 0 \\ 0 & 0 & 0 & 0 & 0 & \varepsilon_{2\mathrm{S}}^{\mathrm{bot}} \end{pmatrix} \tag{5.3}$$

where only the sign of the built-in electric field is switched due to the opposite domain polarizations from the XM domains. Interlayer hopping of electron/hole leads to an off-diagonal coupling H_1 between $\mathrm{DX}_{\downarrow\uparrow}$ and intralayer states (both 1S and 2S):

$$H_1 = \begin{pmatrix} 0 & 0 & t_e^{(1)} & t_h^{(1)} & 0 & 0 \\ 0 & 0 & t_h^{(1)} & t_e^{(1)} & 0 & 0 \\ \overline{t_e^{(1)}} & \overline{t_h^{(1)}} & 0 & 0 & \overline{t_e^{(2)}} & \overline{t_h^{(2)}} \\ \overline{t_h^{(1)}} & \overline{t_e^{(1)}} & 0 & 0 & \overline{t_h^{(2)}} & \overline{t_e^{(2)}} \\ 0 & 0 & t_e^{(2)} & t_h^{(2)} & 0 & 0 \\ 0 & 0 & t_h^{(2)} & t_e^{(2)} & 0 & 0 \end{pmatrix} \tag{5.4}$$

where $t_e^{(1)}$ ($t_e^{(2)}$) stands for the coupling strength between $\mathrm{DX}_{\downarrow\uparrow}$ and intralayer 1S (2S) state that originates from the interlayer electron hopping, while $t_h^{(1)}$ ($t_h^{(2)}$) originates from the interlayer electron hopping. The overlines stands for the conjugations of the coupling strengths for Hermitian purpose.

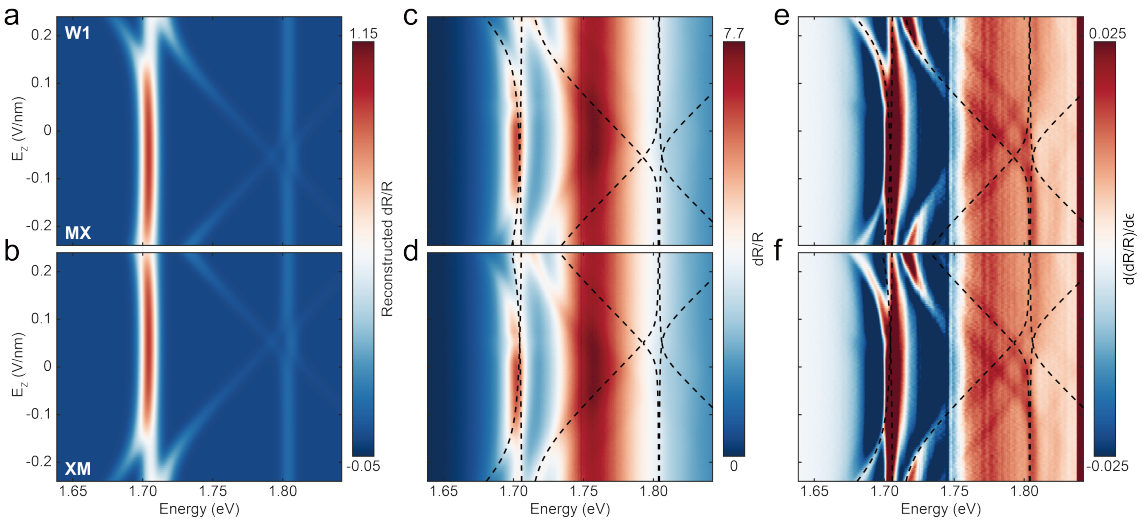

Figure 5.9: Modeling and reconstructing the exciton hybridizations coupled with one domain in device W1. a,b, Reconstructed field dependent dR/R spectra from MX (**a**) and XM (b) domains. **c,d,** Simulated field dependent dR/R spectra from MX (**c**) and XM (**d**) domains. **e,f,** Simulated field dependent dR/R spectra that are differentiated with respect to photon energy from MX (**e**) and XM (**f**) domains.

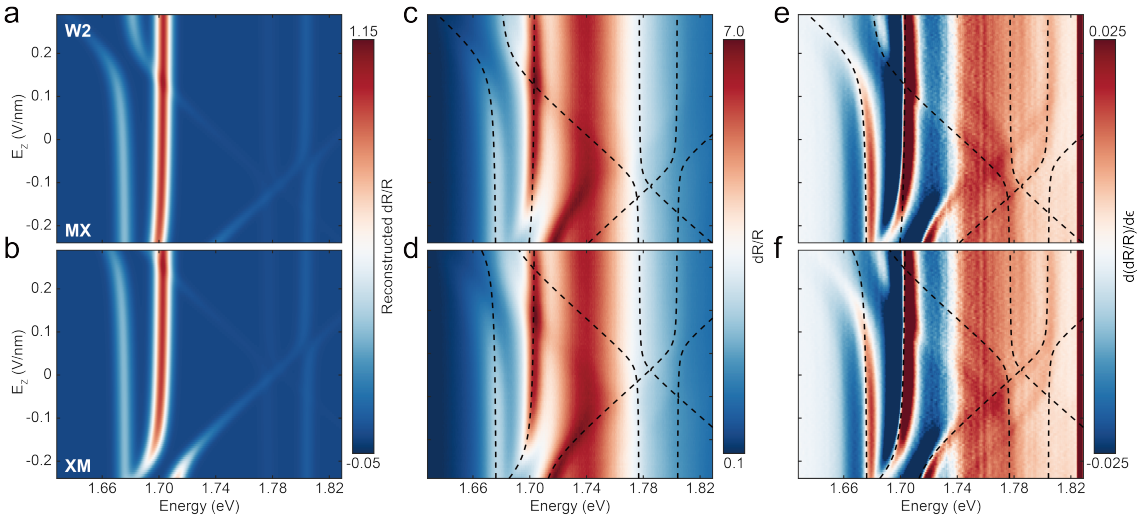

Figure 5.10: Modeling and reconstructing the exciton hybridizations coupled with one domain in device W2. a,b, Reconstructed field dependent dR/R spectra from MX (**a**) and XM (b) domains. **c,d,** Simulated field dependent dR/R spectra from MX (**c**) and XM (**d**) domains. **e,f,** Simulated field dependent dR/R spectra that are differentiated with respect to photon energy from MX (**e**) and XM (**f**) domains.

After diagonalization of $H^{\mathrm{MX}} = H_0^{\mathrm{MX}} + H_1$ by $H_D^{\mathrm{MX}} = U^{\mathrm{MX}\,\dagger} H^{\mathrm{MX}} U^{\mathrm{MX}}$ for excitons in the MX domains, we obtain six eigenstates ($|\mathrm{X}_1^{\mathrm{XM}}\rangle$, $|\mathrm{X}_2^{\mathrm{MX}}\rangle$, $|\mathrm{X}_3^{\mathrm{MX}}\rangle$, $|\mathrm{X}_4^{\mathrm{MX}}\rangle$,$|\mathrm{X}_5^{\mathrm{MX}}\rangle$, $|\mathrm{X}_6^{\mathrm{MX}}\rangle$),

$$\begin{pmatrix} |\mathrm{X}_1^{\mathrm{MX}}\rangle \\ |\mathrm{X}_2^{\mathrm{MX}}\rangle \\ |\mathrm{X}_3^{\mathrm{MX}}\rangle \\ |\mathrm{X}_4^{\mathrm{MX}}\rangle \\ |\mathrm{X}_5^{\mathrm{MX}}\rangle \\ |\mathrm{X}_6^{\mathrm{MX}}\rangle \end{pmatrix} = U^{MX\,\dagger} \begin{pmatrix} |1\mathrm{S}^{\mathrm{top}}\rangle \\ |1\mathrm{S}^{\mathrm{bot}}\rangle \\ |\mathrm{DX}_{\uparrow}^{\mathrm{MX}}\rangle \\ |\mathrm{DX}_{\downarrow}^{\mathrm{MX}}\rangle \\ |2\mathrm{S}^{\mathrm{top}}\rangle \\ |2\mathrm{S}^{\mathrm{bot}}\rangle \end{pmatrix} \tag{5.5}$$

and eigenenergies $H_D^{\mathrm{MX}} = diag(\varepsilon_1^{\mathrm{MX}}(E_z), \varepsilon_2^{\mathrm{MX}}(E_z), \varepsilon_3^{\mathrm{MX}}(E_z), \varepsilon_4^{\mathrm{MX}}(E_z), \varepsilon_5^{\mathrm{MX}}(E_z), \varepsilon_6^{\mathrm{MX}}(E_z))$, as function of electric field. These mixed eigenstates are close to the base vectors, except around $\varepsilon_{\mathrm{DX}\uparrow\downarrow}^{\mathrm{MX}} \approx \varepsilon_{1\mathrm{S}/2\mathrm{S}}$ regions, where $\mathrm{DX}_{\downarrow\uparrow}^{MX}$ hybridize with intralayer 1S/2S and anti-crossing features appear. By fitting the resonance features in the measured dR/R data (Fig. 5.9c and Fig. 5.10c), we obtain the fitting parameters as in Table 5.1.

Table 5.1: Fitting parameters for exciton hybridizations coupled with MX domain

parameters	device W1	device W2
$\varepsilon_{1\mathrm{S}}^{\mathrm{top}}$	1.707 eV	1.677 eV
$\varepsilon_{1\mathrm{S}}^{\mathrm{bot}}$	1.707 eV	1.704 eV
$\varepsilon_{\mathrm{DX}}^{\mathrm{u}}$	1.792 eV	1.763 eV
$\varepsilon_{\mathrm{DX}}^{\mathrm{d}}$	1.792 eV	1.801 eV
$\varepsilon_{2\mathrm{S}}^{\mathrm{top}}$	1.804 eV	1.777 eV
$\varepsilon_{2\mathrm{S}}^{\mathrm{bot}}$	1.804 eV	1.804 eV
d	0.80 nm	0.80 nm
E_i	0.055 V/nm	0.060 V/nm
$t_{\mathrm{e}}^{(1)}$	15 meV	13 meV
$t_{\mathrm{e}}^{(2)}$	5 meV	5 meV
$t_h^{(1)}$	0	0
$t_h^{(2)}$	0	0

From Table 5.1 and the simulated results for both device W1 (Fig. 5.9c) and W2(Fig. 5.10c), we first find that the energy differences between states are constant, confirming our labeling of each excitonic peak. For instance, the intralayer 1S and 2S states are separated by around 0.1 eV for both top and bottom layers from both devices. Considering the optical Stark effect of the dipolar excitons in both devices, their electric dipole moments, or layer separations, are constantly equal to 0.70 nm, the exact distance between the top and bottom layers of WSe_2 bilayers, verifying our understanding of the structure of $DX_{\downarrow\uparrow}$ states.

Similarly, the exciton hybridizations coupled with interfacial ferroelectricity in the XM domains can be simulated by diagonalizing the XM's Hamiltonian $H^{\mathrm{XM}} = H_0^{\mathrm{XM}} + H_1$, and obtain:

$$\begin{pmatrix} |\mathrm{X}_1^{\mathrm{XM}}\rangle \\ |\mathrm{X}_2^{\mathrm{XM}}\rangle \\ |\mathrm{X}_3^{\mathrm{XM}}\rangle \\ |\mathrm{X}_4^{\mathrm{XM}}\rangle \\ |\mathrm{X}_5^{\mathrm{XM}}\rangle \\ |\mathrm{X}_6^{\mathrm{XM}}\rangle \end{pmatrix} = U^{MX\,\dagger} \begin{pmatrix} |1\mathrm{S}^{\mathrm{top}}\rangle \\ |1\mathrm{S}^{\mathrm{bot}}\rangle \\ |\mathrm{DX}_{\uparrow}^{\mathrm{XM}}\rangle \\ |\mathrm{DX}_{\downarrow}^{\mathrm{XM}}\rangle \\ |2\mathrm{S}^{\mathrm{top}}\rangle \\ |2\mathrm{S}^{\mathrm{bot}}\rangle \end{pmatrix} \tag{5.6}$$

with eigenenergies $H_D^{\mathrm{XM}} = diag(\varepsilon_1^{\mathrm{XM}}(E_z), \varepsilon_2^{\mathrm{XM}}(E_z), \varepsilon_3^{\mathrm{XM}}(E_z), \varepsilon_4^{\mathrm{XM}}(E_z), \varepsilon_5^{\mathrm{XM}}(E_z), \varepsilon_6^{\mathrm{XM}}(E_z))$. The fitting results are shown in Fig. 5.9d and Fig. 5.10d with the fitting parameters in Table 5.2.

Table 5.2: Fitting parameters for exciton hybridizations coupled with XM domain

parameters	device W1	device W2
$\varepsilon_{1\mathrm{S}}^{\mathrm{top}}$	1.707 eV	1.677 eV
$\varepsilon_{1\mathrm{S}}^{\mathrm{bot}}$	1.707 eV	1.704 eV
$\varepsilon_{\mathrm{DX}}^{\mathrm{u}}$	1.792 eV	1.763 eV
$\varepsilon_{\mathrm{DX}}^{\mathrm{d}}$	1.792 eV	1.801 eV
$\varepsilon_{2\mathrm{S}}^{\mathrm{top}}$	1.804 eV	1.777 eV
$\varepsilon_{2\mathrm{S}}^{\mathrm{bot}}$	1.804 eV	1.804 eV

d	0.80 nm	0.80 nm
E_i	0.050 V/nm	0.060 V/nm
$t_{\mathrm{e}}^{(1)}$	15 meV	13 meV
$t_{\mathrm{e}}^{(2)}$	5 meV	5 meV
$t_h^{(1)}$	0	0
$t_h^{(2)}$	0	0

We find the results are mostly the same as Table 5.1, indicating the consistent physics for MX and XM domains, except for the opposite domain polarizations from the opposite lateral displacement that breaks the mirror symmetry. Examining the coupling with interfacial ferroelectricity, we find that the built-in electric field are similar in both cases: 0.05 V/nm for device W1 and 0.06 V/nm for device W2 (converted to the dielectric environment of hBN material with $\varepsilon_{hBN} \sim 3.1$). They are also close to other twisted bilayer TMD systems (e.g., 0.09 V/nm for twisted bilayer $MoSe_2$ (Ref. [69])). This verifies our interpretation of the excitonic coupling with the interfacial ferroelectricity (Chapter 4.4) as well as its origin in R-stacked TMD elaborated in Chapter 4.1.

The exciton coupling strengths align with our interpretations in Chapter 5.2. We find that the hole hopping related coupling strengths $t_h^{(1)}$ and $t_h^{(2)}$ must vanish for a direct crossing between the $\left|\mathrm{DX}_{\uparrow}^{\mathrm{XM}}\right\rangle$ and the $\left|1\mathrm{S}^{\mathrm{bot}}\right\rangle$ states, as an example. On the other hand, the electron hopping related coupling strengths, $t_e^{(1)} = 17$ meV and $t_e^{(2)} = 7$ meV, are slightly larger than the coupling strengths in the every-other-layer dipolar exciton's case ($t_1 \approx t_2 \approx 5.5$ meV), where both electrons and holes are assumed to hop in an every-other-layer configuration. The larger hopping strengths might be contributed by a stronger hopping amplitude between adjacent layers and the vanishing hole hopping in this system. Overall, our results demonstrate the delicate coupling between exciton hybridizations and moiré-induced interfacial ferroelectricity.

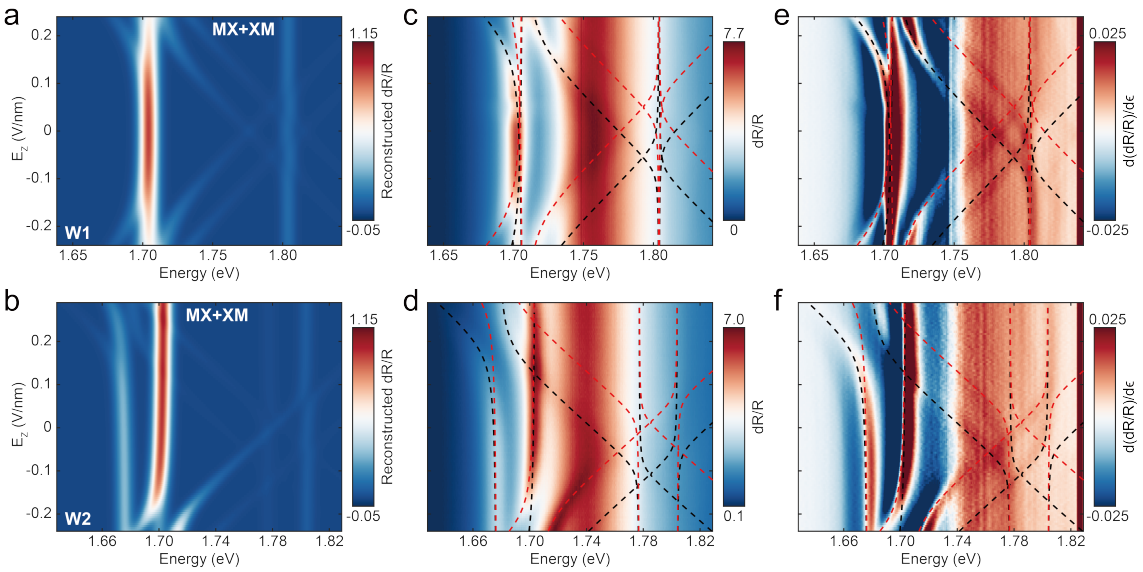

Figure 5.11: Modeling and reconstructing the exciton hybridizations averaged over both domains in W1 and W2. a,b, Reconstructed field dependent dR/R spectra that are averaged over MX and XM domains in W1 (**a**) and W2 (**b**). **c,d,** Simulated field dependent dR/R spectra that are averaged over MX and XM domains in W1 (**c**) and W2 (**d**). Black and red dashed curves represent the fitting results from MX and XM domains, respectively. **e,f,** Simulated field dependent dR/R spectra that are differentiated and averaged over MX and XM domains in W1 (**e**) and W2 (**f**).

We further model the spectral density of each excitonic state as a Gaussian distribution with a bandwidth w_i and intensity I_i ($i = 1S^{top/bot}$, $DX_{\downarrow/\uparrow}$, $2S^{top/bot}$). For both MX and XM cases, the optical reflectance spectrum as a function of incidence energy ε and electric field E_z is given by:

$$I^{MX/XM}(\varepsilon,\, E_z) = \sum_j \sum_i I_i^{MX/XM} \left| U_{ij}^{MX/XM} \right|^2 e^{-\left(\varepsilon - \varepsilon_j^{MX/XM}(E_z)\right)^2 / 2w_i^2} \tag{5.7}$$

For a laser spot covering multiple triangular domains, the excitonic response should be an average over the individual MX and XM domains' responses:

$$I(\varepsilon,\, E_z) = \alpha I^{MX} + (1-\alpha) I^{XM} \tag{5.8}$$

As a result, Table 5.3 demonstrates the parameters used to plot the reconstructed spectra shown in Figs. 5.11a, b.

Table 5.3: Fitting parameters for exciton hybridizations averaged over both domains

parameters	device W1		device W2	
	MX	XM	MX	XM
I_{1S}^{top}	0.5	0.5	0.3	0.3
I_{1S}^{bot}	0.5	0.5	1.0	1.0
I_{1S}^{top}	0.05	0.05	0.015	0.015
I_{1S}^{bot}	0.05	0.05	0.05	0.05
I_{DX}^{u}	0	0	0	0
I_{DX}^{d}	0	0	0	0
w_{1S}^{top}	4.5 meV	4.5 meV	4.0 meV	4.0 meV
w_{1S}^{bot}	4.5 meV	4.5 meV	4.0 meV	4.0 meV
w_{1S}^{top}	3.5 meV	3.5 meV	3.5 meV	3.5 meV
w_{1S}^{bot}	3.5 meV	3.5 meV	3.5 meV	3.5 meV
w_{DX}^{u}	N/A	N/A	N/A	N/A
w_{DX}^{d}	N/A	N/A	N/A	N/A
α	50%		25%	

We have assumed negligible optical oscillator strength of the $|DX_{\downarrow\uparrow}\rangle$ dark states. Like the every-other-layer dipolar excitons in Chapter 3.3, $|DX_{\downarrow\uparrow}\rangle$ states become visible through hybridization with intralayer 1S/2S states.

Alternatively, we can average the same parameters from MX and XM results by putting dipolar exciton states from MX and XM domains into one eight-dimension Hamiltonian, as written below in (5.9), which also indicates the possibility of hybridization between dipolar excitons from different domains through a second-order carrier hopping process.

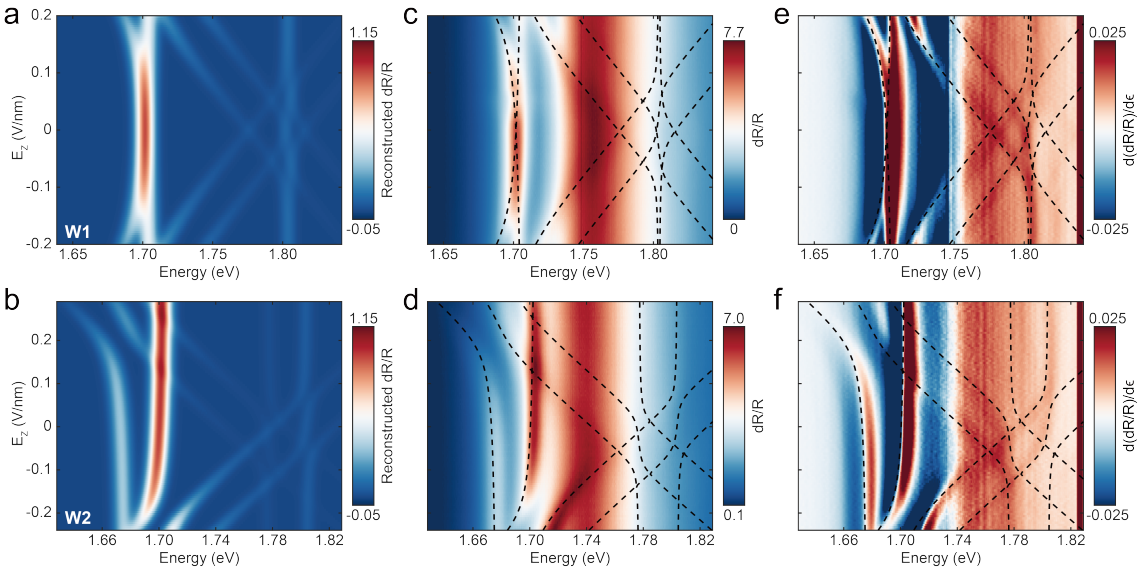

Figure 5.12: Modeling and reconstructing the exciton hybridizations coupled with both domains in W1 and W2. a,b, Reconstructed field dependent dR/R spectra in W1 (**a**) and W2 (**b**). **c,d,** Simulated field dependent dR/R spectra in W1 (**c**) and W2 (**d**). **e,f,** Simulated field dependent dR/R spectra that are differentiated with respect to photon energy in W1 (**e**) and W2 (**f**).

$$H_0 + H_1 = \begin{pmatrix} \varepsilon_{1S}^{top} & 0 & t_e^{(1)} & t_h^{(1)} & t_e^{(1)} & t_h^{(1)} & 0 & 0 \\ 0 & \varepsilon_{1S}^{bot} & t_h^{(1)} & t_e^{(1)} & t_h^{(1)} & t_e^{(1)} & 0 & 0 \\ \overline{t_e^{(1)}} & \overline{t_h^{(1)}} & \varepsilon_{DX\uparrow}^{MX} & 0 & 0 & 0 & t_e^{(2)} & t_h^{(2)} \\ \overline{t_h^{(1)}} & \overline{t_e^{(1)}} & 0 & \varepsilon_{DX\downarrow}^{MX} & 0 & 0 & t_h^{(2)} & t_e^{(2)} \\ \overline{t_e^{(1)}} & \overline{t_h^{(1)}} & 0 & 0 & \varepsilon_{DX\uparrow}^{XM} & 0 & t_e^{(2)} & t_h^{(2)} \\ \overline{t_h^{(1)}} & \overline{t_e^{(1)}} & 0 & 0 & 0 & \varepsilon_{DX\downarrow}^{XM} & t_h^{(2)} & t_e^{(2)} \\ 0 & 0 & t_e^{(2)} & t_h^{(2)} & t_e^{(2)} & t_h^{(2)} & \varepsilon_{2S}^{top} & 0 \\ 0 & 0 & t_h^{(2)} & t_e^{(2)} & t_h^{(2)} & t_e^{(2)} & 0 & \varepsilon_{2S}^{bot} \end{pmatrix} \tag{5.9}$$

We can obtain a better simulation and spectra reconstruction as shown in Fig. 5.12, with all the fitting parameters in Table 5.4.

Table 5.4: Fitting parameters for exciton hybridizations coupled with both domains

parameters	device W1	device W2
ε_{1S}^{top}	1.707 eV	1.677 eV
ε_{1S}^{bot}	1.707 eV	1.704 eV
ε_{DX}^{u}	1.792 eV	1.763 eV
ε_{DX}^{d}	1.792 eV	1.801 eV
ε_{2S}^{top}	1.804 eV	1.777 eV
ε_{2S}^{bot}	1.804 eV	1.804 eV
d	0.80 nm	0.80 nm
E_i^{MX}	0.055 V/nm	0.060 V/nm
E_i^{XM}	0.050 V/nm	0.060 V/nm
$t_e^{(1)}$	15 meV	13 meV
$t_e^{(2)}$	5 meV	5 meV
$t_h^{(1)}$	0	0
$t_h^{(2)}$	0	0

Furthermore, if we add a Gaussian peak to mimic the broad interference background, we finally obtain a perfect reconstruction that primarily resembles the real data (Figs. 5.13a, b).

Similarly, we simulate and reconstruct the spectra from twisted $MoTe_2$ systems (Figs. 5.7a, c) with all the fitting parameters shown in Table 5.5. We find an absence of the coupling between the exciton hybridizations and the interfacial ferroelectricity, probably due to a larger twist angle (around 4°) and a smaller moiré periodicity and thus a more stiffen domain wall.

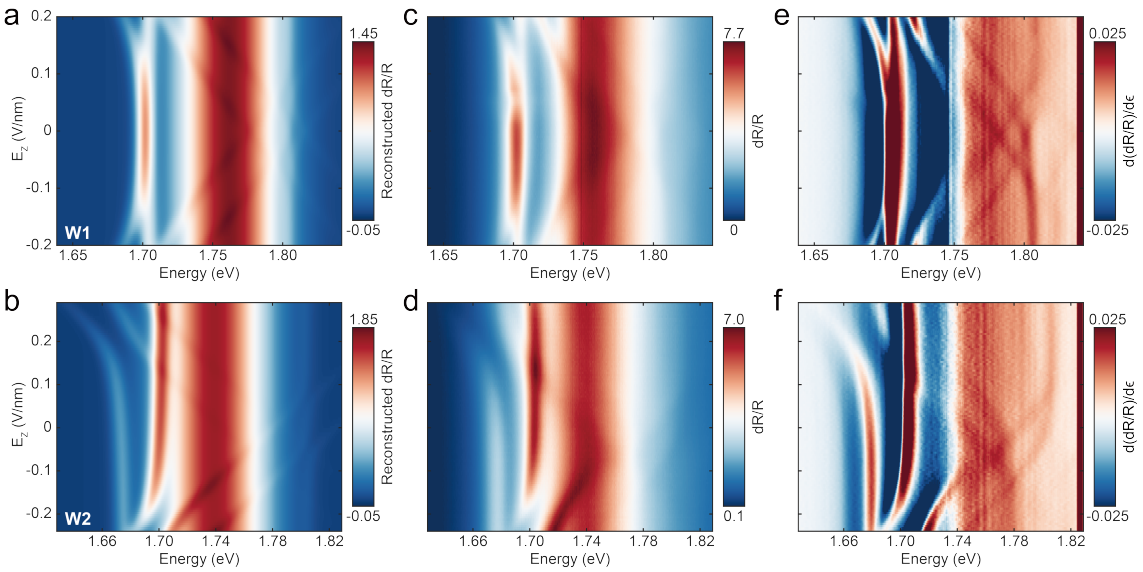

Figure 5.13: Modeling and reconstructing the background in W1 and W2. a,b, Reconstructed field dependent dR/R spectra in W1 (**a**) and W2 (**b**) by adding a broad background with a Gaussian profile. **c,d,** Measured electric field dependent dR/R spectra in W1 (**c**) and W2 (**d**) for comparison. **e,f,** Measured electric field dependent dR/R spectra that are differentiated with respect to photon energy in W1 (**e**) and W2 (**f**) for comparison.

Table 5.5: Fitting parameters for exciton hybridizations in twisted $MoTe_2$

parameters	T > 2K	T ~ 1.6K
ε_{1S}^{top}	1.125 eV	1.125 eV
ε_{1S}^{bot}	1.121 eV	1.121 eV
ε_{DX}^{u}	1.180 eV	1.180 eV
ε_{DX}^{d}	1.180 eV	1.180 eV
d	0.60 nm	0.60 nm
E_i	0	0
t_1	12 meV	14 meV
t_2	0	3 meV

5.4 MAGNETISM AND CORRELATED PHYSICS IN TWISTED BILAYER TMD

In the same twisted WSe_2 bilayer system, we also observe signatures of strong correlated phenomena, such as the sudden blueshifts of the excitonic signal in the dR/R spectra at around 5.0×10^{12} cm^{-2} hole doping density in Figs. 5.3a, c. The blueshift of the trion emission energy as well as the enhanced dR/R response is caused by the reduced dielectric screening from the insulating environment that results in a larger quasiparticle bandgap[22,99,100]. On the other hand, the insulating environment is caused by the incompressibility of the correlated states due to the formation of Mott insulator states[134-137] or band topology[9,17,151,161-163]. These correlated states can be directly characterized by quantum capacitance[164,165] and Hall measurements[45].

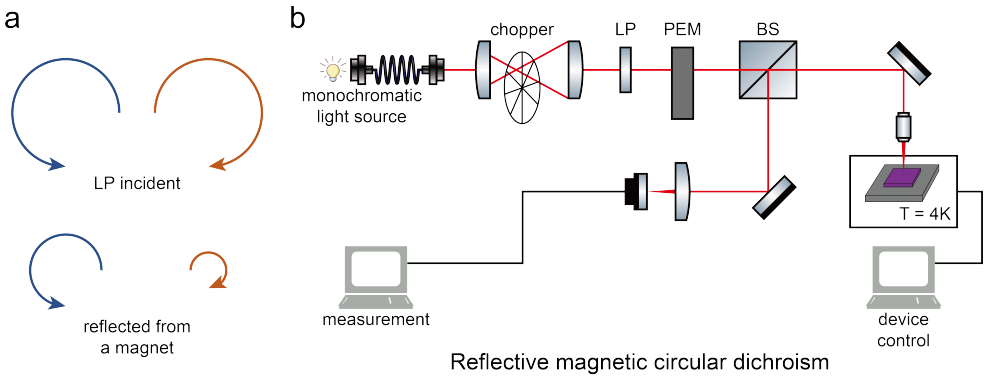

Figure 5.14: Experimental setups for RMCD measurement. a, Schematic of the RCP (orange) and LCP (blue) components from a linearly polarized laser before and after being reflected from a magnet. **b,** Schematic of light paths in RMCD measurement. BS, LP and PEM denote beamsplitter, linear polarizer and photoelastic modulator, respectively.

Furthermore, magnetism can appear as carriers are strongly correlated due to strong exchange interactions[18]. To probe the magnetism, a simple and non-destructive way is to leverage

light-matter interaction, i.e., the magneto-optic effect, where the magnetization of a 2D thin film can be characterized by the polarization change of the reflected light. Materials that exhibit an out-of-plane magnetization may display magnetic circular birefringence (MCB) and magnetic circular dichroism (MCD). Both MCB and MCD accrue a difference in the phase and amplitude, respectively, between right- and left-circularly polarized light that vary as a function of the out-of-plane magnetization. When linearly polarized light, which is an equal superposition of RCP and LCP, is normally incident and reflects off the magnetized material, the phase difference between RCP and LCP leads to a rotation of the linear polarization through an angle θ_K from the magneto-optical Kerr effect (MOKE) and induces ellipticity through reflective magnetic circular dichroism (RMCD)[10,11,173] (Fig. 5.14a).

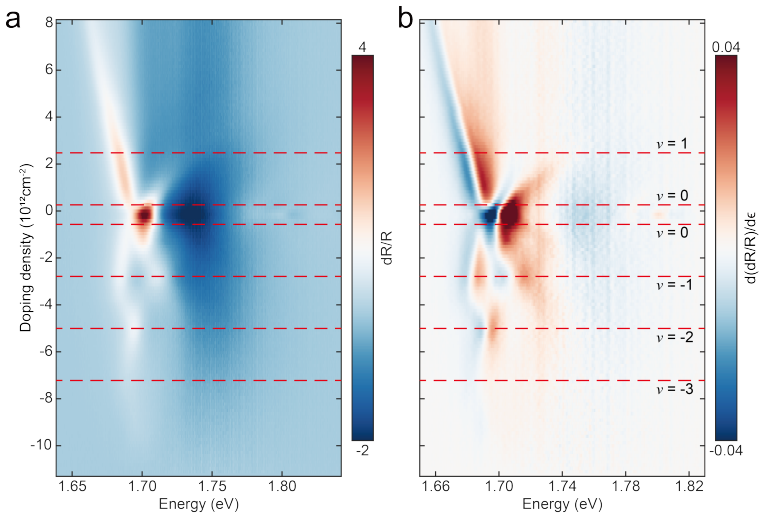

Figure 5.15: Filling factor assignments for device W1. a,b, Doping density dependences of dR/R resonances (**a**) and differentiated dR/R (**b**) from W1, with red dashed lines indicating the possible filling factor assignments.

To probe possible ferromagnetism, where a hysteresis loop and a remanent magnetization are presented, we perform RMCD measurements in a closed-cycle helium cryostat with a base temperature of around 2 K. A superconducting solenoidal magnet allows fields of up to 7 T in the

Faraday geometry to be applied on all devices. A photoelastic modulator (PEM) is used as a time-dependent waveplate that switches a 45° (relative to PEM's fast axis) linearly polarized light between RCP and LCP at a high frequency (tens of kHz) (Fig. 5.14b). The reflected light is amplified by an avalanche photodiode (APD) that has a high gain and signal-to-noise ratio. The circular dichroism signal, or the modulation between the RCP and LCP components, is further captured by an AC lock-in amplifier with the lock-in frequency set to the fundamental frequency of the PEM. In addition, the power of the reflected laser is also captured by the lock-in amplifier as a reference signal with the lock-in frequency set to the frequency of a chopper that periodically blocks the laser and modulates its power (at hundreds of Hz).

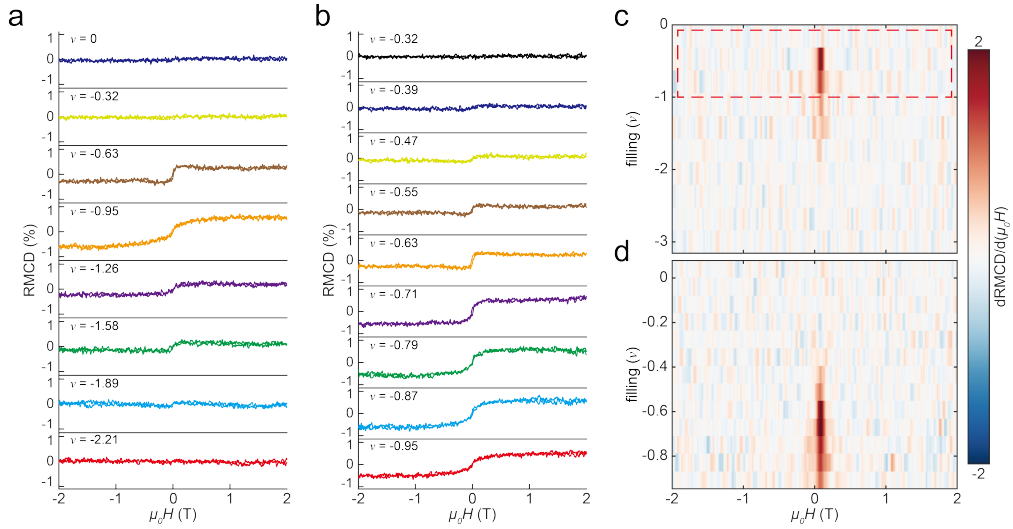

Figure 5.16: Doping density dependent RMCD in W1. a,b, RMCD signal versus magnetic field swept back and forth at roughly (**a**) and finely (**b**) selected fillings. **c,d,** Rough (**c**) and fine (**d**) doping density dependences of RMCD signals differentiated with respect to magnetic field.

Figure 5.15 demonstrates the RMCD from the R-stacked twisted WSe_2 bilayer device W1 as a function of different doping density and the external out-of-plane magnetic field that is applied by the superconducting solenoidal magnet from the cryostat. The filling factor ν stands for the

number of carriers (with positive/negative ν stands for electron/hole doping) per moiré supercell, which is calculated by correlating the Landau fan data with the doping dependence of the dR/R spectra. The possible filling factor assignments are therefore plotted in Figs. 5.15a, b. We notice at around ν = -0.5 to ν = -1.0 hole-doping range (as zoomed in Figs. 5.15b, d), a nonlinear step-like feature appears when the magnetic field switching directions. Furthermore, while sweeping the external magnetic field at opposite directions, a finite hysteresis loop can be observed. The hysteresis loop finds its maximum at around ν = -0.63 filling factor. Therefore, we also measure the hysteresis loop at ν = -0.63 with varying temperatures to investigate its magnetic phase transition, as shown in Fig. 5.17. The step-like loop disappears at a Curie temperature around 25 K. Compared to the magnetic correlated states in R-stacked twisted $MoTe_2$ systems[9,18], twisted WSe_2 systems possess a smaller loop possibly due to material intrinsic properties and sample inhomogeneity.

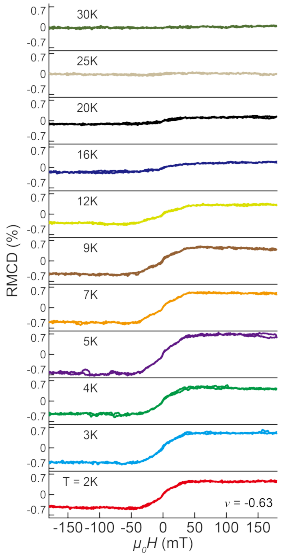

Figure 5.17: Temperature dependent RMCD at ν = -0.63. The RMCD signals degrade at an increasing temperature. The Curie temperature is around 25 K.

Combined with the previous observation of interfacial ferroelectricity, the discovery of magnetic correlated states in twisted WSe_2 indicates possible multiferroics due to the formation of

the moiré superlattice. However, the interfacial ferroelectricity is caused by the periodic distribution of the atomic stacking orders (MX and XM) in the moiré superlattice[109], while the ferromagnetism is caused by the strongly correlated carriers[9,18]. Yet further evidence is needed for the confirmation of the ferromagnetism. For instance, the observed hysteresis loop might be caused by light induced ferromagnetism[174]. Also, transport measurement with a dilution temperature should be performed to observe the consequent anomalous Hall effect[17]. This topic is of great interests and worth further investigation.

5.5 SUMMARY AND APPLICATIONS

In conclusion, in this project and material system, we first identify anti-crossing features in the out-of-plane electric field dependence of the dR/R spectra, indicating a similar exciton hybridization behavior mentioned in Chapter 3. An asymmetric electron hopping with a forbidden hole hopping between the adjacent layers is concluded, possibly due to the carrier wavefunction diffusion over the moiré supercell. We then observe a double-crossing fine feature for the interlayer dipolar excitons, which is caused by the coupling between the dipolar excitons and the alternating domain polarizations mentioned in Chapter 4. We further build a model that couples the exciton hybridization with the interfacial ferroelectricity and reconstruct the dR/R spectra of R-stacked twisted WSe_2, which primarily resembles the measured spectra. Finally, possible magnetic correlated states are identified at around ν = -0.5 to ν = -1.0 hole-doping range. The Curie temperature of the ferromagnetism is around 25 K.

Therefore, we prove that twisted bilayer TMD systems are great candidates for ferroelectric and ferromagnetic thin films, with industrial applications such as FeRAM/FeFET[103-106,129] and MTJ[175]. Also, I think these artificial material engineering methods can be used to inspire the research of other material systems. For instance, we can use the formation of the moiré superlattice as a new tuning knob, that can change and manipulate materials' properties and give rise to

emergent phenomena. Once again, laser probing method is proved to be a powerful characterization that is highly localized, non-destructive, and interactive with semiconducting materials.

Bibliography

1 Geim, A. K. & Novoselov, K. S. The rise of graphene. *Nature Materials* **6**, 183-191, doi:10.1038/nmat1849 (2007).

2 Xie, H. *et al.* Tunable Exciton-Optomechanical Coupling in Suspended Monolayer MoSe2. *Nano Letters* **21**, 2538-2543, doi:10.1021/acs.nanolett.0c05089 (2021).

3 Šiškins, M. *et al.* Magnetic and electronic phase transitions probed by nanomechanical resonators. *Nature Communications* **11**, 2698, doi:10.1038/s41467-020-16430-2 (2020).

4 Zhang, Y., Felser, C. & Fu, L. Moir\'e metal for catalysis. *Physical Review B* **110**, L041407, doi:10.1103/PhysRevB.110.L041407 (2024).

5 Ma, X., Luo, W., Yan, M., He, L. & Mai, L. In situ characterization of electrochemical processes in one dimensional nanomaterials for energy storages devices. *Nano Energy* **24**, 165-188, doi:https://doi.org/10.1016/j.nanoen.2016.03.023 (2016).

6 Lindlau, J. *et al.* The role of momentum-dark excitons in the elementary optical response of bilayer WSe2. *Nature Communications* **9**, 2586, doi:10.1038/s41467-018-04877-3 (2018).

7 Terrones, H. & Terrones, M. Bilayers of transition metal dichalcogenides: Different stackings and heterostructures. *Journal of Materials Research* **29**, 373-382, doi:10.1557/jmr.2013.284 (2014).

8 Cheiwchanchamnangij, T. & Lambrecht, W. R. L. Quasiparticle band structure calculation of monolayer, bilayer, and bulk MoS2. *Physical Review B* **85**, 205302, doi:10.1103/PhysRevB.85.205302 (2012).

9 Cai, J. *et al.* Signatures of fractional quantum anomalous Hall states in twisted MoTe2. *Nature* **622**, 63-68, doi:10.1038/s41586-023-06289-w (2023).

10 Huang, B. *et al.* Layer-dependent ferromagnetism in a van der Waals crystal down to the monolayer limit. *Nature* **546**, 270-273, doi:10.1038/nature22391 (2017).

11 Huang, B. *et al.* Electrical control of 2D magnetism in bilayer CrI3. *Nature Nanotechnology* **13**, 544-548, doi:10.1038/s41565-018-0121-3 (2018).

12 Deng, Y. *et al.* Gate-tunable room-temperature ferromagnetism in two-dimensional Fe3GeTe2. *Nature* **563**, 94-99, doi:10.1038/s41586-018-0626-9 (2018).

13 Fei, Z. *et al.* Two-dimensional itinerant ferromagnetism in atomically thin Fe3GeTe2. *Nature Materials* **17**, 778-782, doi:10.1038/s41563-018-0149-7 (2018).

14 Geim, A. K. & Grigorieva, I. V. Van der Waals heterostructures. *Nature* **499**, 419-425, doi:10.1038/nature12385 (2013).

15 Mak, K. F., Lee, C., Hone, J., Shan, J. & Heinz, T. F. Atomically Thin MoS2: A New Direct-Gap Semiconductor. *Physical Review Letters* **105**, 136805, doi:10.1103/PhysRevLett.105.136805 (2010).

16 Zhang, Y. *et al.* Every-other-layer dipolar excitons in a spin-valley locked superlattice. *Nature Nanotechnology* **18**, 501-506, doi:10.1038/s41565-023-01350-1 (2023).

17 Park, H. *et al.* Observation of fractionally quantized anomalous Hall effect. *Nature* **622**, 74-79, doi:10.1038/s41586-023-06536-0 (2023).

18 Anderson, E. *et al.* Programming correlated magnetic states with gate-controlled moiré geometry. *Science* **381**, 325-330, doi:doi:10.1126/science.adg4268 (2023).

19 Mak, K. F. & Shan, J. Photonics and optoelectronics of 2D semiconductor transition metal dichalcogenides. *Nature Photonics* **10**, 216-226, doi:10.1038/nphoton.2015.282 (2016).

20 Chernikov, A. *et al.* Exciton Binding Energy and Nonhydrogenic Rydberg Series in Monolayer WS2. *Physical Review Letters* **113**, 076802, doi:10.1103/PhysRevLett.113.076802 (2014).

21 Thygesen, K. S. Calculating excitons, plasmons, and quasiparticles in 2D materials and van der Waals heterostructures. *2D Materials* **4**, 022004, doi:10.1088/2053-1583/aa6432 (2017).

22 Wang, G. *et al.* Colloquium: Excitons in atomically thin transition metal dichalcogenides. *Reviews of Modern Physics* **90**, 021001, doi:10.1103/RevModPhys.90.021001 (2018).

23 Xiao, D., Liu, G.-B., Feng, W., Xu, X. & Yao, W. Coupled Spin and Valley Physics in Monolayers of MoS2 and Other Group-VI Dichalcogenides. *Physical Review Letters* **108**, 196802, doi:10.1103/PhysRevLett.108.196802 (2012).

24 Mak, K. F., He, K., Shan, J. & Heinz, T. F. Control of valley polarization in monolayer MoS2 by optical helicity. *Nature Nanotechnology* **7**, 494-498, doi:10.1038/nnano.2012.96 (2012).

25 Cao, T. *et al.* Valley-selective circular dichroism of monolayer molybdenum disulphide. *Nature Communications* **3**, 887, doi:10.1038/ncomms1882 (2012).

26 Zhang, X., Shan, W.-Y. & Xiao, D. Optical Selection Rule of Excitons in Gapped Chiral Fermion Systems. *Physical Review Letters* **120**, 077401, doi:10.1103/PhysRevLett.120.077401 (2018).

27 Kappera, R. *et al.* Phase-engineered low-resistance contacts for ultrathin MoS2 transistors. *Nature Materials* **13**, 1128-1134, doi:10.1038/nmat4080 (2014).

28 Zhang, L. *et al.* Three-Dimensional Spirals of Atomic Layered MoS2. *Nano Letters* **14**, 6418-6423, doi:10.1021/nl502961e (2014).

29 Song, I., Park, C. & Choi, H. C. Synthesis and properties of molybdenum disulphide: from bulk to atomic layers. *RSC Advances* **5**, 7495-7514, doi:10.1039/C4RA11852A (2015).

30 Blake, P. *et al.* Making graphene visible. *Applied Physics Letters* **91**, doi:10.1063/1.2768624 (2007).

31 Coburn, J. W. & Winters, H. F. Plasma etching—A discussion of mechanisms. *Journal of Vacuum Science and Technology* **16**, 391-403, doi:10.1116/1.569958 (1979).

32 Shun'ko, E. V. & Belkin, V. S. Cleaning properties of atomic oxygen excited to metastable state 2s22p4(S1). *Journal of Applied Physics* **102**, doi:10.1063/1.2794857 (2007).

33 Novoselov, K. S. & Castro Neto, A. H. Two-dimensional crystals-based heterostructures: materials with tailored properties. *Physica Scripta* **2012**, 014006, doi:10.1088/0031-8949/2012/T146/014006 (2012).

34 McGilly, L. J. *et al.* Visualization of moiré superlattices. *Nature Nanotechnology* **15**, 580-584, doi:10.1038/s41565-020-0708-3 (2020).

35 Kang, J., Liu, W., Sarkar, D., Jena, D. & Banerjee, K. Computational Study of Metal Contacts to Monolayer Transition-Metal Dichalcogenide Semiconductors. *Physical Review X* **4**, 031005, doi:10.1103/PhysRevX.4.031005 (2014).

36 Wang, Z., Zhao, L., Mak, K. F. & Shan, J. Probing the Spin-Polarized Electronic Band Structure in Monolayer Transition Metal Dichalcogenides by Optical Spectroscopy. *Nano Letters* **17**, 740-746, doi:10.1021/acs.nanolett.6b03855 (2017).

37 Movva, H. C. P. *et al.* Density-Dependent Quantum Hall States and Zeeman Splitting in Monolayer and Bilayer WSe2. *Physical Review Letters* **118**, 247701, doi:10.1103/PhysRevLett.118.247701 (2017).

38 Boyd, R. W. in *Nonlinear Optics (Third Edition)* (ed Robert W. Boyd) 1-67 (Academic Press, 2008).

39 Seyler, K. L. *et al.* Electrical control of second-harmonic generation in a WSe2 monolayer transistor. *Nature Nanotechnology* **10**, 407-411, doi:10.1038/nnano.2015.73 (2015).

40 Rivera, P. *et al.* Valley-polarized exciton dynamics in a 2D semiconductor heterostructure. *Science* **351**, 688-691, doi:doi:10.1126/science.aac7820 (2016).

41 Schaibley, J. R. *et al.* Directional interlayer spin-valley transfer in two-dimensional heterostructures. *Nature Communications* **7**, 13747, doi:10.1038/ncomms13747 (2016).

42 Yankowitz, M. *et al.* Emergence of superlattice Dirac points in graphene on hexagonal boron nitride. *Nature Physics* **8**, 382-386, doi:10.1038/nphys2272 (2012).

43 Wang, L. *et al.* One-Dimensional Electrical Contact to a Two-Dimensional Material. *Science* **342**, 614-617, doi:doi:10.1126/science.1244358 (2013).

44 Rosenberger, M. R. *et al.* Nano-"Squeegee" for the Creation of Clean 2D Material Interfaces. *ACS Applied Materials & Interfaces* **10**, 10379-10387, doi:10.1021/acsami.8b01224 (2018).

45 Klitzing, K. v., Dorda, G. & Pepper, M. New Method for High-Accuracy Determination of the Fine-Structure Constant Based on Quantized Hall Resistance. *Physical Review Letters* **45**, 494-497, doi:10.1103/PhysRevLett.45.494 (1980).

46 Frenkel, J. On the Transformation of light into Heat in Solids. I. *Physical Review* **37**, 17-44, doi:10.1103/PhysRev.37.17 (1931).

47 Knox, R. S. Theory of excitons. *Solid state physics* **3** (1963).

48 Mueller, T. & Malic, E. Exciton physics and device application of two-dimensional transition metal dichalcogenide semiconductors. *npj 2D Materials and Applications* **2**, 29, doi:10.1038/s41699-018-0074-2 (2018).

49 Combescot, M. & Shiau, S.-Y. *Excitons and Cooper pairs: two composite bosons in many-body physics*. (Oxford University Press, 2015).

50 Fox, M. *Optical properties of solids*. Vol. 3 (Oxford university press, 2010).

51 Round, H. J. Light-emitting diodes hit the centenary milestone. *Electr. World* **19**, 309-310 (1907).

52 Ross, J. S. *et al.* Electrical control of neutral and charged excitons in a monolayer semiconductor. *Nature Communications* **4**, 1474, doi:10.1038/ncomms2498 (2013).

53 Teets, T. S. *Photoluminescence*. (American Chemical Society, 2021).

54 Splendiani, A. *et al.* Emerging Photoluminescence in Monolayer MoS2. *Nano Letters* **10**, 1271-1275, doi:10.1021/nl903868w (2010).

55 Lehovec, K., Accardo, C. A. & Jamgochian, E. Injected Light Emission of Silicon Carbide Crystals. *Physical Review* **83**, 603-607, doi:10.1103/PhysRev.83.603 (1951).

56 Lehovec, K., Accardo, C. A. & Jamgochian, E. Light Emission Produced by Current Injected into a Green Silicon-Carbide Crystal. *Physical Review* **89**, 20-25, doi:10.1103/PhysRev.89.20 (1953).

57 Wang, G. *et al.* Exciton dynamics in WSe2 bilayers. *Applied Physics Letters* **105**, doi:10.1063/1.4900945 (2014).

58 Robert, C. *et al.* Fine structure and lifetime of dark excitons in transition metal dichalcogenide monolayers. *Physical Review B* **96**, 155423, doi:10.1103/PhysRevB.96.155423 (2017).

59 Moody, G., Schaibley, J. & Xu, X. Exciton dynamics in monolayer transition metal dichalcogenides [Invited]. *J. Opt. Soc. Am. B* **33**, C39-C49, doi:10.1364/JOSAB.33.000C39 (2016).

60 Schaibley, J. R. *et al.* Valleytronics in 2D materials. *Nature Reviews Materials* **1**, 16055, doi:10.1038/natrevmats.2016.55 (2016).

61 Zhang, X.-X., You, Y., Zhao, S. Y. F. & Heinz, T. F. Experimental Evidence for Dark Excitons in Monolayer WSe2. *Physical Review Letters* **115**, 257403, doi:10.1103/PhysRevLett.115.257403 (2015).

62 Zhang, X.-X. *et al.* Magnetic brightening and control of dark excitons in monolayer WSe2. *Nature Nanotechnology* **12**, 883-888, doi:10.1038/nnano.2017.105 (2017).

63 Zhou, Y. *et al.* Probing dark excitons in atomically thin semiconductors via near-field coupling to surface plasmon polaritons. *Nature Nanotechnology* **12**, 856-860, doi:10.1038/nnano.2017.106 (2017).

64 Wang, G. *et al.* In-Plane Propagation of Light in Transition Metal Dichalcogenide Monolayers: Optical Selection Rules. *Physical Review Letters* **119**, 047401, doi:10.1103/PhysRevLett.119.047401 (2017).

65 Rivera, P. *et al.* Intrinsic donor-bound excitons in ultraclean monolayer semiconductors. *Nature Communications* **12**, 871, doi:10.1038/s41467-021-21158-8 (2021).

66 He, M. *et al.* Valley phonons and exciton complexes in a monolayer semiconductor. *Nature Communications* **11**, 618, doi:10.1038/s41467-020-14472-0 (2020).

67 Seyler, K. L. *et al.* Signatures of moiré-trapped valley excitons in MoSe2/WSe2 heterobilayers. *Nature* **567**, 66-70, doi:10.1038/s41586-019-0957-1 (2019).

68 Wang, X. *et al.* Moiré trions in MoSe2/WSe2 heterobilayers. *Nature Nanotechnology* **16**, 1208-1213, doi:10.1038/s41565-021-00969-2 (2021).

69 Sung, J. *et al.* Broken mirror symmetry in excitonic response of reconstructed domains in twisted MoSe2/MoSe2 bilayers. *Nature Nanotechnology* **15**, 750-754, doi:10.1038/s41565-020-0728-z (2020).

70 Wang, Z. *et al.* Intravalley Spin–Flip Relaxation Dynamics in Single-Layer WS2. *Nano Letters* **18**, 6882-6891, doi:10.1021/acs.nanolett.8b02774 (2018).

71 Plechinger, G. *et al.* Trion fine structure and coupled spin–valley dynamics in monolayer tungsten disulfide. *Nature Communications* **7**, 12715, doi:10.1038/ncomms12715 (2016).

72 Hill, H. M. *et al.* Observation of Excitonic Rydberg States in Monolayer MoS2 and WS2 by Photoluminescence Excitation Spectroscopy. *Nano Letters* **15**, 2992-2997, doi:10.1021/nl504868p (2015).

73 Jones, A. M. *et al.* Spin–layer locking effects in optical orientation of exciton spin in bilayer WSe2. *Nature Physics* **10**, 130-134, doi:10.1038/nphys2848 (2014).

74 Wang, Z., Chiu, Y.-H., Honz, K., Mak, K. F. & Shan, J. Electrical Tuning of Interlayer Exciton Gases in WSe2 Bilayers. *Nano Letters* **18**, 137-143, doi:10.1021/acs.nanolett.7b03667 (2018).

75 Altaiary, M. M. *et al.* Electrically Switchable Intervalley Excitons with Strong Two-Phonon Scattering in Bilayer WSe2. *Nano Letters* **22**, 1829-1835, doi:10.1021/acs.nanolett.1c01590 (2022).

76 Bistritzer, R. & MacDonald, A. H. Moiré bands in twisted double-layer graphene. *Proceedings of the National Academy of Sciences* **108**, 12233-12237, doi:doi:10.1073/pnas.1108174108 (2011).

77 Cao, Y. *et al.* Unconventional superconductivity in magic-angle graphene superlattices. *Nature* **556**, 43-50, doi:10.1038/nature26160 (2018).

78 Song, T. *et al.* Switching 2D magnetic states via pressure tuning of layer stacking. *Nature Materials* **18**, 1298-1302, doi:10.1038/s41563-019-0505-2 (2019).

79 Li, T. *et al.* Pressure-controlled interlayer magnetism in atomically thin CrI3. *Nature Materials* **18**, 1303-1308, doi:10.1038/s41563-019-0506-1 (2019).

80 Yasuda, K., Wang, X., Watanabe, K., Taniguchi, T. & Jarillo-Herrero, P. Stacking-engineered ferroelectricity in bilayer boron nitride. *Science* **372**, 1458-1462, doi:doi:10.1126/science.abd3230 (2021).

81 Woods, C. R. *et al.* Charge-polarized interfacial superlattices in marginally twisted hexagonal boron nitride. *Nature Communications* **12**, 347, doi:10.1038/s41467-020-20667-2 (2021).

82 Vizner Stern, M. *et al.* Interfacial ferroelectricity by van der Waals sliding. *Science* **372**, 1462-1466, doi:doi:10.1126/science.abe8177 (2021).

83 Wu, S. *et al.* Electrical tuning of valley magnetic moment through symmetry control in bilayer MoS2. *Nature Physics* **9**, 149-153, doi:10.1038/nphys2524 (2013).

84 Zeng, H., Dai, J., Yao, W., Xiao, D. & Cui, X. Valley polarization in MoS2 monolayers by optical pumping. *Nature Nanotechnology* **7**, 490-493, doi:10.1038/nnano.2012.95 (2012).

85 Gong, Z. *et al.* Magnetoelectric effects and valley-controlled spin quantum gates in transition metal dichalcogenide bilayers. *Nature Communications* **4**, 2053, doi:10.1038/ncomms3053 (2013).

86 Shi, Q. *et al.* Bilayer WSe2 as a natural platform for interlayer exciton condensates in the strong coupling limit. *Nature Nanotechnology* **17**, 577-582, doi:10.1038/s41565-022-01104-5 (2022).

87 Yankowitz, M., McKenzie, D. & LeRoy, B. J. Local Spectroscopic Characterization of Spin and Layer Polarization in WSe2. *Physical Review Letters* **115**, 136803, doi:10.1103/PhysRevLett.115.136803 (2015).

88 Bawden, L. *et al.* Spin–valley locking in the normal state of a transition-metal dichalcogenide superconductor. *Nature Communications* **7**, 11711, doi:10.1038/ncomms11711 (2016).

89 Slobodeniuk, A. O. *et al.* Fine structure of K-excitons in multilayers of transition metal dichalcogenides. *2D Materials* **6**, 025026, doi:10.1088/2053-1583/ab0776 (2019).

90 Liu, G.-B., Shan, W.-Y., Yao, Y., Yao, W. & Xiao, D. Three-band tight-binding model for monolayers of group-VIB transition metal dichalcogenides. *Physical Review B* **88**, 085433, doi:10.1103/PhysRevB.88.085433 (2013).

91 Wilson, N. R. *et al.* Determination of band offsets, hybridization, and exciton binding in 2D semiconductor heterostructures. *Science Advances* **3**, e1601832, doi:doi:10.1126/sciadv.1601832 (2017).

92 Shih, Y. C. A. & Streetman, B. G. Photoluminescence of AlAs/GaAs superlattice quantum wells. *Applied Physics Letters* **62**, 2655-2657, doi:10.1063/1.109276 (1993).

93 Król, M. *et al.* Exciton-polaritons in multilayer WSe2 in a planar microcavity. *2D Materials* **7**, 015006, doi:10.1088/2053-1583/ab4b14 (2020).

94 Arora, A. *et al.* Valley-contrasting optics of interlayer excitons in Mo- and W-based bulk transition metal dichalcogenides. *Nanoscale* **10**, 15571-15577, doi:10.1039/C8NR03764G (2018).

95 Raiber, S. *et al.* Ultrafast pseudospin quantum beats in multilayer WSe2 and MoSe2. *Nature Communications* **13**, 4997, doi:10.1038/s41467-022-32534-3 (2022).

96 Shimazaki, Y. *et al.* Strongly correlated electrons and hybrid excitons in a moiré heterostructure. *Nature* **580**, 472-477, doi:10.1038/s41586-020-2191-2 (2020).

97 Yoo, H. *et al.* Atomic and electronic reconstruction at the van der Waals interface in twisted bilayer graphene. *Nature Materials* **18**, 448-453, doi:10.1038/s41563-019-0346-z (2019).

98 Zhang, C. *et al.* Interlayer couplings, Moiré patterns, and 2D electronic superlattices in MoS2/WSe2 hetero-bilayers. *Science Advances* **3**, e1601459, doi:doi:10.1126/sciadv.1601459 (2017).

99 Raja, A. *et al.* Coulomb engineering of the bandgap and excitons in two-dimensional materials. *Nature Communications* **8**, 15251, doi:10.1038/ncomms15251 (2017).

100 Mhenni, A. B. *et al.* Breakdown of the static dielectric screening approximation of Coulomb interactions in atomically thin semiconductors. *arXiv preprint arXiv:2402.18639* (2024).

101 Känzig, W. in *Solid State Physics* Vol. 4 1-197 (Elsevier, 1957).

102 Lines, M. E. & Glass, A. M. *Principles and applications of ferroelectrics and related materials*. (Oxford university press, 2001).

103 Scott, J. F. & Paz de Araujo, C. A. Ferroelectric memories. *Science* **246**, 1400-1405 (1989).

104 Cui, C., Xue, F., Hu, W.-J. & Li, L.-J. Two-dimensional materials with piezoelectric and ferroelectric functionalities. *npj 2D Materials and Applications* **2**, 18 (2018).

105 Li, L. & Wu, M. Binary Compound Bilayer and Multilayer with Vertical Polarizations: Two-Dimensional Ferroelectrics, Multiferroics, and Nanogenerators. *ACS Nano* **11**, 6382-6388, doi:10.1021/acsnano.7b02756 (2017).

106 Wu, M. Two-Dimensional van der Waals Ferroelectrics: Scientific and Technological Opportunities. *ACS Nano* **15**, 9229-9237, doi:10.1021/acsnano.0c08483 (2021).

107 Zhuravlev, M. Y., Sabirianov, R. F., Jaswal, S. S. & Tsymbal, E. Y. Giant Electroresistance in Ferroelectric Tunnel Junctions. *Physical Review Letters* **94**, 246802, doi:10.1103/PhysRevLett.94.246802 (2005).

108 Chang, C. *et al.* Remote epitaxy of single-crystal rhombohedral WS2 bilayers. *Nature Communications* **15**, 4130, doi:10.1038/s41467-024-48522-8 (2024).

109 Wang, X. *et al.* Interfacial ferroelectricity in rhombohedral-stacked bilayer transition metal dichalcogenides. *Nature Nanotechnology* **17**, 367-371, doi:10.1038/s41565-021-01059-z (2022).

110 Wang, Y., Wang, Z., Yao, W., Liu, G.-B. & Yu, H. Interlayer coupling in commensurate and incommensurate bilayer structures of transition-metal dichalcogenides. *Physical Review B* **95**, 115429, doi:10.1103/PhysRevB.95.115429 (2017).

111 Park, J. *et al.* Optical control of the layer degree of freedom through Wannier–Stark states in polar 3R MoS2. *Journal of Physics: Condensed Matter* **31**, 315502, doi:10.1088/1361-648X/ab1d0f (2019).

112 Park, J., Yeu, I. W., Han, G., Hwang, C. S. & Choi, J.-H. Ferroelectric switching in bilayer 3R MoS2 via interlayer shear mode driven by nonlinear phononics. *Scientific Reports* **9**, 14919, doi:10.1038/s41598-019-50293-y (2019).

113 Kormányos, A., Zólyomi, V., Fal'ko, V. I. & Burkard, G. Tunable Berry curvature and valley and spin Hall effect in bilayer MoS2. *Physical Review B* **98**, 035408, doi:10.1103/PhysRevB.98.035408 (2018).

114 Andersen, T. I. *et al.* Excitons in a reconstructed moiré potential in twisted WSe2/WSe2 homobilayers. *Nature Materials* **20**, 480-487, doi:10.1038/s41563-020-00873-5 (2021).

115 Weston, A. *et al.* Atomic reconstruction in twisted bilayers of transition metal dichalcogenides. *Nature Nanotechnology* **15**, 592-597, doi:10.1038/s41565-020-0682-9 (2020).

116 Li, E. *et al.* Lattice reconstruction induced multiple ultra-flat bands in twisted bilayer WSe2. *Nature Communications* **12**, 5601, doi:10.1038/s41467-021-25924-6 (2021).

117 Shabani, S. *et al.* Deep moiré potentials in twisted transition metal dichalcogenide bilayers. *Nature Physics* **17**, 720-725, doi:10.1038/s41567-021-01174-7 (2021).

118 Naik, M. H. & Jain, M. Ultraflatbands and Shear Solitons in Moir\'e Patterns of Twisted Bilayer Transition Metal Dichalcogenides. *Physical Review Letters* **121**, 266401, doi:10.1103/PhysRevLett.121.266401 (2018).

119 Zhang, Z. *et al.* Flat bands in twisted bilayer transition metal dichalcogenides. *Nature Physics* **16**, 1093-1096, doi:10.1038/s41567-020-0958-x (2020).

120 Bennett, D. & Remez, B. On electrically tunable stacking domains and ferroelectricity in moiré superlattices. *npj 2D Materials and Applications* **6**, 7, doi:10.1038/s41699-021-00281-6 (2022).

121 Enaldiev, V. V., Ferreira, F. & Fal'ko, V. I. A Scalable Network Model for Electrically Tunable Ferroelectric Domain Structure in Twistronic Bilayers of Two-Dimensional Semiconductors. *Nano Letters* **22**, 1534-1540, doi:10.1021/acs.nanolett.1c04210 (2022).

122 Wang, L. *et al.* Correlated electronic phases in twisted bilayer transition metal dichalcogenides. *Nature Materials* **19**, 861-866, doi:10.1038/s41563-020-0708-6 (2020).

123 Kim, K. *et al.* van der Waals Heterostructures with High Accuracy Rotational Alignment. *Nano Letters* **16**, 1989-1995, doi:10.1021/acs.nanolett.5b05263 (2016).

124 Cao, Y. *et al.* Superlattice-Induced Insulating States and Valley-Protected Orbits in Twisted Bilayer Graphene. *Physical Review Letters* **117**, 116804, doi:10.1103/PhysRevLett.117.116804 (2016).

125 Güthner, P. & Dransfeld, K. Local poling of ferroelectric polymers by scanning force microscopy. *Applied Physics Letters* **61**, 1137-1139, doi:10.1063/1.107693 (1992).

126 El Ghanem, H. M., Saq'an, S. A., Al Saadi, M. & Sa'di M, A. J. On the electrical and optical properties of polycarbonate/MNCl 2 composite. *Journal of Modern Physics* **2011** (2011).

127 Nonnenmacher, M., O'Boyle, M. P. & Wickramasinghe, H. K. Kelvin probe force microscopy. *Applied Physics Letters* **58**, 2921-2923, doi:10.1063/1.105227 (1991).

128 Kelvin, L. V. Contact electricity of metals. *The London, Edinburgh, and Dublin Philosophical Magazine and Journal of Science* **46**, 82-120 (1898).

129 Yasuda, K. *et al.* Ultrafast high-endurance memory based on sliding ferroelectrics. *Science* **385**, 53-56, doi:doi:10.1126/science.adp3575 (2024).

130 Ghiotto, A. *et al.* Quantum criticality in twisted transition metal dichalcogenides. *Nature* **597**, 345-349, doi:10.1038/s41586-021-03815-6 (2021).

131 Foutty, B. A. *et al.* Mapping twist-tuned multiband topology in bilayer WSe2. *Science* **384**, 343-347, doi:doi:10.1126/science.adi4728 (2024).

132 Zeng, Y. *et al.* Thermodynamic evidence of fractional Chern insulator in moiré MoTe2. *Nature* **622**, 69-73, doi:10.1038/s41586-023-06452-3 (2023).

133 Wu, F., Lovorn, T., Tutuc, E. & MacDonald, A. H. Hubbard Model Physics in Transition Metal Dichalcogenide Moir\'e Bands. *Physical Review Letters* **121**, 026402, doi:10.1103/PhysRevLett.121.026402 (2018).

134 Tang, Y. *et al.* Simulation of Hubbard model physics in WSe2/WS2 moiré superlattices. *Nature* **579**, 353-358, doi:10.1038/s41586-020-2085-3 (2020).

135 Regan, E. C. *et al.* Mott and generalized Wigner crystal states in WSe2/WS2 moiré superlattices. *Nature* **579**, 359-363, doi:10.1038/s41586-020-2092-4 (2020).

136 Xu, Y. *et al.* Correlated insulating states at fractional fillings of moiré superlattices. *Nature* **587**, 214-218, doi:10.1038/s41586-020-2868-6 (2020).

137 Li, H. *et al.* Imaging two-dimensional generalized Wigner crystals. *Nature* **597**, 650-654, doi:10.1038/s41586-021-03874-9 (2021).

138 Li, T. *et al.* Continuous Mott transition in semiconductor moiré superlattices. *Nature* **597**, 350-354, doi:10.1038/s41586-021-03853-0 (2021).

139 Zhang, M. *et al.* Tuning Quantum Phase Transitions at Half Filling in MoTe2/WSe2 Moiré Superlattices. *Physical Review X* **12**, 041015, doi:10.1103/PhysRevX.12.041015 (2022).

140 Zhao, W. *et al.* Gate-tunable heavy fermions in a moiré Kondo lattice. *Nature* **616**, 61-65, doi:10.1038/s41586-023-05800-7 (2023).

141 Zhang, Y., Devakul, T. & Fu, L. Spin-textured Chern bands in AB-stacked transition metal dichalcogenide bilayers. *Proceedings of the National Academy of Sciences* **118**, e2112673118, doi:doi:10.1073/pnas.2112673118 (2021).

142 Li, T. *et al.* Quantum anomalous Hall effect from intertwined moiré bands. *Nature* **600**, 641-646, doi:10.1038/s41586-021-04171-1 (2021).

143 Zhao, W. *et al.* Realization of the Haldane Chern insulator in a moiré lattice. *Nature Physics* **20**, 275-280, doi:10.1038/s41567-023-02284-0 (2024).

144 Tao, Z. *et al.* Valley-Coherent Quantum Anomalous Hall State in AB-Stacked MoTe2/ WSe2 Bilayers. *Physical Review X* **14**, 011004, doi:10.1103/PhysRevX.14.011004 (2024).

145 Devakul, T., Crépel, V., Zhang, Y. & Fu, L. Magic in twisted transition metal dichalcogenide bilayers. *Nature Communications* **12**, 6730, doi:10.1038/s41467-021-27042-9 (2021).

146 Pan, H., Wu, F. & Das Sarma, S. Quantum phase diagram of a Moiré Hubbard model. *Physical Review B* **102**, 201104, doi:10.1103/PhysRevB.102.201104 (2020).

147 Yu, H., Chen, M. & Yao, W. Giant magnetic field from moiré induced Berry phase in homobilayer semiconductors. *National Science Review* **7**, 12-20, doi:10.1093/nsr/nwz117 (2019).

148 Zhang, Y., Liu, T. & Fu, L. Electronic structures, charge transfer, and charge order in twisted transition metal dichalcogenide bilayers. *Physical Review B* **103**, 155142, doi:10.1103/PhysRevB.103.155142 (2021).

149 Angeli, M. & MacDonald, A. H. Γ valley transition metal dichalcogenide moiré bands. *Proceedings of the National Academy of Sciences* **118**, e2021826118, doi:doi:10.1073/pnas.2021826118 (2021).

150 Wu, F., Lovorn, T., Tutuc, E., Martin, I. & MacDonald, A. H. Topological Insulators in Twisted Transition Metal Dichalcogenide Homobilayers. *Physical Review Letters* **122**, 086402, doi:10.1103/PhysRevLett.122.086402 (2019).

151 Crépel, V. & Fu, L. Anomalous Hall metal and fractional Chern insulator in twisted transition metal dichalcogenides. *Physical Review B* **107**, L201109, doi:10.1103/PhysRevB.107.L201109 (2023).

152 Kaushal, N., Morales-Durán, N., MacDonald, A. H. & Dagotto, E. Magnetic ground states of honeycomb lattice Wigner crystals. *Communications Physics* **5**, 289, doi:10.1038/s42005-022-01065-0 (2022).

153 Abouelkomsan, A., Bergholtz, E. J. & Chatterjee, S. Multiferroicity and Topology in Twisted Transition Metal Dichalcogenides. *Physical Review Letters* **133**, 026801, doi:10.1103/PhysRevLett.133.026801 (2024).

154 Haavisto, M., Lado, J. L. & Otero Fumega, A. Topological multiferroic order in twisted transition metal dichalcogenide bilayers. *SciPost Physics* **13**, 052 (2022).

155 Liu, G.-B., Xiao, D., Yao, Y., Xu, X. & Yao, W. Electronic structures and theoretical modelling of two-dimensional group-VIB transition metal dichalcogenides. *Chemical Society Reviews* **44**, 2643-2663, doi:10.1039/C4CS00301B (2015).

156 Ulstrup, S. *et al.* Direct observation of minibands in a twisted graphene/WS2 bilayer. *Science Advances* **6**, eaay6104, doi:doi:10.1126/sciadv.aay6104 (2020).

157 Cao, Y. *et al.* Correlated insulator behaviour at half-filling in magic-angle graphene superlattices. *Nature* **556**, 80-84, doi:10.1038/nature26154 (2018).

158 Marchenko, D. *et al.* Extremely flat band in bilayer graphene. *Science Advances* **4**, eaau0059, doi:doi:10.1126/sciadv.aau0059 (2018).

159 Xia, Y. *et al.* Unconventional superconductivity in twisted bilayer WSe2. *arXiv preprint arXiv:2405.14784* (2024).

160 Guo, Y. *et al.* Superconductivity in twisted bilayer WSe2. *arXiv preprint arXiv:2406.03418* (2024).

161 Zhao, Y.-F. *et al.* Tuning the Chern number in quantum anomalous Hall insulators. *Nature* **588**, 419-423, doi:10.1038/s41586-020-3020-3 (2020).

162 Shi, Q. *et al.* Odd- and even-denominator fractional quantum Hall states in monolayer WSe2. *Nature Nanotechnology* **15**, 569-573, doi:10.1038/s41565-020-0685-6 (2020).

163 Chang, C.-Z., Liu, C.-X. & MacDonald, A. H. Colloquium: Quantum anomalous Hall effect. *Reviews of Modern Physics* **95**, 011002, doi:10.1103/RevModPhys.95.011002 (2023).

164 Hunt, B. *et al.* Massive Dirac Fermions and Hofstadter Butterfly in a van der Waals Heterostructure. *Science* **340**, 1427-1430, doi:doi:10.1126/science.1237240 (2013).

165 Zibrov, A. A. *et al.* Even-denominator fractional quantum Hall states at an isospin transition in monolayer graphene. *Nature Physics* **14**, 930-935, doi:10.1038/s41567-018-0190-0 (2018).

166 Wang, X. *et al.* Intercell moiré exciton complexes in electron lattices. *Nature Materials* **22**, 599-604, doi:10.1038/s41563-023-01496-2 (2023).

167 Lezama, I. G. *et al.* Indirect-to-Direct Band Gap Crossover in Few-Layer MoTe2. *Nano Letters* **15**, 2336-2342, doi:10.1021/nl5045007 (2015).

168 Xu, X., Yao, W., Xiao, D. & Heinz, T. F. Spin and pseudospins in layered transition metal dichalcogenides. *Nature Physics* **10**, 343-350, doi:10.1038/nphys2942 (2014).

169 Liang, J. *et al.* Optically Probing the Asymmetric Interlayer Coupling in Rhombohedral-Stacked MoS2 Bilayer. *Physical Review X* **12**, 041005, doi:10.1103/PhysRevX.12.041005 (2022).

170 Zhang, X.-W. *et al.* Polarization-driven band topology evolution in twisted MoTe2 and WSe2. *Nature Communications* **15**, 4223, doi:10.1038/s41467-024-48511-x (2024).

171 Naik, M. H. *et al.* Intralayer charge-transfer moiré excitons in van der Waals superlattices. *Nature* **609**, 52-57, doi:10.1038/s41586-022-04991-9 (2022).

172 Susarla, S. *et al.* Hyperspectral imaging of exciton confinement within a moiré unit cell with a subnanometer electron probe. *Science* **378**, 1235-1239, doi:doi:10.1126/science.add9294 (2022).

173 Sato, K. Measurement of Magneto-Optical Kerr Effect Using Piezo-Birefringent Modulator. *Japanese Journal of Applied Physics* **20**, 2403, doi:10.1143/JJAP.20.2403 (1981).

174 Wang, X. *et al.* Light-induced ferromagnetism in moiré superlattices. *Nature* **604**, 468-473, doi:10.1038/s41586-022-04472-z (2022).

175 Song, T. *et al.* Giant tunneling magnetoresistance in spin-filter van der Waals heterostructures. *Science* **360**, 1214-1218, doi:doi:10.1126/science.aar4851 (2018).

Appendix A: Power dependence of monolayer WSe_2 excitons in device M2

In another sample (M2) shown in Fig. A.1, its A exciton peak is located around 1.740 eV, possibly due to strains, defects, dielectric environment and temperature fluctuations. Nevertheless, the dark exciton peak is found at 1.699 eV thanks to the high-NA objective lens and the recombination path assisted by phonon and defect scatterings.

Defect peaks are also identified by a saturated peak height at different laser intensities. The spectra of monolayer WSe_2 flakes vary a lot, largely due to the defect states. The monolayer WSe_2 in Fig. A.1 exhibits multiple defect peaks ranging from 1.61 eV to 1.69 eV. Practically, power dependence measurements are used broadly to examine the defect level and the crystal qualities of TMD monolayers from any unknown batches.

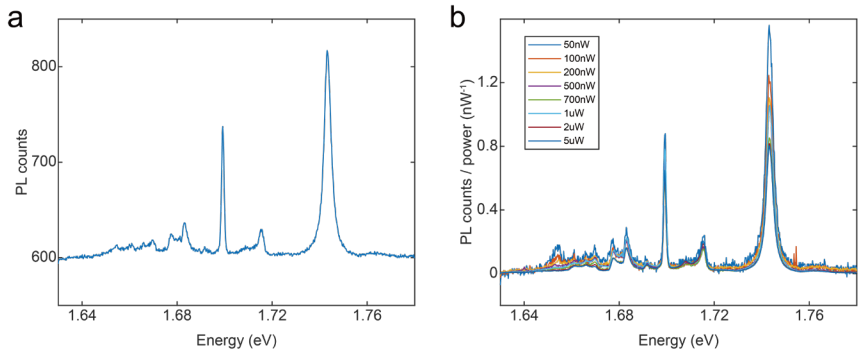

Figure A.1: Power dependence of monolayer WSe_2 excitons in M2. a, PL spectrum of M2 at 1 μW excitation. b, Normalized PL at different excitation powers.

Appendix B: Lattice Reconstructions in Rhombohedral-stacked twisted TMD

Multiple twisted double bilayer WSe_2 devices are fabricated and examined, while the same value is obtained (Fig. B.1 and Fig. B.2). More surprisingly, the same potential difference value is also measured in domains with irregular shapes. After measuring device P2 (Fig. B.1), it's dropped onto the floor and a strong and sudden strain was induced to the sample, causing the domain distribution to reconstruct. Multiple triangular domains are merged and form a huge domain with an irregular shape. When we try to correlate its PFM and KPFM images again, we find the potential difference between two huge domains still equal to 20 mV (Fig. B.2b). The independence of potential difference on domain size (at a small twist angle) further supports our understanding that the stacking order within a triangular is relaxed into either XM or MX configuration, which generates the spontaneous electric polarization. However, in different TMD systems, the potential difference can vary with materials and number of layers.

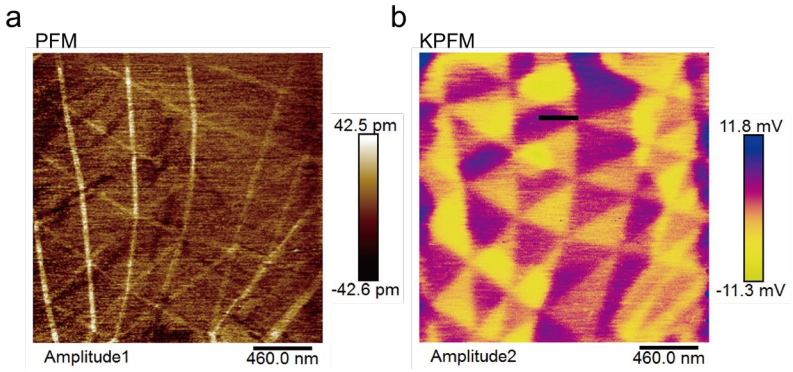

Figure B.1: Visualization of interfacial ferroelectricity in P2 before being strained. a,b, PFM (**a**) and KPFM (**b**) images of the same area on device P2 before being dropped on the floor.

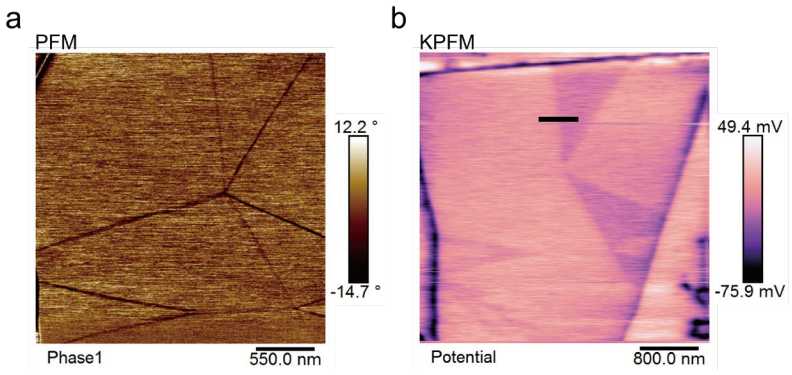

Figure B.2: Visualization of interfacial ferroelectricity in P2 after being strained. a,b, PFM (**a**) and KPFM (**b**) images of the same area on device P2 after being dropped on the floor.

Appendix C: Reconstructing every-other-layer DX

We perform the modeling at different hopping amplitude. At t = 0 meV limit, the every-other-layer DXs do not hybridize with the intralayer species at all (and form direct crossings in Fig. C.1e), with a similar reconstructed spectra as monolayer and bilayer WSe_2 (Fig. C.1a). At t = 20 meV limit, the anti-crossing gaps as well as the second order perturbation gap are becoming larger.

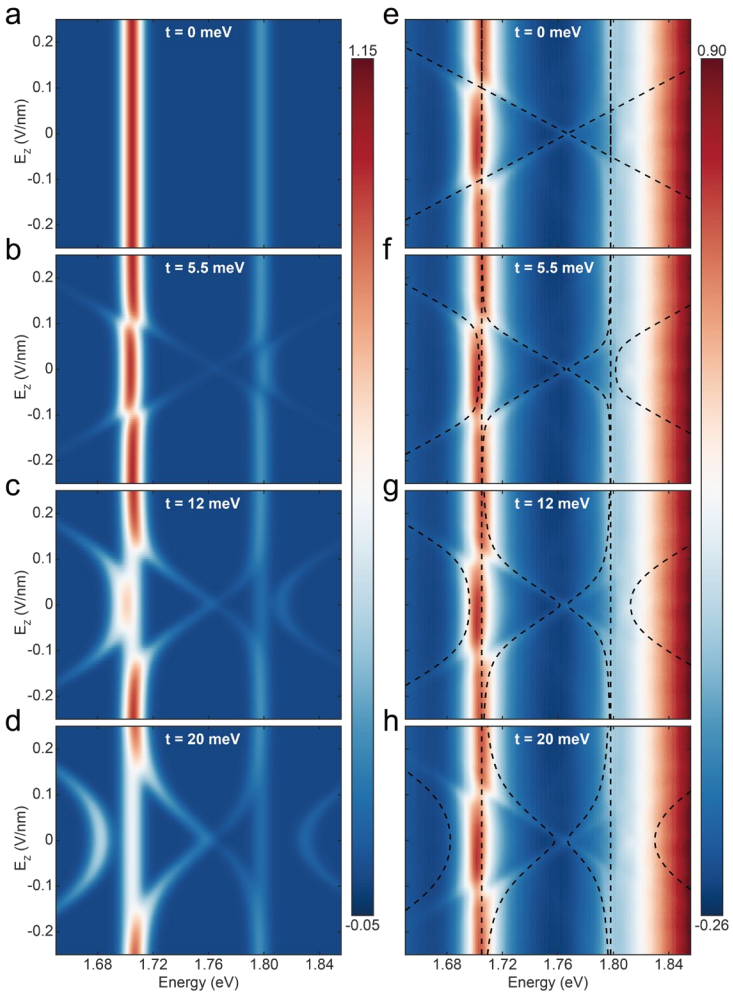

Figure C.1: Every-other-layer DX versus hopping amplitude. a-d, Reconstructed field dependent dR/R spectra at electron/hole hopping amplitudes equal to 0 (**a**), 5.5 meV (**b**), 12 meV (**c**) and 20 meV (**d**). **e-h,** Curve fitting results for electron/hole hopping amplitudes equal to 0 (**e**), 5.5 meV (**f**), 12 meV (**g**) and 20 meV (**h**).

On the other hand, the hopping amplitude of electrons and holes cannot be determined separately from the electric field dependence data due to the energy degeneracy of the intralayer A excitons. The simulations and reconstructions will give similar results if only one carrier (electron or hole) dominates the every-other-layer hopping (Fig. C.2).

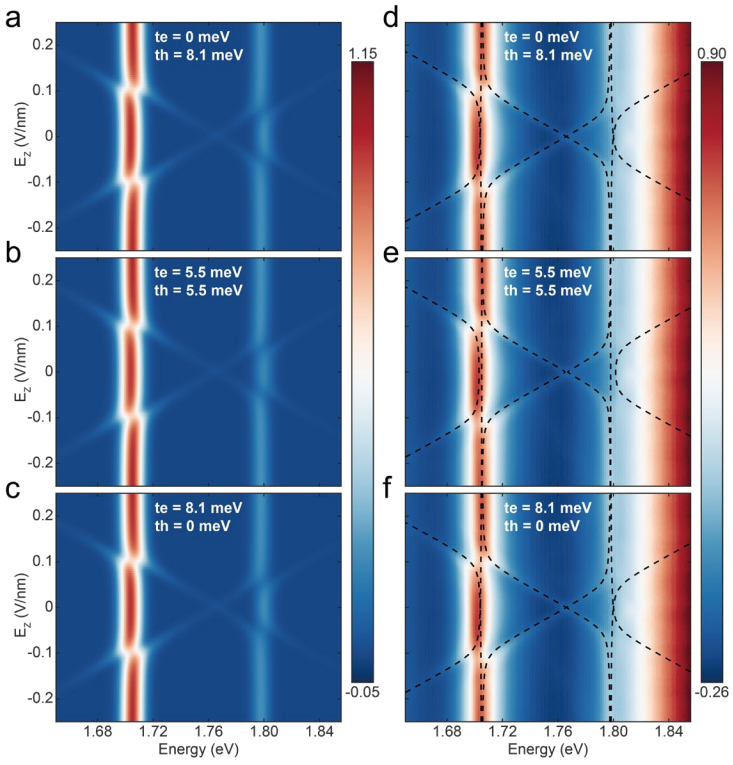

Figure C.2: Every-other-layer DX versus asymmetric hopping amplitude. a-c, Reconstructed field dependent dR/R spectra at hopping amplitudes t_e = 0 meV and t_h = 8.1 meV (**a**), t_e = t_h = 5.5 meV (**b**), t_e = 8.1 meV and t_h = 0 meV (**c**). **e-h,** Curve fitting results for hopping amplitudes t_e = 0 meV and t_h = 8.1 meV (**d**), t_e = t_h = 5.5 meV (**e**), t_e = 8.1 meV and t_h = 0 meV (**f**).

Appendix D: Supplementary data

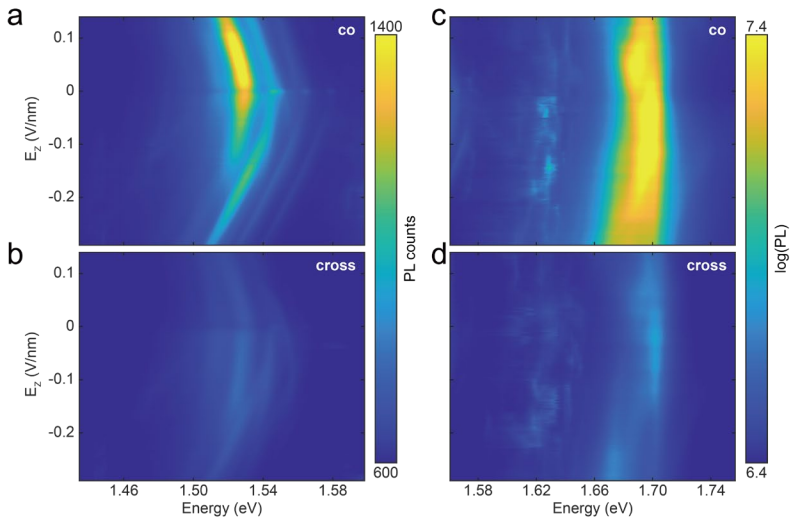

Figure D.1: Electric field dependences of the intravalley and intervalley PL in device W1. a,b, Electric field dependence of the intervalley PL emissions with co-circular (**a**) and cross-circular (**b**) polarizations. **c,d,** Electric field dependence of the intravalley PL emissions with co-circular (**c**) and cross-circular (**d**) polarizations.

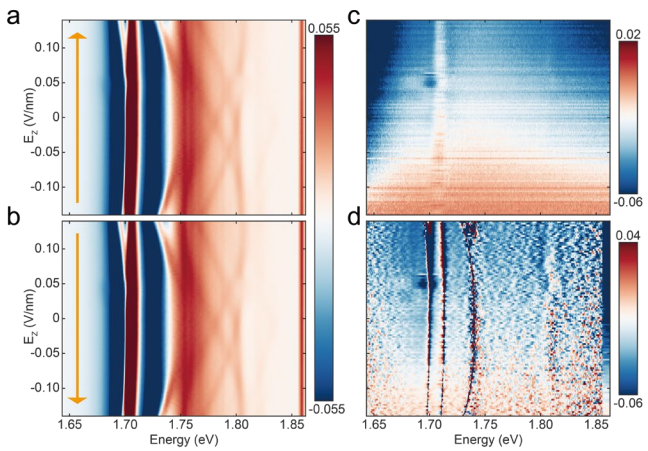

Figure D.2: Hysteresis loop missing from twisted bilayer WSe_2. a,b, Electric field dependence of the differentiated dR/R in twisted bilayer WSe_2 device W1 under an ascending (**a**) and a descending (**b**) external electric field. **c,** Difference between the ascending field dependent dR/R spectra and the descending field dependent dR/R spectra normalized by their average. **d,** Difference between the ascending field dependence of the differentiated PL spectra (**a**) and the descending field dependence of the differentiated PL spectra (**b**) normalized by their average.

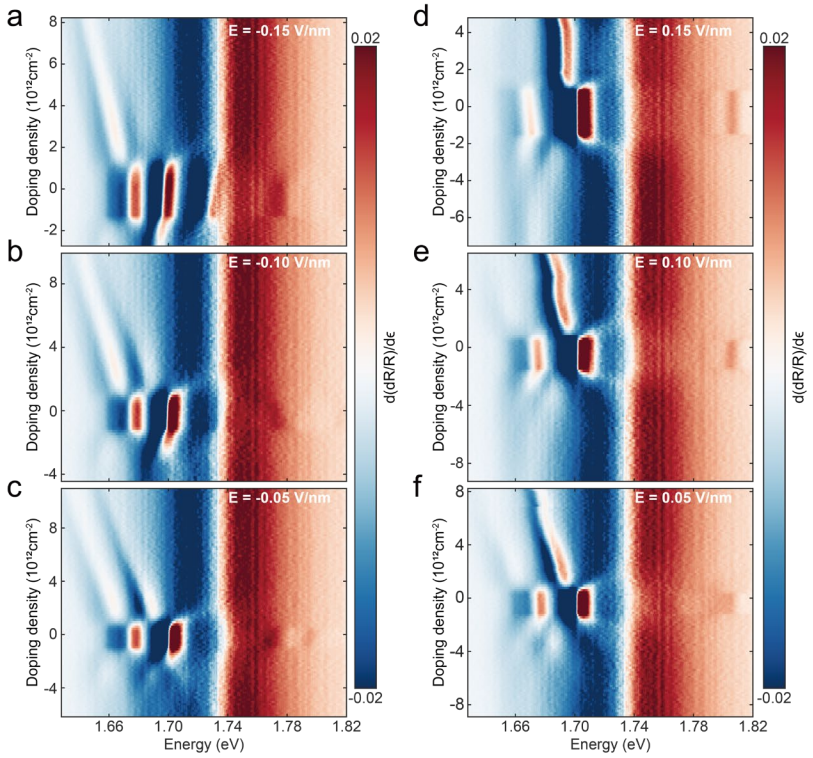

Figure D.3: Layer polarization analysis. a-f, Doping density dependence of the differentiated dR/R resonances at fixed out-of-plane electric fields equal to -0.15V/nm (a), -0.10 V/nm (b), -0.05 V/nm (c), 0.15 (**d**), 0.10 V/nm (**e**) and 0.05 V/nm (**f**).